ANALYSIS AND DESIGN OF

VIA LOADED MICROSTRIP ANTENNAS

A Dissertation

Presented to

the Faculty of the Department of Electrical and Computer Engineering

University of Houston

In Partial Fulfillment

of the Requirements for the Degree

Doctor of Philosophy

in Electrical Engineering

by

Osman Kanlioglu

August 2007

ANALYSIS AND DESIGN OF

VIA LOADED MICROSTRIP ANTENNAS

Osman Kanlioglu

Approved:

Chairman of the Committee
David R. Jackson, Professor,
Electrical and Computer Engineering

Committee Members:

Jeffery T. Williams, Professor,
Electrical and Computer Engineering

Donald R. Wilton, Professor,
Electrical and Computer Engineering

Edgar A. Bering, Professor,
Physics

Xiaojing Jane Yuan, Professor,
Engineering Technology

L. C. Witte, Associate Dean,
Cullen College of Engineering

H. Ogmen, Professor and Chairman,
Electrical and Computer Engineering

Acknowledgements

I would like to express my most sincere thanks and gratitude to my dissertation advisors, Dr. David R. Jackson and Dr. Jeffery T. Williams for their guidance and encouragement. I deeply appreciate their endless patience and wisdom. I learned innumerable lessons from you, concerning my research topic and electromagnetics and antennas in general. I would also like to thank Dr. Donald R. Wilton and Dr. Stuart A. Long for their valuable support and guidance.

My sincere gratefulness is extended to all the members of the Electromagnetics Group, who have become not only my colleagues but also close friends: Hao Xu, Chatrpol Lertsirimit, Tianxia Zhao, Richard Chen, Timothy F. Kennedy, William L. Langston, Michael A. Khayat, Christopher De Young, Akbar Ng, Ying Hu, Siddhart Oroskar, Turker Celepcikay, Varadarajan Komanduri, Anthony Lau, Weixin Dong and Vikram Shete. I will miss you all.

Lastly, I would like to express my foremost gratitude to my family. My parents and dear brother always supported me with their love and encouragement. I would like to dedicate my dissertation to my dear wife who never left me alone in this challenging journey and made priceless sacrifices.

ANALYSIS AND DESIGN OF

VIA LOADED MICROSTRIP ANTENNAS

An Abstract

of a Dissertation

Presented to

the Faculty of the Department of Electrical and Computer Engineering

University of Houston

In Partial Fulfillment

of the Requirements for the Degree

Doctor of Philosophy

in Electrical Engineering

by

Osman Kanlioglu

August 2007

Abstract

Various planar antenna geometries are encountered that include a circular array of conducting vias (metallic posts). Examples include shorted-annular-ring reduced-surface-wave (SAR-RSW) microstrip antennas, dual-band UHF antennas, and miniaturized microstrip antennas. An accurate analysis of such geometries is thus important. This dissertation presents an electromagnetic investigation of a circular array of vias. The reflection coefficient of a cylindrical wave impinging on a circular array of vias is found analytically. For validation, an equivalent strip model is introduced as a second method to calculate the reflection coefficient of the via array. Equivalent sheet and surface impedance models of the via array are found in terms of the reflection coefficient. A loss calculation for a via array is also introduced and an equivalent sheet resistance of the via array is found.

Numerical calculations are presented for the reflection coefficients, as well as the sheet and surface impedances, for several via arrays with different geometries. The change in these quantities is observed by varying the number of vias, the radius of the vias, the radius of the via array, and the dielectric of the medium. These calculations are repeated for the strip model and very good agreement is obtained between the two models, demonstrating the validity and accuracy of the via array analysis. To further validate the via analysis, cavities are created that contain an array of vias. These cavities are simulated with the full-wave electromagnetic simulation software Ansoft HFSS in order to obtain numerically exact values for the resonance frequency and the surface impedance

of the via array. These quantities are compared with the corresponding analytical values based on the via array analysis, and very good agreement is obtained.

Finally, the utilization of via arrays in practical antenna design is demonstrated. An SAR-RSW antenna for GPS is designed using a surface impedance wall realized by a circular array of vias. A UHF dual-band microstrip antenna design is also presented that uses a circular via array to realize dual-band performance. A miniaturized circular microstrip antenna with a monopole-like pattern is also designed using a circular array of vias.

Table of Contents

List of Figures

List of Tables

Chapter 1
Introduction

This dissertation addresses the analysis of a circular array of vias (metallic posts) that is sandwiched between two infinite metallic planes. The circular array of vias arises in various antenna applications, and these are discussed below in order to provide motivation and background for this subject.

1.1 Microstrip Antennas

Low-profile antennas are required in aircraft, spacecraft, satellite and missile applications, where size, weight, cost, performance, ease of installation, and aerodynamic profile are constraints. Microstrip antennas, which are often described as one of the most useful developments in antenna history, can be used to meet these requirements. Microstrip patch antennas belong to a class of printed antennas that includes dipoles, slots and tapered slots, and are the most popular and adaptable. Microstrip antennas are low profile, conformable to planar and nonplanar surfaces, simple and inexpensive to manufacture using modern printed-circuit technology, compatible with monolithic microwave integrated circuit (MMIC) designs, and mechanically robust. They are versatile in terms of resonance frequency, impedance, polarization, and radiation pattern. Also, adaptive antennas with a variable resonance frequency, impedance, polarization, and pattern can be designed by adding elements to the patch, such as vias and varactor diodes [1], [2], [3].

The disadvantages of microstrip antennas are their narrow bandwidth, low efficiency, low power-handling capability, and spurious feed radiation. The height of the substrate can be increased to improve the bandwidth. However, as the height increases, the dominant TM_0 surface wave is more strongly excited (unless an air substrate is used), which is not desirable since this decreases the radiation efficiency and degrades the antenna pattern and polarization characteristics due to scattering from the edges of the substrate and ground plane and feed radiation [1].

1.2 Reduced Surface Wave (RSW) Microstrip Antennas

In 1993, new types of microstrip antennas were investigated that had reduced surface wave excitation. These microstrip antennas are based on the principle that a ring of magnetic current in a substrate, which models a circular microstrip patch, will not excite the dominant TM_0 surface wave if the radius of the ring is a particular critical value. These patch designs result in very little surface-wave excitation as well as greatly reduced lateral radiation (radiation along the horizon) and thus have smoother radiation patterns when mounted on finite-size ground planes, due to reduced diffraction. These new antenna designs also have reduced mutual coupling to adjacent structures, due to the reduced surface-wave excitation and lateral radiation [4].

One of the RSW designs that has been investigated is the shorted-annular-ring reduced-surface-wave (SAR-RSW) antenna shown in Figure 1.1. This antenna consists of an annular ring microstrip antenna with a short-circuit inner boundary introduced by a circular array of vias at radius R_0. When operating in the TM_{011} mode, the antenna will excite the dominant TM_0 surface wave of the grounded substrate having a field at the ground plane that varies as [4]

$$E_z^{SW} = A(z) H_1^{(2)}\left(k_{TM_0}\rho\right)(\cos\phi) J_1'\left(k_{TM_0}R_1\right), \tag{1.1}$$

where $A(z)$ is the variation along the vertical z direction, k_{TM_0} is the propagation wavenumber for the TM_0 surface wave, and R_1 is the outer radius of the patch.

The amplitude of the TM_0 surface wave is controlled by the $J_1'\left(k_{TM_0}R_1\right)$ Bessel function. This term is dependent only on the substrate and the geometry and the amplitude of this surface wave mode can be set to zero by choosing the antenna radius R_1 such that

$$R_1 = \frac{x_{1n}'}{k_{TM_0}}, \tag{1.2}$$

where x_{1n}' is the n^{th} zero of the derivative of the J_1 Bessel function. Because of the oscillatory nature of the Bessel function, there are an infinite number solutions to (1.2). The smallest value of R_1 corresponding to x_{11}' is chosen to keep the antenna size as small as possible. For thin substrates, where $k_{TM_0} \approx k_0$, the R_1 value from (1.2) will not only make the surface wave excitation of TM_0 mode zero, but will also greatly reduce the lateral radiation (the space wave that propagates along the air-dielectric boundary of the microstrip antenna).

In order to make the TM_{011} mode of the antenna resonant at the desired operating frequency (the frequency for which the antenna has RSW performance), the inner boundary at radius R_0 is short circuited to the ground plane using a circular array of vias. The radius of the circular via array R_0 is selected to make the antenna resonant at the operating frequency. After obtaining the outer radius from (1.2) at the desired operating frequency, the inner radius R_0 can be found using the following transcendental equation

$$\frac{J_1(k_1R_0)}{Y_1(k_1R_0)} = \frac{J_1'(k_1R_1)}{Y_1'(k_1R_1)}, \tag{1.3}$$

where k_1 is the wavenumber in the dielectric substrate, R_1 is the outer radius of the patch, and R_0 is the radius of the circular via array which is modeled as a short-circuit wall.

The SAR-RSW antennas produce only a small amount of surface-wave excitation, due to the higher-order patch modes, so there is very little edge diffraction from the edges of the substrate and ground plane, and hence very little interference with the forward radiation pattern and significantly reduced back-scattered radiation compared to a conventional microstrip patch antenna. This is demonstrated in Figure 1.2 [5]. These characteristics make the RSW antenna ideal for applications when the supporting ground plane of the

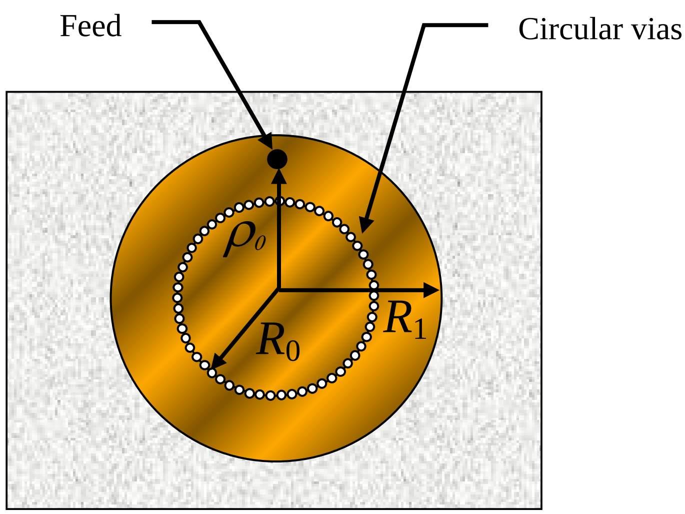

(a)

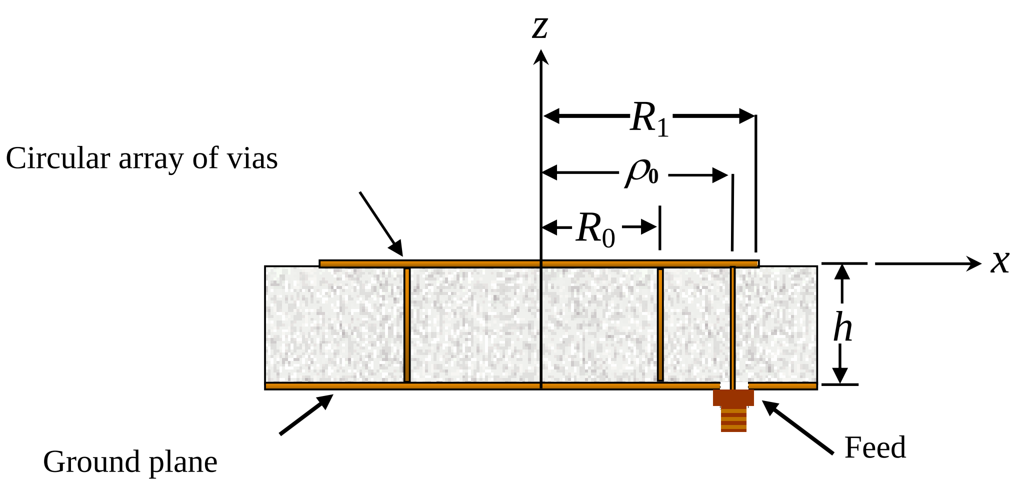

(b)

Figure 1.1. Shorted-annular-ring reduced-surface-wave (SAR-RSW) antenna. (a) Top view. (b) Side view.

antenna is small. The RSW antenna has potential benefits for global position system (GPS) applications, since it significantly reduces the deleterious effects of low-angle and ground-bounce multipath signals, which are problematic signals that impinge on the antenna at low elevation angles as a result of ground reflections or scattering from the supporting structure of the antenna [6]. Therefore, SAR-RSW antennas are good candidates for high-precision GPS systems. Extending the concept, dual-band RSW antennas have been designed to receive GPS signals in both the L1 (1.575 GHz) and L2 (1.227 GHz) frequency bands [7].

Mutual coupling between two SAR-RSW antennas has also been studied in past work. It was shown that this coupling was significantly lower and dropped off faster with separation distance compared to conventional microstrip antennas [8].

One consequence of using a thin substrate for the RSW antenna is its narrow bandwidth. Two RSW designs have been introduced to increase the impedance bandwidth without sacrificing the RSW performance. One is the “fence” design where the RSW antenna is surrounded by a vertical conducting fence. The other design is a recessed cavity-backed annular slot design [9].

1.3 Center-Fed Microstrip Antennas with Vias

Some antenna applications require a monopole-like radiation pattern (conical shape), having maximum radiation at the horizon with a null at broadside, as shown in Figure

1.3. A circular array of vias may be used to create an antenna with a monopole-like pattern that is broadband, or is dual-band. An example of a dual-band UHF antenna designed using a circular array of vias is presented in Chapter 5.

A circular microstrip antenna fed at its center produces a conical pattern that is azimuthally symmetric. However, the size of this type of antenna operating at resonance is large in terms of a wavelength. The appropriate use of shorting vias in microstrip antennas can permit size reduction [9], [10], [11], [12]. This is also explored here in Chapter 5 to arrive at the design of a miniaturized center-fed circular microstrip antenna that incorporates a circular array of vias.

1.4 Electromagnetic Analysis of a Circular Via Array

As explained above up to this point, shorting vias have an important role in many types of microstrip antennas. Circular arrays of vias are used in RSW antennas to obtain a short circuit wall to achieve a resonant antenna that doesn't excite surface waves. Similar via arrays can be used to improve impedance bandwidth, obtain dual-band behavior, or to miniaturize the antenna. Therefore, an accurate analysis of these via arrays is important to understand and design the various antennas that incorporate these structures. In this dissertation a full-wave electromagnetic analysis of a circular via array will be developed that will then be applied to three different antennas: a SAR-RSW antenna for GPS applications, a dual-band UHF antenna, and a center fed microstrip UHF antenna.

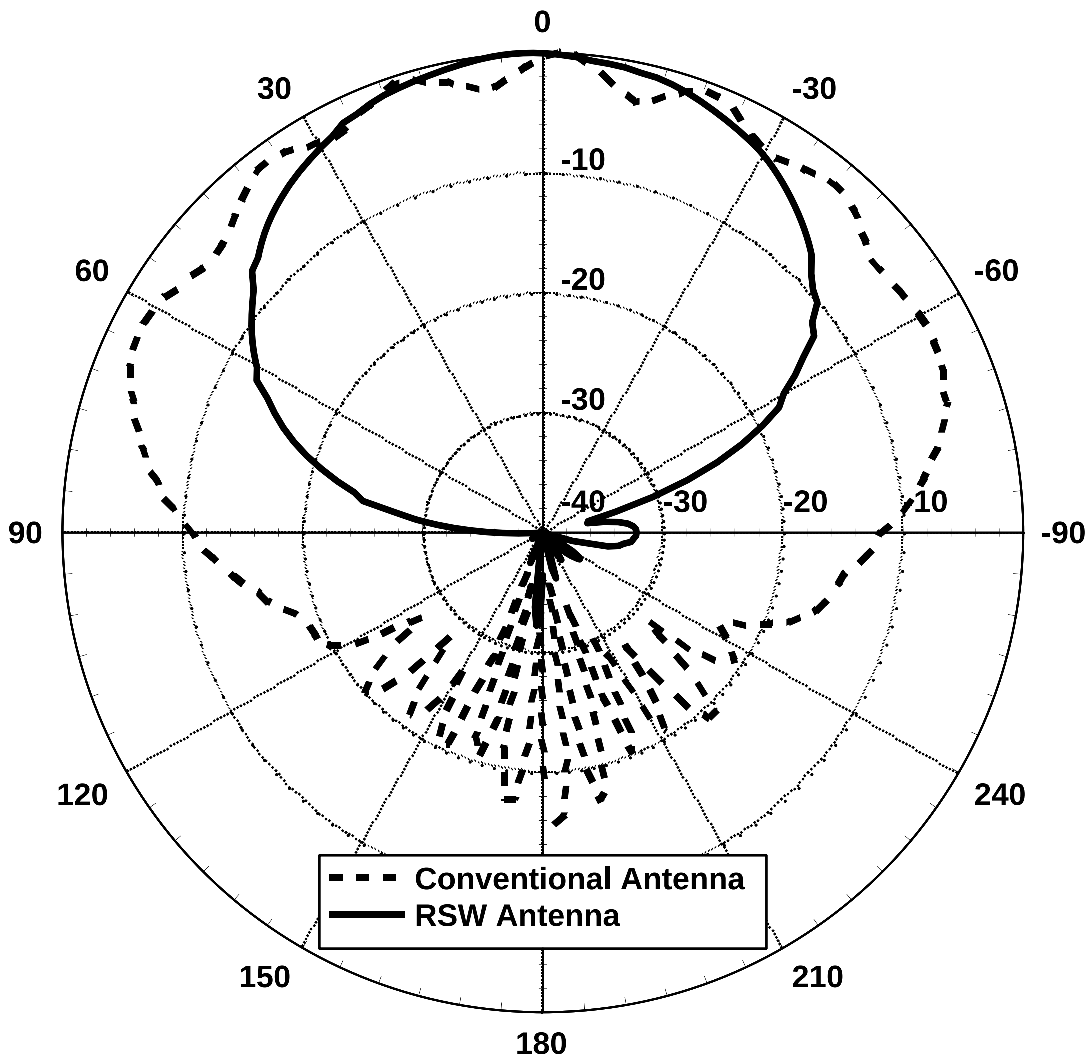

Figure 1.2. A comparison between the E-plane radiation patterns of a conventional patch antenna and an RSW patch antenna at 2.0 GHz on a 1 meter diameter circular ground plane [5].

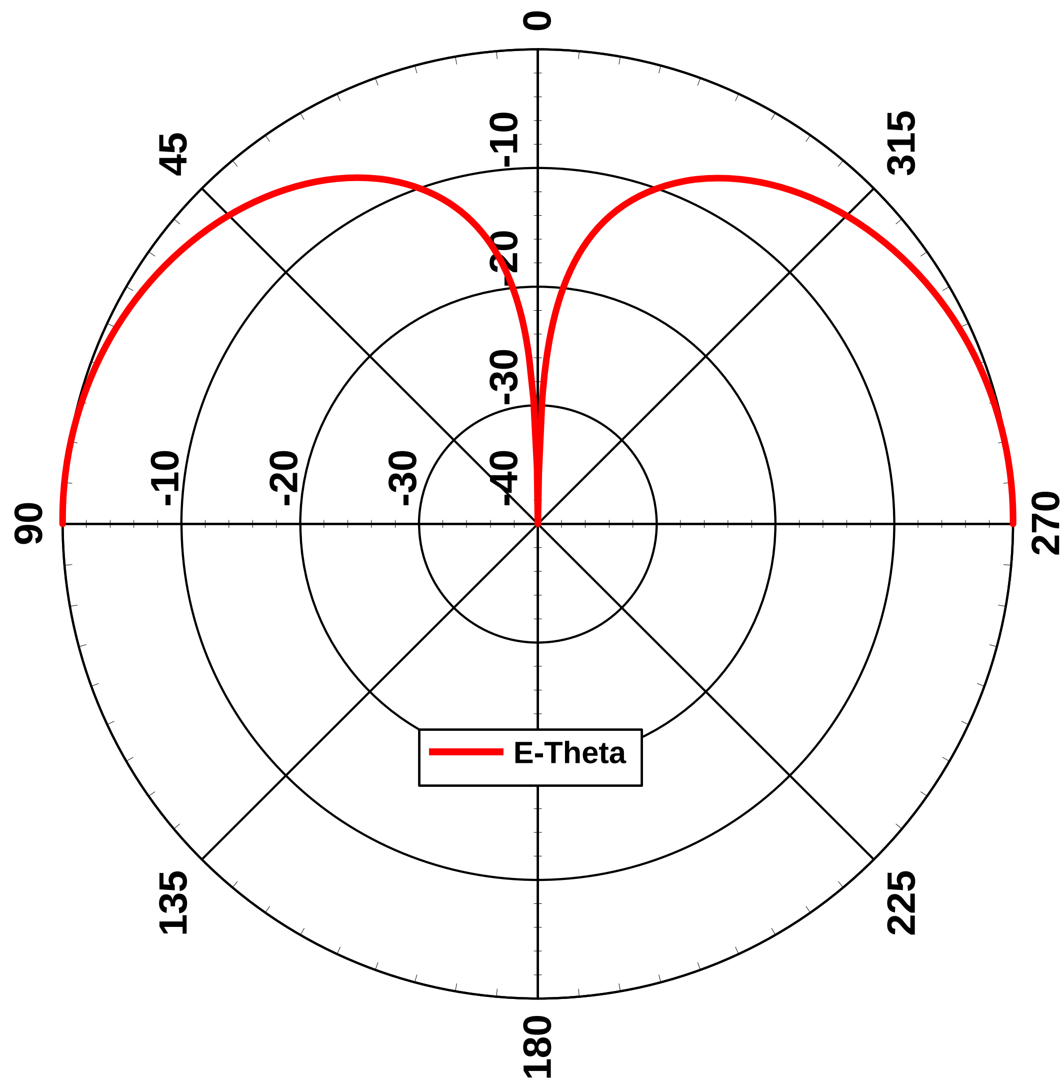

Figure 1.3. The far-field component E_θ for a quarter-wavelength monopole on an infinite ground plane at $f = 2\ \text{GHz}$.

1.5 Organization of the Dissertation

In Chapter 2, the full-wave electromagnetic analysis of a circular via array sandwiched between two infinite perfectly conducting planes is presented using two methods. First, the vias are modeled with infinitely long cylinders (which accurately describes the actual cross-sectional shape of the vias). The array is analyzed to find the induced currents on the vias when the array is excited by an impinging cylindrical wave having an azimuth variation described by $\exp(-jn_i\phi)$. The method of moments (MoM) together with the electric field integral equation (EFIE) is used to solve for the unknown currents. The addition theorem is used in this method to relate fields in different coordinate systems so that a closed-form evaluation of the necessary reaction integrals may be obtained. Exterior and interior reflection coefficients are obtained, for an incident cylindrical wave that impinges on the circular via array from either the exterior or the interior region, respectively.

In order to provide validation, a second model of the circular array of vias is introduced using a strip model that uses flat strips with an appropriate effective width in order to model the circular vias. A cylindrical wave analysis of the circular array of flat strips is used to solve for the currents on the strips and the reflection coefficient.

After the reflection coefficients are obtained, these values are converted to sheet and surface impedance values. These values are particularly useful for analyzing and designing antenna that incorporate circular via arrays.

Chapter 3 presents loss calculations assuming that the vias are not perfectly conducting, but are composed of a normally conducting metal that is represented by a surface resistance. The power dissipated in the via array is found by summing all the (identical) powers dissipated on each via. This is equated to the power dissipated in an equivalent sheet impedance model of the circular via array. Equating these two powers, the equivalent sheet resistance of the via array is then calculated.

Chapter 4 of the dissertation is mainly devoted to presenting results from the analytical models discussed in Chapter 2, and their comparison with the full-wave electromagnetic software simulation tool Ansoft HFSS. The reflection coefficient resulting from two different methods, the via model and the equivalent strip model, are compared in order to validate the via analysis results. This comparison is done by changing different parameters of the circular via array such as the number of vias, the via radius, the radius of the array, the number of basis functions, the operating frequency, and the dielectric medium.

Sheet and surface impedances are also calculated from the reflection coefficient results. In the later part of this chapter, several different cylindrical cavities with perfect electric conductor (PEC) and perfect magnetic conductor (PMC) outer walls that have a circular array of vias inside are used to provide validation. The resonance frequencies of these cavities are calculated using HFSS and the via analysis (along with a simple analytical cavity model). The validity and accuracy of the via array analysis is assessed by comparing the resonance frequencies.

In Chapter 5, three examples of antennas designed using the via-array analysis are presented. First, a new method for designing SAR-RSW antennas using a circular array of vias is presented. The classical method of designing SAR-RSW antennas has been changed to use a reactive wall that is realized by using an array of vias instead of a short-circuit wall. A location is chosen for the impedance wall and then the required value of sheet reactance is found using a cavity analysis. Once sheet reactance value is determined, the number of vias and their radii are determined by using the via analysis. Radiation patterns are obtained using HFSS for these types of RSW antennas.

Another type of antenna, a dual-band UHF antenna that uses a circular via array, is also presented in Chapter 5. The circular via array is used for obtaining dual resonances in this particular antenna. The original design procedure used previously for this antenna, which uses an iterative process for determining the number of vias and the radius of the via array, is improved using the new via-array analysis. The agreement of the results from the new approach and the previous design procedure proves validation of the via analysis and demonstrates its usefulness.

The last practical example presented in Chapter 5 is an implementation of a circular via array to realize a miniaturized circular microstrip antenna that has a monopole-like radiation pattern. This antenna uses the array of vias for reducing the size of the antenna. The required sheet impedance value is found using a radial transmission line model, and the via geometry is then realized by using the via analysis presented here. This example serves as further validation of the via-array analysis, and also demonstrates another practical use of the circular via array.

Chapter 2
Electromagnetic Analysis of a Circular Array of Vias

2.1 Introduction

There are many applications for a circular array of vias in microstrip antenna designs, such as creating a short circuit wall in a RSW microstrip antenna to create an antenna that reduces unwanted surface-wave effects; and loading a microstrip antenna to change the input impedance in order to reduce overall antenna size.

The accurate analysis of a circular array of vias is very important in order to understand and make use of this structure. In this chapter, the circular array of vias is modeled as an array of infinitely long conducting cylinders that models the actual (vertically independent) microstrip antenna field. Then, assuming an incident cylindrical field impinging onto the vias, the reflected field is found by taking all field interactions into account.

The incident and scattered field expressions determine the reflection coefficient from the circular array of vias. Analytical expression for these fields are used to calculate reflection coefficient values for several arrays with different physical dimensions.

Two different methods are used to find the scattered field of the via array. One is a classical electromagnetic analysis of the array using infinite cylinders to model the vias. The other one uses flat current strips to approximate the vias. In each case, an Electric Field Integral Equation (EFIE) is derived and then solved to obtain the unknown current coefficients.

2.2 Infinite Cylinder Model Analysis

The circular array of vias between two ground planes can be analyzed by modeling them as infinitely long cylinders in a homogenous space. The field expressions will be given and interactions will be found by using the EFIE.

2.2.1 Modeling of the Circular Array of Vias

A circular array of vias is shown inside of a microstrip antenna in Figure 2.1(a). In this figure the vias are simply conducting cylinders connecting an upper conductor (usually the microstrip patch) to the ground plane. Assuming that the vias are well within the patch (not near the edges) and the separation between the conductors is electrically small (no variations along the axis of the vias), the circular array of vias can be modeled with infinitely long cylinders using image theory as shown in Figure 2.1(b) [13]. The homogenous medium in which the infinitely long cylinders reside is the same as the dielectric of the microstrip antenna.

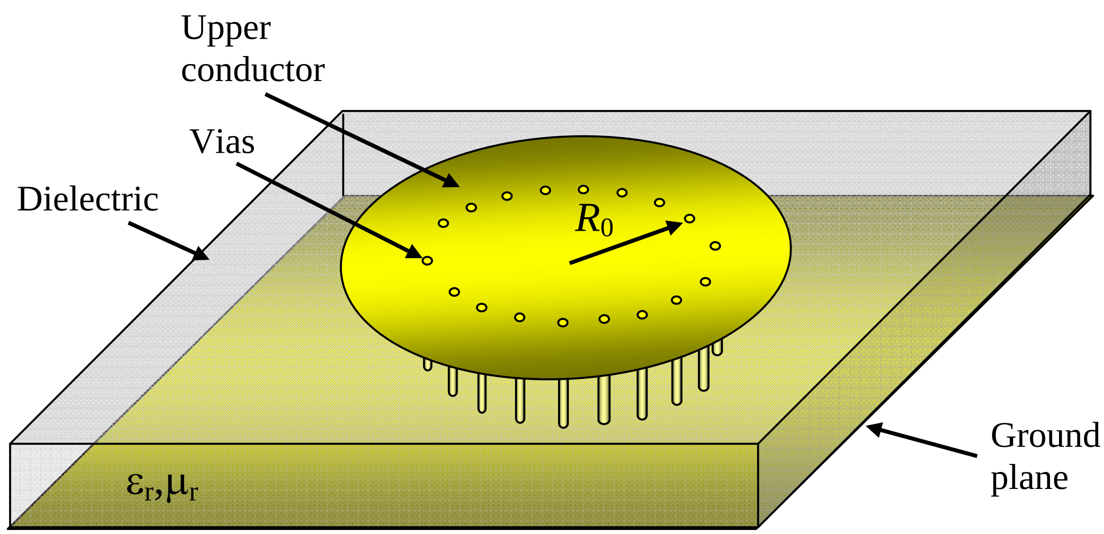

(a)

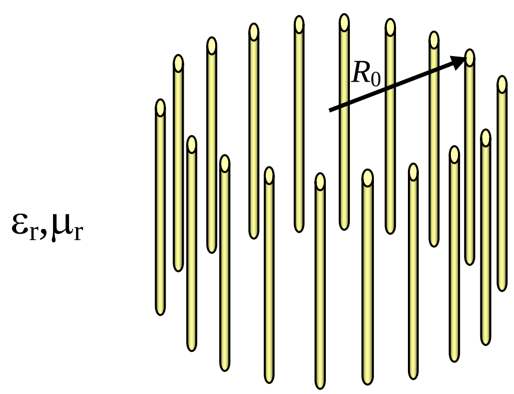

(b)

Figure 2.1. (a) A microstrip antenna that contains a circular array of vias, (b) An equivalent model of the circular array of vias.

2.2.2 Modeling of a Single Via

It is necessary to know the exact distribution of the current on each via, or on the equivalent infinitely long perfect electric conductor (PEC) cylinder, in order to find the total scattered field. It is known that the electric field radiated from a cylinder with the radius *a*, at the origin, with constant unit amplitude current and phase distribution, $J_{szn}\ (\phi, z) = e^{jn\phi}$ is [13]

$$E_z(\rho,\phi) = H_n^{(2)}\left(k\rho\right)\left[-\pi\eta\left(\frac{ka}{2}\right)J_n\left(ka\right)\right]e^{jn\phi} \qquad \left(\rho > a\right), \tag{2.1}$$

where k is the wavenumber and η is the wave impedance of the medium. Locating the center of the array at the center at the cylindrical coordinate system as shown in Figure 2.2, the more general scattered electric field radiated from the l^{th} via in the array with unity current density can be written as

$$E_z^{s,(l)}(\rho,\phi) = H_n^{(2)}\left(k\rho_l'\right)\left[-\pi\eta\left(\frac{ka}{2}\right)J_n\left(ka\right)\right]e^{jn\phi_l'} \qquad \left(\rho > a\right), \tag{2.2}$$

where ρ_l' is the distance between the l_{th} via center and the observation point.

The unknown current distribution on the reference via (the via on the positive *x*-axis that is labeled as $l = 0$) can be written as a Fourier series in terms of $e^{jn\phi_0'}$ current bases as

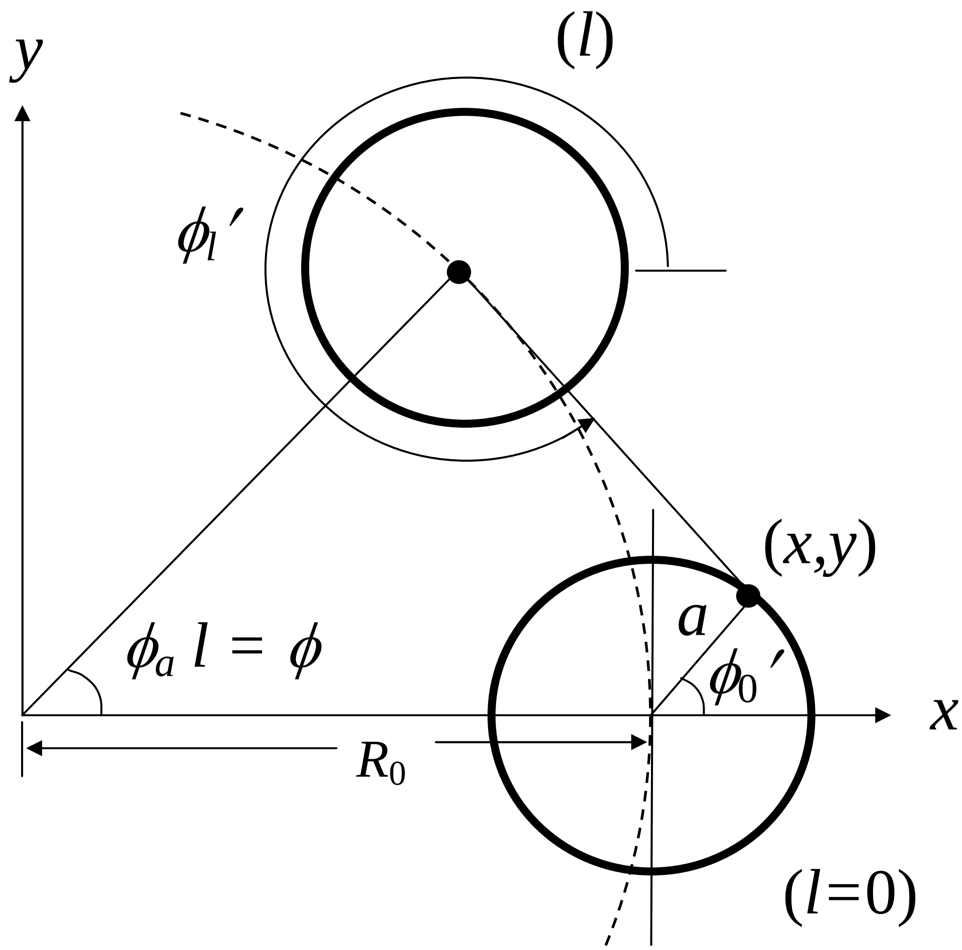

Figure 2.2. The rectangular coordinate system and the defined parameters for the via-array analysis.

$$J_{sz}^{(0)}(\rho,\phi) = \sum_{n=-N}^{n=N} a_n e^{jn\phi_0{}'} , \qquad (2.3)$$

where a_n is amplitude of the unknown current basis function, n is the order of the current basis function, $2N+1$ is the total number of current basis functions, and $\phi_0{}'$ is the local reference coordinate system angle.

The current induced on l^{th} via, due to an incoming field of the form $E_z^i = H_{n_i}^{(1)}(k\rho)e^{jn_i\phi}$, will be the same as that of the reference via except for the coordinate shift by $l\phi_a$ and a phase difference by $e^{jn_i l\phi_a}$, so that

$$J_{sz}^{(l)}(\rho,\phi) = e^{jn_i l\phi_a} \sum_{n=-N}^{n=N} a_n e^{jn(\phi_l{}' - l\phi_a)} , \qquad (2.4)$$

where $\phi_l{}'$ is the angle between the x-axis and the line connecting the center of the l^{th} via and the observation point, and ϕ_a is the discrete angle between the vias. Since the electric field is proportional to the current density, the fields radiated from each via defined using (2.2) and (2.4) are summed to find the total electric field re-radiated from the array due to the incoming field of $E_z^i = H_{n_i}^{(1)}(k\rho)e^{jn_i\phi}$ as

$$E_z^s(\rho,\phi) = \sum_{n=-N}^{n=N} a_n \sum_{l=0}^{L-1} e^{jn_i l\phi_a} e^{jn(\phi_l{}' - l\phi_a)} H_n^{(2)}\left(k\rho_l'\right)\left[-\pi\eta\left(\frac{ka}{2}\right)J_n\left(ka\right)\right]. \qquad (2.5)$$

The scattered electric field from the l^{th} via with unit amplitude current density and with the phase variation of the nth basis function, is written as

$$E_z^{s,(l)}(\rho,\phi) = e^{jn_l l\phi_a} e^{jn(\phi_l' - l\phi_a)} H_n^{(2)}\left(k\rho_l'\right)\left[-\pi\eta\left(\frac{ka}{2}\right) J_n\left(ka\right)\right]. \qquad (2.6)$$

The total scattered electric field can then be written in the form

$$E_z^s(\rho,\phi) = \sum_{n=-N}^{n=N} a_n \sum_{l=0}^{L-1} E_z^{s,(l)}(\rho,\phi) \,. \qquad (2.7)$$

2.2.3 Electric Field Integral Equation (EFIE)

The key to the solution of any scattering problem is knowledge of the current density distributions on the surface of the scatterer. Once these are known then the scattered fields can be found using standard radiation integrals. This can be accomplished by the Electric Field Integral Equation method.

The electric field integral equation enforces the boundary condition that the total electric tangential electric field on the perfectly conducting (PEC) surface of a scatterer is zero [13]. In the via-array problem, the EFIE enforces the vanishing of the tangential electric field on the surface of every via. Because of the rotational symmetry of the structure, all the unknown currents can be found by solving the currents on one via only. The reference via (via along the positive *x* axis) will be chosen to implement the EFIE for simplicity.

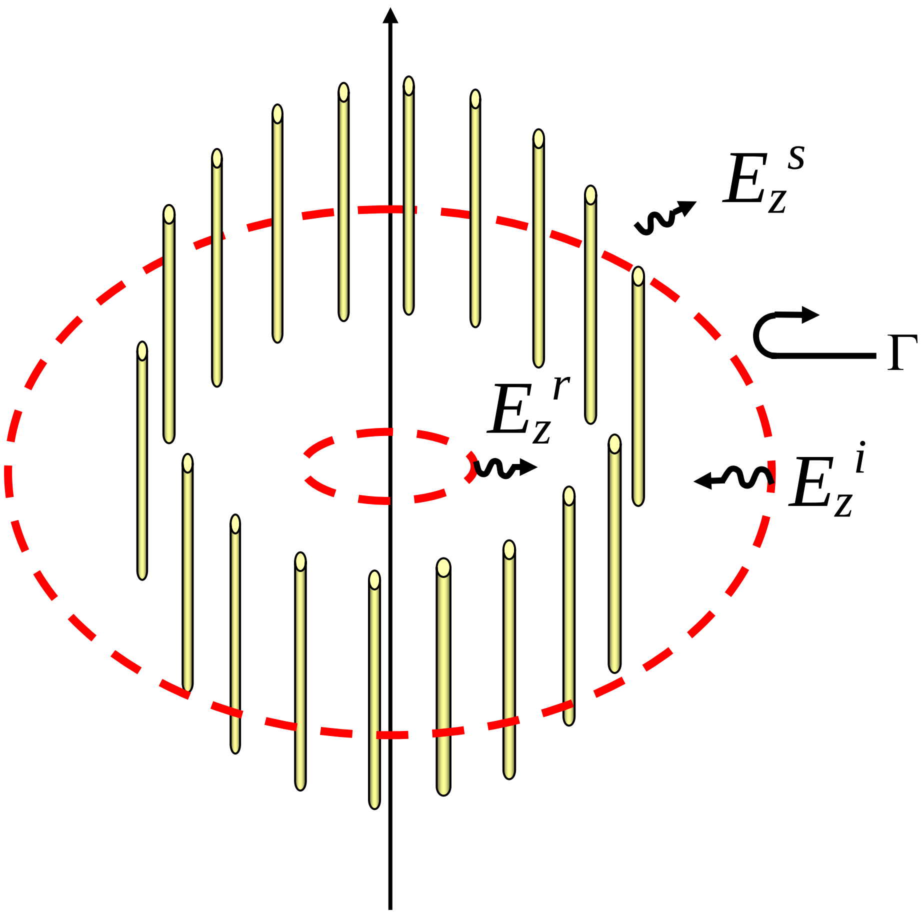

Figure 2.3. The incoming, reflected and the scattered cylindrical fields for the via array.

For this problem, an incoming cylindrical wave is expressed using a Hankel function of the first kind as

$$E_z^i\left(\rho,\phi\right) = e^{jn_i\phi} H_{n_i}^{(1)}\left(k\rho\right). \tag{2.8}$$

The amplitude of the incoming wave is normalized to unity and the other fields are found accordingly. In the absence of scatterers an outgoing wave is also present. This outgoing or *reflected wave* results from the incoming cylindrical wave being "reflected" by, the *z*-axis. This reflected wave is similar to (2.8) with an outgoing Hankel function of the second kind and a unit magnitude since the medium is lossless. The reflected field is written as

$$E_z^r\left(\rho,\phi\right) = e^{jn_i\phi} H_{n_i}^{(2)}\left(k\rho\right). \tag{2.9}$$

The EFIE is obtained by summing all of the E_z fields on the reference via surface ($\rho_0' = a$) and setting the sum to zero,

$$E_z^i(\rho,\phi) + E_z^r(\rho,\phi) + E_z^s(\rho,\phi) = 0 \qquad (\rho_0' = a). \tag{2.10}$$

The sum of the incoming and reflected fields will be referred to as the "impressed field" and it is equal to

$$E_z^{imp}(\rho,\phi) = E_z^i(\rho,\phi) + E_z^r(\rho,\phi) = 2e^{jn_i\phi} J_{n_i}\left(k\rho\right) \qquad (\rho = a). \tag{2.11}$$

Then the EFIE equation becomes

$$\sum_{n=-N}^{n=N} a_n \sum_{l=0}^{L-1} E_z^{s,(l)}(\rho,\phi) = -2e^{jn_i\phi} J_{n_i}\left(k\rho\right) \qquad (\rho_0' = a). \tag{2.12}$$

Galerkin's method is used to solve this equation. Multiplying both sides of (2.12) by a $e^{-jm\phi_0'}$ testing function and integrating both sides of (2.12) on the reference via from 0 to 2π results in

$$\int_0^{2\pi} e^{-jm\phi_0'} \sum_{n=-N}^{n=N} a_n \sum_{l=0}^{L-1} E_z^{s,(l)}(\rho,\phi) a d\phi_0' = -2\int_0^{2\pi} e^{-jm\phi_0'} e^{jn_i\phi} J_{n_i}\left(k\rho\right) a d\phi_0' \qquad (\rho_0' = a) . \tag{2.13}$$

The left hand side (LHS) and the right hand side (RHS or b_m terms) of (2.13) are treated separately. The left hand side is written as

$$LHS = \int_0^{2\pi} e^{-jm\phi_0'} \sum_{n=-N}^{N} a_n \sum_{l=0}^{L-1} e^{jn_i\phi_a l} e^{jn(\phi_l' - l\phi_a)} H_n^{(2)}\left(k\rho_l'\right)\left[-\pi\eta\left(\frac{ka}{2}\right) J_n\left(ka\right)\right] a\, d\phi_0' . \tag{2.14}$$

Interchanging the order of the integral and the summation over *n* result in

$$LHS = \sum_{n=-N}^{N} a_n \underbrace{\int_0^{2\pi} e^{-jm\phi_0'} \sum_{l=0}^{L-1} \underbrace{e^{jn_i\phi_a l} e^{jn(\phi_l' - l\phi_a)} H_n^{(2)}\left(k\rho_l'\right)\left[-\pi\eta\left(\frac{ka}{2}\right) J_n\left(ka\right)\right]}_{E_z^{(l)}(\rho,\phi)} a\, d\phi_0'}_{Z_{mn}} \tag{2.15}$$

Since the integrand in (2.15) gives the interaction between the testing current and the electric field from all the vias, it is called the impedance element Z_{mn}, as denoted in (2.15).

The LHS of the EFIE equation then becomes

$$LHS = \sum_{n=-N}^{N} a_n Z_{mn} . \tag{2.16}$$

Reorganizing the Z_{mn} term

$$Z_{mn} = \sum_{l=0}^{L-1} Z_{mn}^{(l)} . \tag{2.17}$$

where the interaction between the testing current and the l^{th} via is

$$Z_{mn}^{(l)} = \int_0^{2\pi} e^{-jm\phi_0'} e^{jn_i\phi_a l} e^{jn(\phi_l' - l\phi_a)} H_n^{(2)}\left(k\rho_l'\right)\left[-\pi\eta\left(\frac{ka}{2}\right) J_n\left(ka\right)\right] a\, d\phi_0' . \tag{2.18}$$

Two different cases need to be considered to evaluate (2.18), $l = 0$ and $l \neq 0$. First consider the $l = 0$ case,

$$Z_{mn}^{(0)} = \int_0^{2\pi} e^{-j(m-n)\phi_0'} H_n^{(2)}\left(k\rho_0'\right)\left[-\pi\eta\left(\frac{ka}{2}\right) J_n\left(ka\right)\right] a\, d\phi_0' . \tag{2.19}$$

Substituting $\rho_0{}' = a$ and using orthogonality, (2.18) reduces to

$$Z_{mn}^{(0)} = \left\{ \begin{array}{ll} 0 & m \neq n \\ 2\pi a H_n^{(2)}(ka)\left[-\pi\eta\left(\frac{ka}{2}\right) J_n(ka)\right] & m = n \end{array} \right\}. \tag{2.20}$$

Considering the more general $l \neq 0$ case in (2.18),

$$Z_{mn}^{(l)} = \left[-\pi\eta\left(\frac{ka}{2}\right) J_n(ka)\right] e^{j(n_i - n)\phi_{al}} \int_0^{2\pi} e^{-jm\phi_0'} e^{jn\phi_l'} H_n^{(2)}\left(k\rho_l{}'\right) a\, d\phi_0{}'. \tag{2.21}$$

Note that the integrand in (2.21) has two different coordinate system variables, $(\phi_0{}', \rho_0{}')$ for the reference via and $(\phi_l{}', \rho_l{}')$ for the l^{th} via, as shown in Figure 2.2. It is necessary to have the variables in the same coordinate system to obtain an analytical result.

2.2.3.1 Addition Theorem

The addition theorem [14] is used to displace the origin of the coordinate system where the Bessel function is defined. In other words it translates the Bessel function defined at point *A* to other Bessel functions defined at point *B* with a different order as shown in Figure 2.4. The general form of the addition theorem is given in (2.22), where the Hankel function of the second kind can be replaced with the first kind or with a combination and the identity is still valid

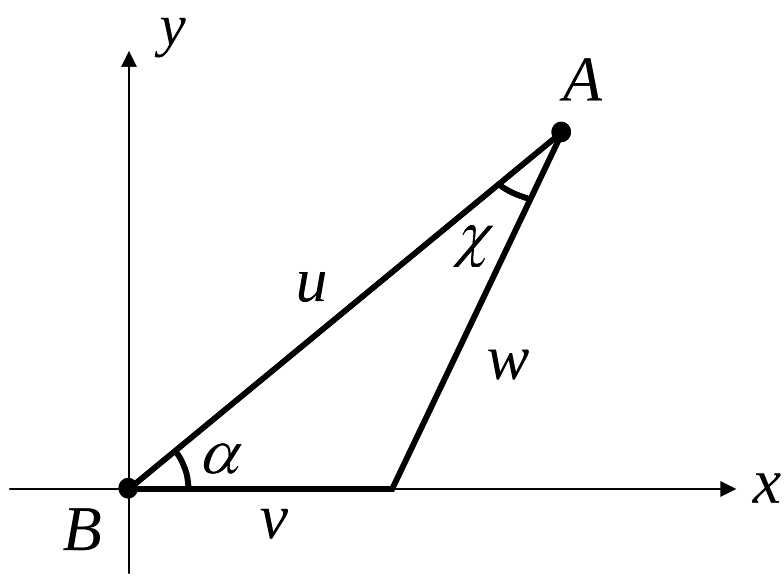

Figure 2.4. Addition theorem triangle.

$$H_n^{(2)}(w)e^{jn\chi} = \sum_{q=-\infty}^{\infty} H_{n+q}^{(2)}(u)\,J_q(v)\,e^{jq\alpha} \qquad (|v|<|u|)\,. \tag{2.22}$$

2.2.3.2 Addition Theorem for Z_{mn}

The addition theorem in (2.22) is be applied to the Z_{mn} equation in (2.21). In particular, the Hankel function expressed in terms of (ρ_l', ϕ_l') will be expressed in terms of (ρ_0', ϕ_0') in the reference via coordinate system.

As shown in Figure 2.5, placing the general addition theorem triangle given in Figure 2.4 into the problem geometry shown in Figure 2.2, the following equations are obtained:

$$w = k\rho_l', \tag{2.23}$$

$$u = 2kR\cos\left(\frac{\pi}{2} - l\frac{\pi}{L}\right), \tag{2.24}$$

$$v = k\rho_0', \tag{2.25}$$

$$\alpha = \frac{\pi}{2} + l\frac{\phi_a}{2} - \phi_0', \tag{2.26}$$

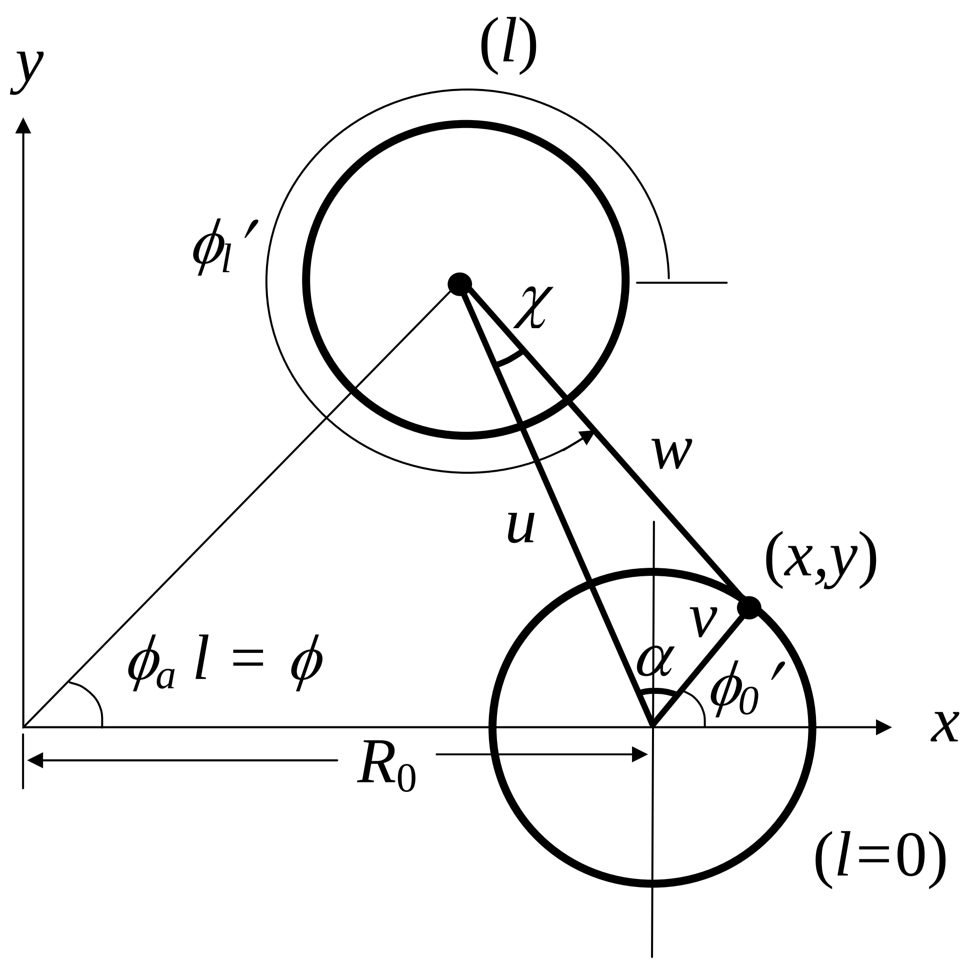

Figure 2.5. Application of addition theorem to Z_{mn}.

where

$$\chi = \phi_l' - 3\frac{\pi}{2} - l\frac{\phi_a}{2}. \tag{2.27}$$

Substituting these values into the addition theorem in (2.22) to obtain $H_n^{(2)}\left(k\rho_l'\right)e^{jn\phi_l'}$ in terms of the reference via coordinates, gives the result

$$H_n^{(2)}\left(k\rho_l'\right)e^{jn\phi_l'} = \sum_{q=-\infty}^{\infty} H_{n+q}^{(2)}\left(2kR\cos\left(\frac{\pi}{2} - l\frac{\pi}{L}\right)\right) J_q\left(k\rho_0'\right) j^{-n} j^q e^{j(q+n)l\frac{\phi_a}{2}} e^{-jq\phi_0'}. \tag{2.28}$$

Hence, (2.21) becomes

$$\begin{aligned} Z_{mn}^{(l)} = &\left[-\pi\eta\left(\frac{ka}{2}\right)J_n\left(ka\right)\right] a e^{j(n_i - n)\phi_a l} \\ &\cdot\int_0^{2\pi} j^{-n} e^{-jm\phi_0'}\left(\sum_{q=-\infty}^{\infty} e^{-jq\phi_0'} H_{n+q}^{(2)}\left(2kR\sin\frac{l\pi}{L}\right) j^q J_q\left(k\rho_0'\right) e^{j(q+n)l\frac{\phi_a}{2}}\right) d\phi_0'. \end{aligned} \tag{2.29}$$

From orthogonality, (2.29) is nonzero only when $q = -m$, thus

$$\begin{aligned} Z_{mn}^{(l)} = &\left[-\pi\eta\left(\frac{ka}{2}\right)J_n\left(ka\right)\right] 2\pi a j^{-(m+n)} J_{-m}\left(k\rho_0'\right) \\ &. e^{j(n_i - n)\phi_a l} e^{j(n-m)l\frac{\phi_a}{2}} H_{n-m}^{(2)}\left(2kR\sin l\frac{\pi}{L}\right). \end{aligned} \tag{2.30}$$

The final Z_{mn} term is obtained by combining (2.20) and (2.30) as

$$Z_{mn} = 2\pi a\left[-\pi\eta\left(\frac{ka}{2}\right)J_n\left(ka\right)\right]$$
$$\cdot\left\{H_n^{(2)}\left(ka\right)\delta(m,n) - j^{m+n}J_{-m}\left(k\rho_0'\right)\sum_{l=1}^{L-1}e^{j(n_i-n)\phi_a l}e^{j(n-m)l\frac{\phi_a}{2}}H_{n-m}^{(2)}\left(2kR\sin\frac{l\pi}{L}\right)\right\}. \tag{2.31}$$

2.2.3.3 Addition Theorem for b_m

Similar to the Z_{mn} application of the addition theorem, it is necessary to make the coordinate systems agree in the b_m equation, which is the right-hand side (RHS) of (2.13). In this equation, the Bessel function expressed in terms of the global coordinate system (ρ,ϕ) will be expressed in terms of (ρ_0', ϕ_0'), which again is the reference via coordinate system.

This time, the general addition theorem triangle shown in Figure 2.2 is oriented to shift the global coordinates into the reference via coordinate system as shown in Figure 2.6. The corresponding addition theorem equations are then

$$w = k\rho\,, \tag{2.32}$$

$$u = kR_0\,, \tag{2.33}$$

$$v = k\rho_0'\,, \tag{2.34}$$

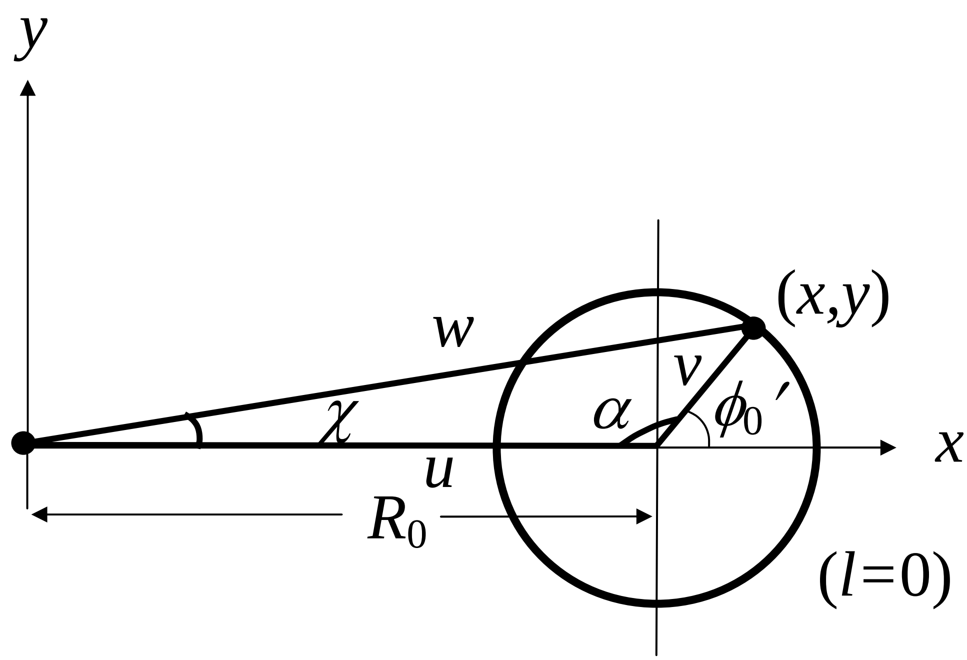

Figure 2.6. Application of addition theorem to b_m.

$$\alpha = \pi - \phi_0{}' , \tag{2.35}$$

$$\chi = \phi . \tag{2.36}$$

Substituting the above equations into the addition theorem given in (2.22) and using Bessel functions instead of Hankel functions yields

$$J_{n_i}\left(k\rho\right)e^{jn_i\phi} = \sum_{q=-\infty}^{\infty}(-1)^q J_{n_i+q}\left(kR_0\right)J_q\left(k\rho_0{}'\right)e^{-jq\phi_0{}'} . \tag{2.37}$$

Using the result in (2.37), b_m in (2.13) becomes

$$b_m = -2\int_0^{2\pi} e^{-jm\phi}\sum_{q=-\infty}^{\infty}(-1)^q\left(J_{n_i+q}\left(kR_0\right)J_q\left(k\rho_0{}'\right)e^{-jq\phi_0{}'}\right)a\,d\phi_0{}' . \tag{2.38}$$

Using orthogonality once again, b_m is nonzero only when $q = -m$, and hence

$$b_m = -4\pi a J_{n_i-m}\left(kR_0\right)J_m\left(ka\right). \tag{2.39}$$

2.2.3.4 EFIE Matrix Equation

Equation (2.13) is rewritten in matrix form as

$$\left[Z_{mn}\right]\left[a_n\right] = \left[b_m\right] \tag{2.40}$$

with the sizes of $(2N+1)\times(2N+1)$, $(2N+1)\times(1)$ and $(2N+1)\times(1)$ for Z_{mn}, a_n and b_m respectively, where $2N+1$ represents the number of basis functions. This matrix equation is used to solve for the a_n coefficients.

2.2.4 Exterior Reflection Coefficient (Γ_{EXT})

Once the current coefficients have been determined all the field quantities are known. The next important step is to find the reflection coefficient of the array. The reflection coefficient is defined as the ratio of the electric field amplitude propagating away from the via array with a variation $\exp\left(jn_i\phi\right)$, E_{z,n_i}^{AWAY}, to the electric field amplitude propagating toward the via array, E_z^{TOWARD}. For the circular via-array structure in Figure 2.3, the outgoing field, E_{z,n_i}^{AWAY}, is the summation of the reflected field from the z-axis, E_z^r, and the scattered field E_{z,n_i}^s. Therefore, the reflection coefficient is written as

$$\Gamma_{EXT} = \left.\frac{E_{z,n_i}^{AWAY}}{E_z^{TOWARD}}\right|_{\rho=R_0} = \left.\frac{E_z^r + E_{z,n_i}^s}{E_z^i}\right|_{\rho=R_0}. \tag{2.41}$$

Examining the field equations needed in (2.41) that are given by (2.5), (2.8) and (2.9), it can be seen that they are not expressed in the same coordinate system. Therefore, it is necessary again to use the addition theorem to express them in the same coordinate system to obtain an analytical expression for the reflection coefficient.

2.2.4.1 Addition Theorem for E_z^s

In this case the addition theorem will be is applied to (2.5), which is in the $(\rho_0{}', \phi_0{}')$ coordinate system, to yield E_z^s in the (ρ, ϕ) global coordinate system.

As before, the general addition theorem triangle given in Figure 2.2 is used to shift the l^{th} via coordinate system into the global coordinates as shown in Figure 2.7. The corresponding addition theorem equations are:

$$w = k\rho_l' , \tag{2.42}$$

$$u = k\rho , \tag{2.43}$$

$$v = kR_0 , \tag{2.44}$$

$$\alpha = \phi - l\phi_a , \tag{2.45}$$

$$\chi = \phi_l' - \phi . \tag{2.46}$$

Substituting the above equations into the addition theorem given in (2.22) yields

$$H_n^{(2)}\left(k\rho_l'\right)e^{jn\phi_l'} = \sum_{q=-\infty}^{\infty} H_{n+q}^{(2)}\left(k\rho\right)J_q\left(kR_0\right)e^{j(q+n)\phi}e^{-jql\phi_a} . \tag{2.47}$$

Substituting this result into (2.5), the final E_Z^S in global coordinates is

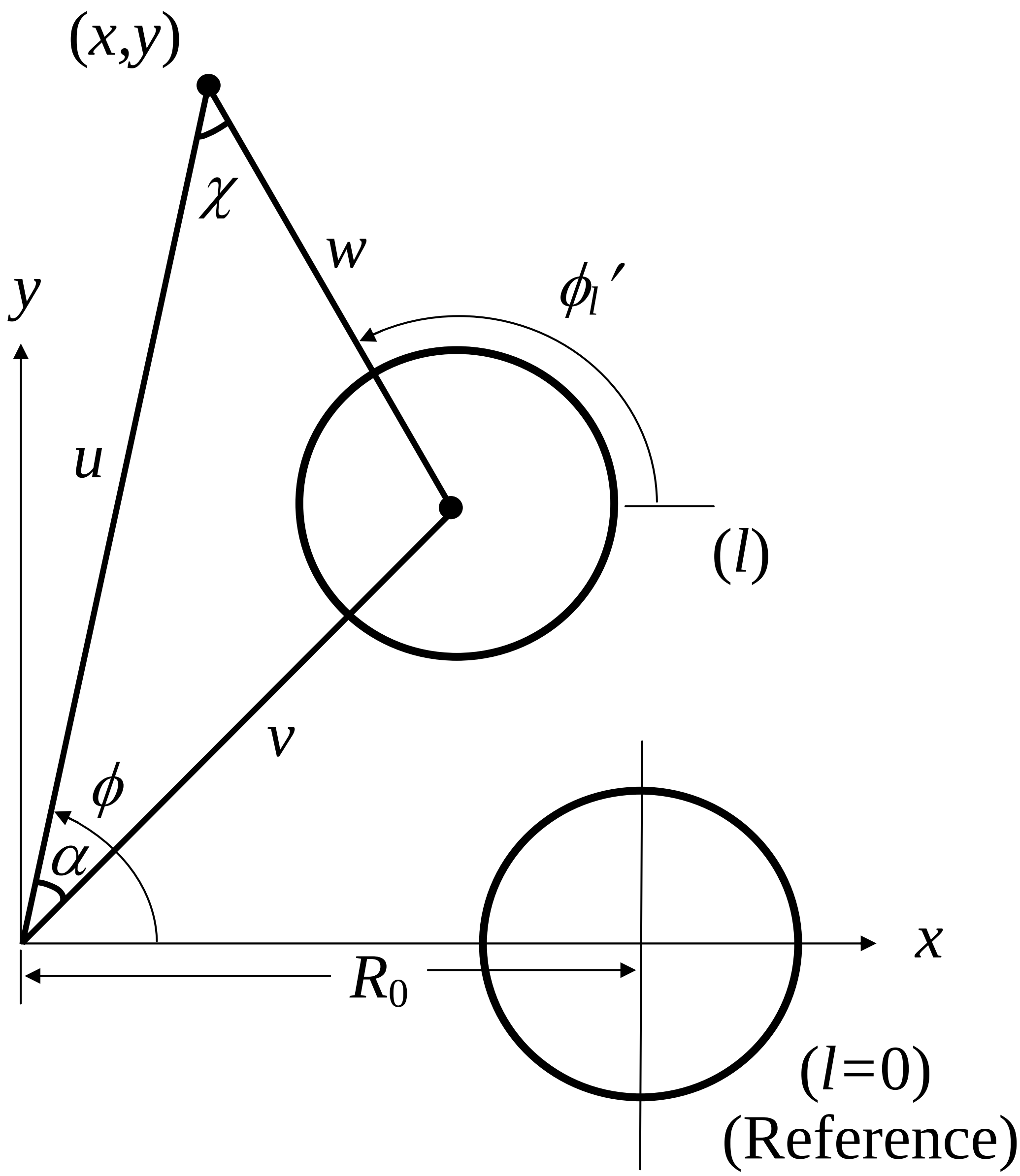

Figure 2.7. Application of addition theorem to E_z^s.

$$E_z^s(\rho,\phi)=\sum_{n=-N}^{N}\sum_{l=0}^{L-1}\sum_{q=-\infty}^{\infty}\left(a_n\left[-\pi\eta\left(\frac{ka}{2}\right)J_n(ka)\right]\right.$$
$$\left.\cdot\left(H_{n+q}^{(2)}(k\rho)J_q(kR_0)e^{j(q+n)\phi}e^{-j(q-n_i+n)l\phi_a}\right)\right). \tag{2.48}$$

Since the separation angle ϕ_a is the angle between vias, the summation over l in (2.47) simplifies as

$$\begin{aligned}\sum_{l=0}^{L-1}e^{-j(q-n_i+n)l\phi_a}&=\sum_{l=0}^{L-1}e^{-j(q-n_i+n)\frac{2\pi}{L}l}\\&=\begin{cases}L, & \text{when } q=n_i-n+pL,\ (p \text{ integer})\\0, & \text{otherwise.}\end{cases}\end{aligned} \tag{2.49}$$

Substituting $q=n_i-n+pL$ in (2.48) yields

$$E_z^s(\rho,\phi)=\sum_{n=-N}^{N}\sum_{p=-\infty}^{\infty}a_nL\left[-\pi\eta\left(\frac{ka}{2}\right)J_n(ka)\right]\left(H_{n_i+pL}^{(2)}(k\rho)J_{n_i-n+pL}(kR_0)e^{j(n_i+pL)\phi}\right). \tag{2.50}$$

The definition of reflection coefficient requires that all the fields should have the same azimuth variation, therefore p is set to zero to get the same $\exp(jn_i\phi)$ mode variation in the scattered field. Thus the scattered field component that varies as $\exp(jn_i\phi)$ is

$$E_{z,n_i}^s(\rho,\phi)=\sum_{n=-N}^{N}a_nL\left[-\pi\eta\left(\frac{ka}{2}\right)J_n(ka)\right]J_{n_i-n}(kR_0)H_{n_i}^{(2)}(k\rho)e^{jn_i\phi}. \tag{2.51}$$

2.2.4.2 Analytical Result for External Reflection Coefficient (Γ_{EXT})

The final formula for the external reflection coefficient at $\rho = R_0$ is written using (2.41), (2.5), (2.8) and (2.51) as

$$\Gamma_{EXT} = \frac{H_{n_i}^{(2)}\left(kR_0\right)\left(1+\left(\sum_{n=-N}^{N} a_n L\left[-\pi\eta\left(\frac{ka}{2}\right)J_n\left(ka\right)\right]J_{n_i-n}\left(kR_0\right)\right)\right)}{H_{n_i}^{(1)}\left(kR_0\right)}. \qquad (2.52)$$

2.2.5 Interior Reflection Coefficient (Γ_{INT})

There are many applications that require knowledge of the reflection coefficient looking from the inside of the via fence (interior reflection coefficient). The analysis of the interior reflection coefficient (Figure 2.8) is similar to that of exterior reflection coefficient.

The primary difference in the EFIE formulation is that b_m changes since the incident field E_z^i impinges on the via array from the interior. The Z_{mn} matrix is unaffected. Therefore, the resulting a_n coefficients and the usage of the addition theorem to determine the scattered field is different. From the geometry shown in Figure 2.8, the incident field is given by a Hankel function of the second kind as

$$E_z^i\left(\rho,\phi\right) = e^{jn_i\phi}H_{n_i}^{(2)}\left(k\rho\right). \qquad (2.53)$$

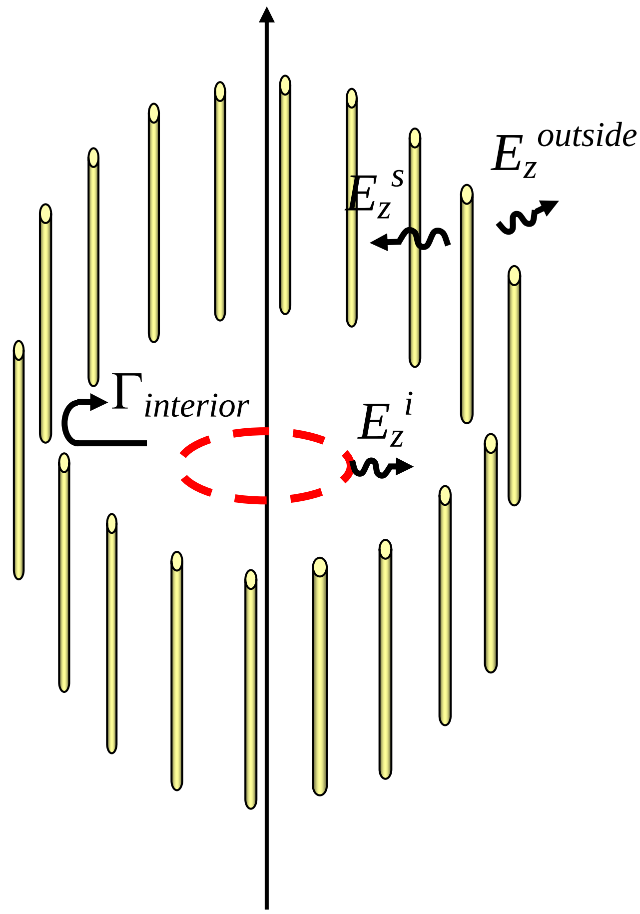

Figure 2.8. The incoming, reflected and the scattered fields for the via array to be used for calculating the interior reflection coefficient.

Since the general form of the scattered field is the same, (2.5) is valid for this case.

2.2.5.1 Electric Field Integral Equation (EFIE)

Similar to the analysis in Section 2.2.3, the EFIE equation is written for this interior reflection coefficient case by equating all the fields to zero on the reference via as

$$E_z^s(\rho,\phi) = -E_z^i(\rho,\phi) \qquad (\rho_0' = a)\,. \tag{2.54}$$

Multiplying both sides by the same testing function and then integrating (2.54) over the circumference of the reference via results in the same Z_{mn} values as the previous case, but different b_m values.

2.2.5.2 Addition Theorem for b_m

Using (2.53) in (2.54) and integrating over the reference via yields the following RHS formula

$$b_m = -\int_0^{2\pi} e^{-jm\phi} e^{jn_i\phi} H_{n_i}^{(2)}\left(k\rho\right) a d\phi_0' \qquad (\rho_0' = a)\,. \tag{2.55}$$

Similarly, the addition theorem is applied using Figure 2.6 to write

$$H_{n_i}^{(2)}\left(k\rho\right) e^{jn_i\phi} = \sum_{q=-\infty}^{\infty} (-1)^q H_{n_i+q}^{(2)}\left(kR_0\right) J_q\left(k\rho_0{}'\right) e^{-jq\phi_0'}\,. \tag{2.56}$$

Inserting (2.56) into (2.55) and using orthogonality, the final b_m formula for the interior problem is

$$b_m = -4\pi a H_{n_i-m}^{(2)}\left(kR_0\right) J_m\left(ka\right). \tag{2.57}$$

In this case, the new a_n current density coefficients can be found using (2.31) and (2.57) in the matrix equation (2.40).

2.2.5.3 Addition Theorem for E_z^s for Interior Reflection Coefficient

The addition theorem triangle shown in Figure 2.9 is oriented for interior problems so that it preserves the $|v| < |u|$ condition given in (2.22). The corresponding addition theorem equations are:

$$w = k\rho_l', \tag{2.58}$$

$$u = kR_0, \tag{2.59}$$

$$v = k\rho, \tag{2.60}$$

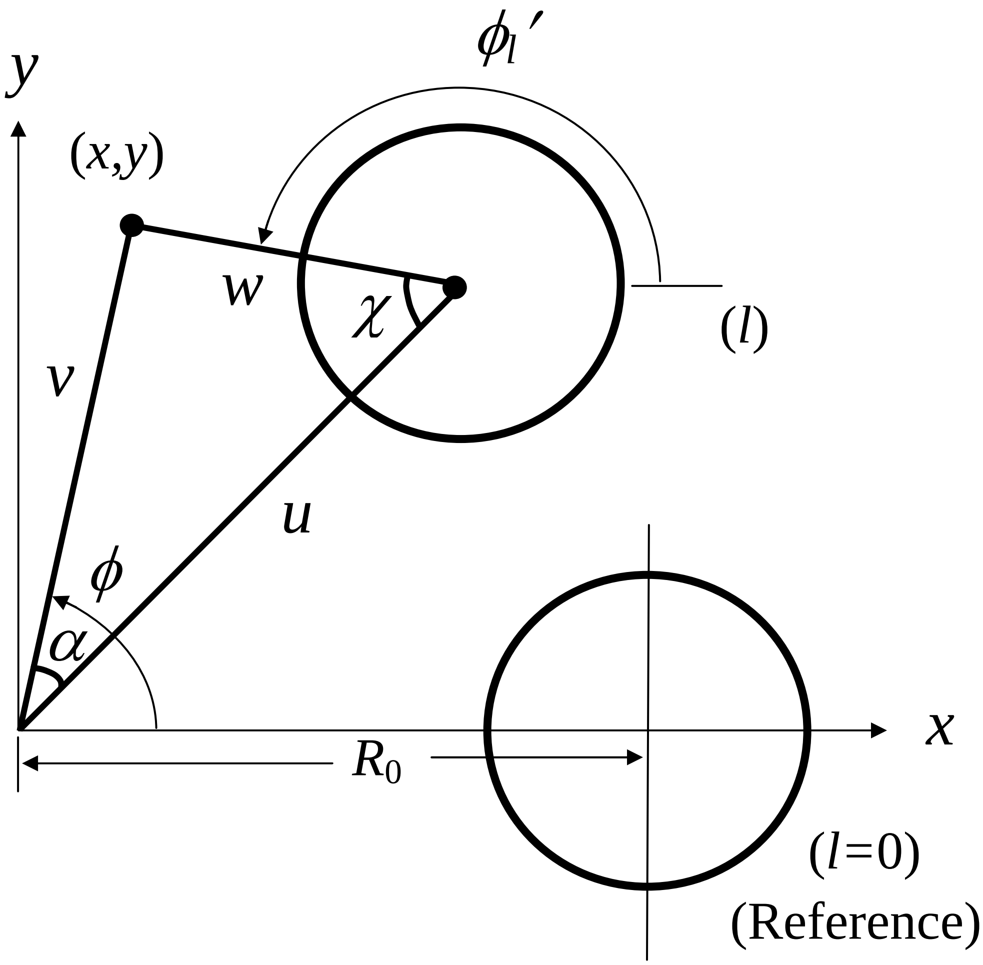

Figure 2.9. Application of addition theorem to E_z^s where the observation point lies inside the fence.

$$\alpha = \phi - l\phi_a, \tag{2.61}$$

$$\chi = \pi + l\phi_a - \phi_l'. \tag{2.62}$$

As before, the above equations are substituted into the addition theorem in (2.22) and the following result is obtained,

$$H_n^{(2)}\left(k\rho_l'\right)e^{jn\phi_l'} = \sum_{q=-\infty}^{\infty} H_{-n+q}^{(2)}\left(kR_0\right)J_q\left(k\rho\right)e^{jq\phi}e^{j(n-q)l\phi_a}. \tag{2.63}$$

After some algebra the result of substituting (2.63) in (2.5) yields the final form for the n_i component of the scattered field as

$$E_{z,n_i}^s\left(x,y\right) = \sum_{n=-N}^{N} a_n L\left[-\pi\eta\left(\frac{ka}{2}\right)J_n\left(ka\right)\right]\left(H_{n_i-n}^{(2)}\left(kR_0\right)J_{n_i}\left(k\rho\right)e^{jn_i\phi}\right). \tag{2.64}$$

Since the scattered field inside the via array is a standing wave, it can be decomposed into waves propagating toward to via array and propagating away from the via array, referenced to the interior face of the array, as follows:

$$E_{z.n_i}^{s,TOWARD}\left(x,y\right) = \sum_{n=-N}^{N} \frac{1}{2} a_n L\left[-\pi\eta\left(\frac{ka}{2}\right)J_n\left(ka\right)\right]\left(H_{n_i-n}^{(2)}\left(kR_0\right)H_{n_i}^{(2)}\left(k\rho\right)e^{jn_i\phi}\right), \tag{2.65}$$

$$E_{z,n_i}^{s,AWAY}\left(x,y\right) = \sum_{n=-N}^{N} \frac{1}{2} a_n L\left[-\pi\eta\left(\frac{ka}{2}\right)J_n\left(ka\right)\right]\left(H_{n_i-n}^{(2)}\left(kR_0\right)H_{n_i}^{(1)}\left(k\rho\right)e^{jn_i\phi}\right). \tag{2.66}$$

2.2.5.4 Analytical Result for Interior Reflection Coefficient (Γ_{INT})

The interior reflection coefficient is defined at $\rho = R_0$ as the ratio of the E_z component propagating away from the interior side of the via array relative to that propagating toward the interior side,

$$\Gamma_{INT} = \left.\frac{E_{z,n_i}^{AWAY}}{E_z^{TOWARD}}\right|_{\rho=R_0} = \left.\frac{E_{z,n_i}^{s,AWAY}}{E_z^i + E_{z,n_i}^{s,TOWARD}}\right|_{\rho=R_0} \tag{2.67}$$

where "AWAY" means the wave propagating away from the fence towards to the *z*-axis and "TOWARD" means the wave propagating toward (impinging on) the via array from the *z*-axis.

Using (2.53) and (2.64) in (2.65), the final form for the internal reflection coefficient is

$$\Gamma_{INT} = \frac{\frac{1}{2}\sum_{n=-N}^{N} a_n L\left[-\pi\eta\left(\frac{ka}{2}\right)J_n(ka)\right]\left(H_{n_i-n}^{(2)}(kR_0)\,H_{n_i}^{(1)}(kR_0)\right)}{H_{n_i}^{(2)}(kR_0)\left(1+\frac{1}{2}\sum_{n=-N}^{N} a_n L\left[-\pi\eta\left(\frac{ka}{2}\right)J_n(ka)\right]H_{n_i-n}^{(2)}(kR_0)\right)}. \tag{2.68}$$

2.3 Infinite Strip Model Analysis

For validation purposes another via model is also used. In this new model each cylinder is approximated as an infinitely long flat metallic strip as shown in Figure 2.10.

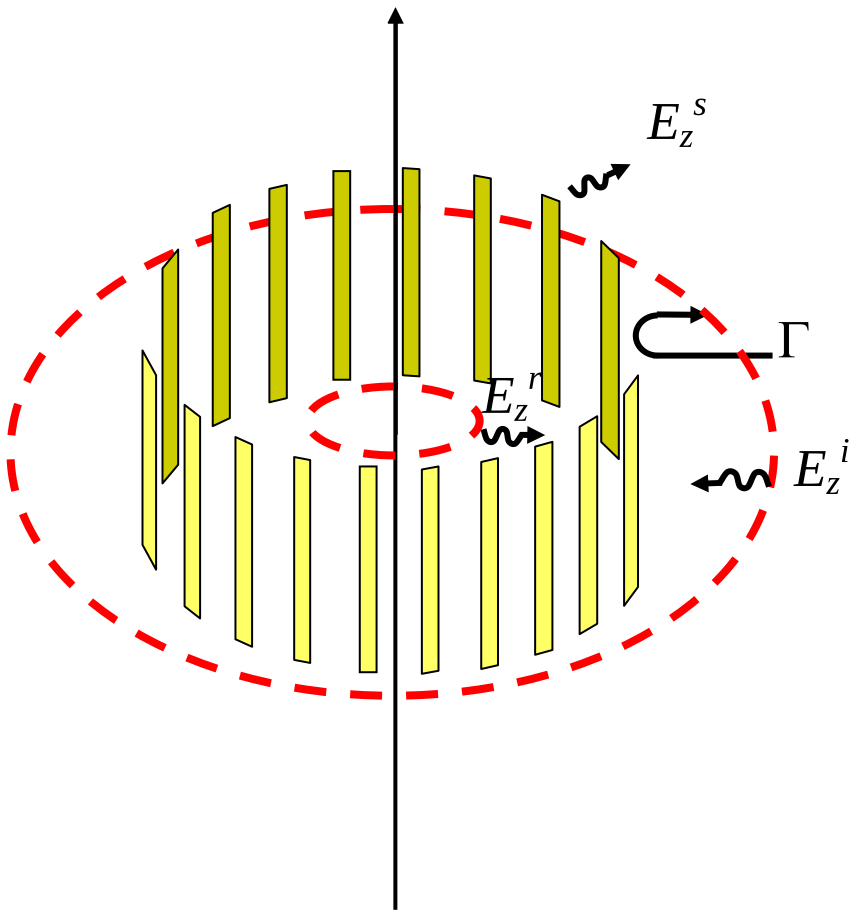

Figure 2.10. The infinitely long metallic strip model of the via array, showing the incoming, reflected and the scattered fields.

To make an equivalent strip array model, the width of each strip is chosen as [15]

$$w = ae^{3/2}, \tag{2.69}$$

which is consistent with the assumption of a uniform current on each strip. The analytical approach is the same as the circular via case.

2.3.1 Fourier Series Representation of the Current on the Strip Via Array

In this model the strip widths are very small because of the small radius of the vias; therefore the surface current on each strip is assumed to be constant in amplitude. The phase of the surface current on each via however differs by ϕ_a degrees from the adjacent via because of the induced current due to the incoming electric field given in (2.8). Therefore, the current density on each l^{th} via is written as

$$J_{sz}^{(l)} = J_{sz}^{(0)} e^{-jn_i l\phi_a}. \tag{2.70}$$

Finally the entire strip via array is modeled as a tube of current as shown in Figure 2.11. It is thus represented using a Fourier series as

$$J_{sz}(\phi) = \sum_{n=-\infty}^{\infty} c_n e^{jn\phi} \tag{2.71}$$

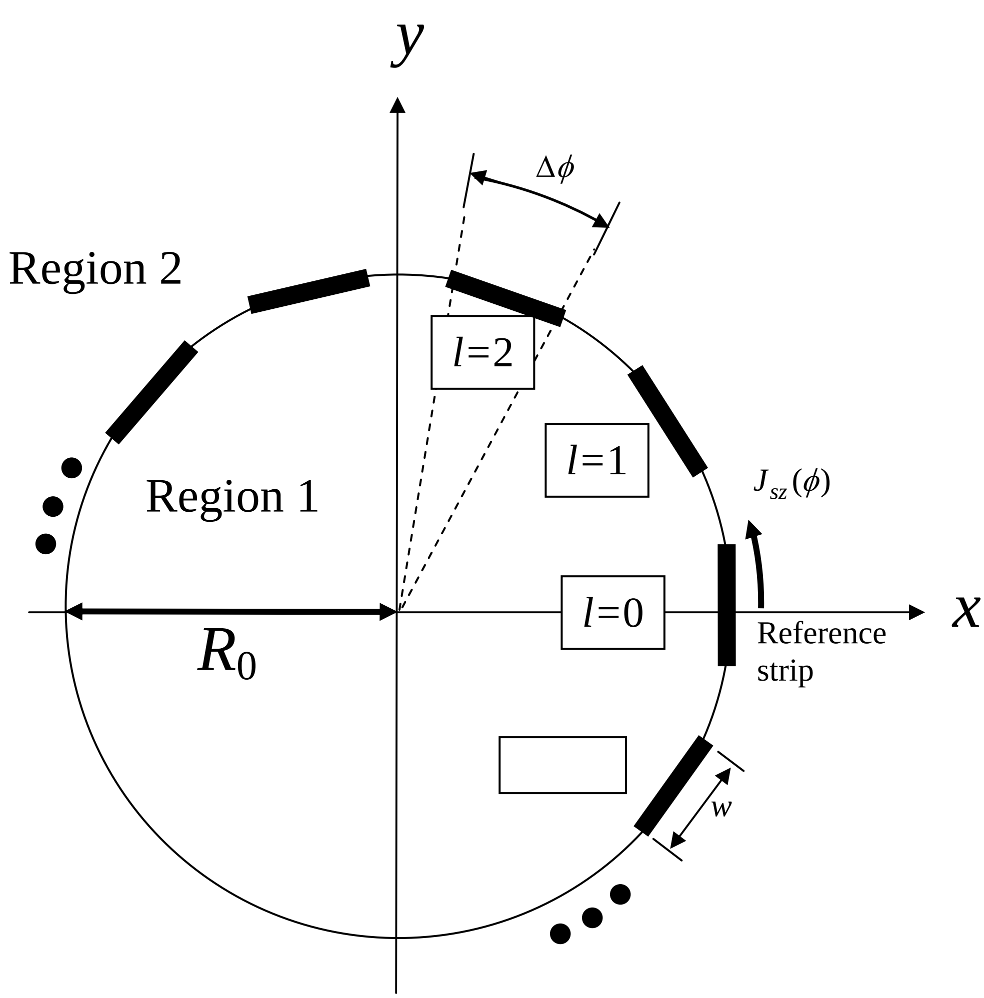

Figure 2.11. The tube of current modeling the via array represented with metallic strips.

where

$$c_n = \frac{1}{2\pi}\int_0^{2\pi} J_{sz}(\phi)\, e^{-jn\phi} d\phi. \tag{2.72}$$

The current on the l^{th} via, given in (2.70), is described by a pulse function so that

$$J_{sz}^{(l)}(\phi) = J_{sz0}\ \text{rect}\left(\frac{\phi - l\phi_a}{\Delta\phi}\right) e^{jn_i l\phi_a}, \tag{2.73}$$

where $\Delta\phi$ is the angular width of the strip. Therefore, the total array current is represented as

$$J_{sz}(\phi) = \sum_{l=0}^{L-1} J_{sz0}\ \text{rect}\left(\frac{\phi - l\phi_a}{\Delta\phi}\right) e^{jn_i l\phi_a}. \tag{2.74}$$

The inverse Fourier transform is found using (2.74) in (2.72) as

$$c_n = J_{sz0}\frac{\Delta\phi}{2\pi}\text{sinc}\left(\frac{n\Delta\phi}{2}\right)\frac{1 - e^{j(n_i - n)\phi_a L}}{1 - e^{j(n_i - n)\phi_a}}. \tag{2.75}$$

Since $\phi_a L = 2\pi$, (2.75) is simplified as

$$c_n = \begin{cases} L J_{sz0}\dfrac{\Delta\phi}{2\pi}\text{sinc}\left(\dfrac{n\Delta\phi}{2}\right) & \text{if} \quad (n_i - n)\phi_a = 2\pi p, \quad p = \ldots -1, 0, 1, 2\ldots \\ 0 & \text{otherwise.} \end{cases} \tag{2.76}$$

2.3.2 Spectral Domain Analysis

The strip via structure is analyzed using vector potentials and spectral domain analysis. The z-component of the vector potentials inside and outside of the via array are written as

$$A_{z1} = \sum_{n=-\infty}^{\infty} d_n \, e^{jn\phi} J_n(k\rho) \qquad (\rho < R_0)\,, \tag{2.77}$$

$$A_{z2} = \sum_{n=-\infty}^{\infty} e_n \, e^{jn\phi} H_n^{(2)}(k\rho) \qquad (\rho > R_0)\,, \tag{2.78}$$

where the coefficients d_n and e_n are obtained by enforcing the electromagnetic field boundary conditions at $\rho = R_0$, yielding

$$d_n = -j\pi\mu\left(\frac{R_0}{2}\right) c_n H_n^{(2)}(kR_0)\,, \tag{2.79}$$

$$e_n = -j\pi\mu\left(\frac{R_0}{2}\right) c_n J_n(kR_0)\,. \tag{2.80}$$

Using (2.80) along with (2.76) the vector potential outside of the array in (2.78) becomes

$$A_{z2} = -\sum_{n=-\infty}^{\infty} j J_{sz0}\, \pi\mu L \,\frac{R_0\,\Delta\phi}{4\pi} e^{jn\phi} \,\mathrm{sinc}\left(\frac{n\,\Delta\phi}{2}\right) J_n(kR_0)\, H_n^{(2)}(k\rho)\,. \tag{2.81}$$

Using c_n from (2.76) and inserting $n = n_i - \dfrac{2\pi p}{\phi_a} = n_i - Lp$ in (2.81) yields the following nonzero terms:

$$A_{z2} = -\sum_{p=-\infty}^{\infty} j J_{sz0}\, \pi\mu L \frac{R_0\,\Delta\phi}{4\pi} e^{jn_i\phi} \operatorname{sinc}\left(\frac{(n_i - Lp)\Delta\phi}{2}\right) J_{n_i - Lp}(kR_0)\, e^{-jLp\phi} H^{(2)}_{n_i - Lp}(k\rho). \quad (2.82)$$

The scattered field outside the strip array, found from (2.82), is

$$E_z^s = -\sum_{p=-\infty}^{\infty} J_{sz0}\, \pi\mu\omega L \frac{R_0\,\Delta\phi}{4\pi} \operatorname{sinc}\left(\frac{(n_i - Lp)\Delta\phi}{2}\right) J_{n_i - Lp}(kR_0)\, e^{j(n_i - Lp)\phi} H^{(2)}_{n_i - Lp}(k\rho). \quad (2.83)$$

This field expression is a Floquet Series [16]. Note that the scattered electric field equation in (2.83) has an unknown current density amplitude coefficient J_{sz0}, which is solved for by using the EFIE method as presented in the following section. Even though (2.83) is valid for all integer p values, p is eventually be chosen to be zero since all the fields should have the same mode variation $e^{jn_i\phi}$ as the incoming field in the reflection coefficient formula.

2.3.3 Electric Field Integral Equation (EFIE)

To find the unknown current amplitude J_{sz0}, the EFIE method is implemented in a similar fashion as in Section 2.2.3. The EFIE equation in (2.10) is valid for this case, with the incoming field given by (2.8), the reflected field by (2.9) and the scattered field by (2.83).

To solve this equation a unit pulse testing function running over the strip width at the reference position is used. The result is

$$-\int_{-\frac{\Delta\phi}{2}}^{\frac{\Delta\phi}{2}} J_{sz0}\,\pi\mu\omega L\,\frac{R_0\,\Delta\phi}{4\pi}\operatorname{sinc}\left(\frac{n_i\,\Delta\phi}{2}\right)J_{n_i-Lp}(kR_0)\,e^{jn_i\phi}H_{n_i}^{(2)}(k\rho)d\phi$$
$$=-\int_{-\frac{\Delta\phi}{2}}^{\frac{\Delta\phi}{2}} 2e^{jn_i\phi}J_{n_i}\left(kR_0\right)R_0 d\phi. \tag{2.84}$$

This equation is solved in closed form to give

$$J_{sz0}=\frac{8J_{n_i}\left(kR_0\right)}{\mu\omega L R_0\,\Delta\phi\operatorname{sinc}\left(\frac{n_i\,\Delta\phi}{2}\right)J_{n_i}(kR_0)H_{n_i}^{(2)}(k\rho)}. \tag{2.85}$$

With J_{sz0} determined, E_z^s in (2.83) is known and the reflection coefficient for the strip array defined by (2.41) can be calculated.

2.4 Equivalent Exterior Sheet Impedance Model

After finding the reflection coefficient for the via array using either of the methods described in Sections 2.2 or 2.3, the reflection coefficients can be converted to an equivalent sheet impedance that can replace the array of vias for modeling purposes. Modeling the array with an impedance sheet at the radius of the via array allows the structure to be analyzed more readily when using mode-matching or cavity-model approaches.

To find the equivalent sheet impedance for the via array, the simple model given Figure 2.12 is used. In this analysis the incoming field is chosen to be the same as (2.8). The total E_z fields outside and inside the sheet are:

$$E_z^{OUT}\left(\rho,\phi\right) = Be^{jn_i\phi} H_{n_i}^{(2)}\left(k\rho\right), \tag{2.86}$$

$$E_z^{IN}\left(\rho,\phi\right) = Ae^{jn_i\phi} J_{n_i}\left(k\rho\right), \tag{2.87}$$

where A and B are unknowns determined by applying the boundary conditions. The definition of sheet impedance is

$$Z_{sh} = \left.\frac{E_z}{J_{sz}}\right|_{\rho=R_0} = \left.\frac{E_z}{H_\phi^{OUT} - H_\phi^{IN}}\right|_{\rho=R_0}. \tag{2.88}$$

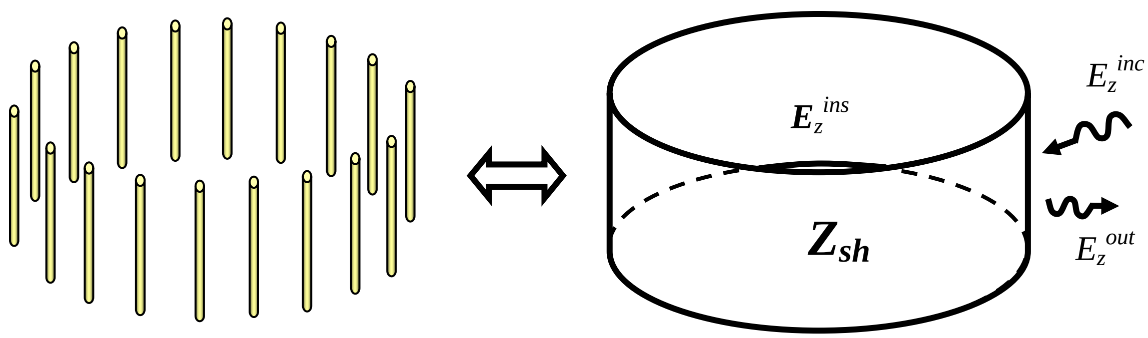

Figure 2.12. The equivalent sheet impedance model of the via array.

The reflection coefficient in (2.41) becomes

$$\Gamma_{EXT} = B\frac{H_{n_i}^{(2)}\left(kR_0\right)}{H_{n_i}^{(1)}\left(kR_0\right)}. \tag{2.89}$$

Using the boundary conditions for electric and magnetic fields at $\rho = R_0$ gives

$$Z_{sh,EXT} = \frac{j\eta J_{n_i}\left(kR_0\right)\left[H_{n_i}^{(1)}\left(kR_0\right) + BH_{n_i}^{(2)}\left(kR_0\right)\right]}{\left(\begin{array}{c}\left[J_{n_i}\left(kR_0\right)H_{n_i}^{(1)\prime}\left(kR_0\right) - J_{n_i}{}'\left(kR_0\right)H_{n_i}^{(1)}\left(kR_0\right)\right] \\ +B\left[J_{n_i}\left(kR_0\right)H_{n_i}^{(2)\prime}\left(kR_0\right) - J_{n_i}{}'\left(kR_0\right)H_{n_i}^{(2)}\left(kR_0\right)\right]\end{array}\right)}. \tag{2.90}$$

Using the Wronskian Identity [2] and (2.89), the sheet impedance in (2.90) is simplified and represented in terms of the exterior reflection coefficient Γ_{EXT} as

$$Z_{sh,EXT} = \frac{\eta\left(\dfrac{\pi}{2}\right)\left(kR_0\right)J_{n_i}\left(kR_0\right)H_{n_i}^{(1)}\left(kR_0\right)\left(1+\Gamma_{EXT}\right)}{1-\Gamma_{EXT}\left(\dfrac{H_{n_i}^{(1)}\left(kR_0\right)}{H_{n_i}^{(2)}\left(kR_0\right)}\right)}. \tag{2.91}$$

It is noted from (2.90) and (2.89) that $Z_{sh,EXT} \to 0$ as $\Gamma_{EXT} \to -1$, which is the PEC boundary case and

$Z_{sh,EXT} \to \infty$ for $\Gamma_{EXT} = \dfrac{H_{n_i}^{(2)}\left(kR_0\right)}{H_{n_i}^{(1)}\left(kR_0\right)}$ which is the open boundary (no via array) case.

If it is assumed there is no power is radiated into the other modes and there are no losses, the magnitude of the exterior reflection coefficient is equal to 1. Then (2.91) becomes

$$Z_{sh,EXT} = j\eta\left(\frac{\pi}{2}\right)(kR_0)J_{n_i}(kR_0)\left|H_{n_i}^{(1)}\left(kR_0\right)\right|\left[\frac{\cos(\phi/2)}{\sin(\psi+\phi/2)}\right] \tag{2.92}$$

where $\phi = \angle\Gamma$ and $\psi = \angle H_{n_i}^{(1)}(kR)$.

2.5 Equivalent Exterior Surface Impedance Model

Similar to the equivalent sheet impedance analysis in Section 2.4, an equivalent surface impedance can also be found. The only difference in the analysis is the definition of surface impedance, which is given as

$$Z_{sur,EXT} = \left.\frac{E_z}{H_\phi^{OUT}}\right|_{\rho=R_0}. \tag{2.93}$$

From the results of the previous section, the equivalent surface impedance, expressed in terms of the reflection coefficient, is

$$Z_{sur,EXT} = \frac{j\eta J_{n_i}\left(kR_0\right)\left[H_{n_i}^{(1)}\left(kR_0\right)+\Gamma_{EXT}H_{n_i}^{(1)}\left(kR_0\right)\right]}{\left[\Gamma_{EXT}J_{n_i}\left(kR_0\right)H_{n_i}^{(2)\prime}\left(kR_0\right)\dfrac{H_{n_i}^{(1)}\left(kR_0\right)}{H_{n_i}^{(2)}\left(kR_0\right)}+J_{n_i}\left(kR_0\right)H_{n_i}^{(1)\prime}\left(kR_0\right)\right]} \tag{2.94}$$

where the derivatives are defined with respect to the argument.

Another way to think about the surface impedance is as the parallel combination of the sheet impedance and the impedance of the interior region as shown in Figure 2.13,

$$Z_{sur,EXT} = \frac{1}{\dfrac{1}{Z_{sh}} + \dfrac{1}{Z_{core}}}, \tag{2.95}$$

where Z_{core} is the ratio of the electric field to the magnetic field at $\rho = \rho_0$, which is

$$Z_{core} = \frac{j\eta J_{n_i}\left(kR_0\right)}{J_{n_i}{}'\left(kR_0\right)}. \tag{2.96}$$

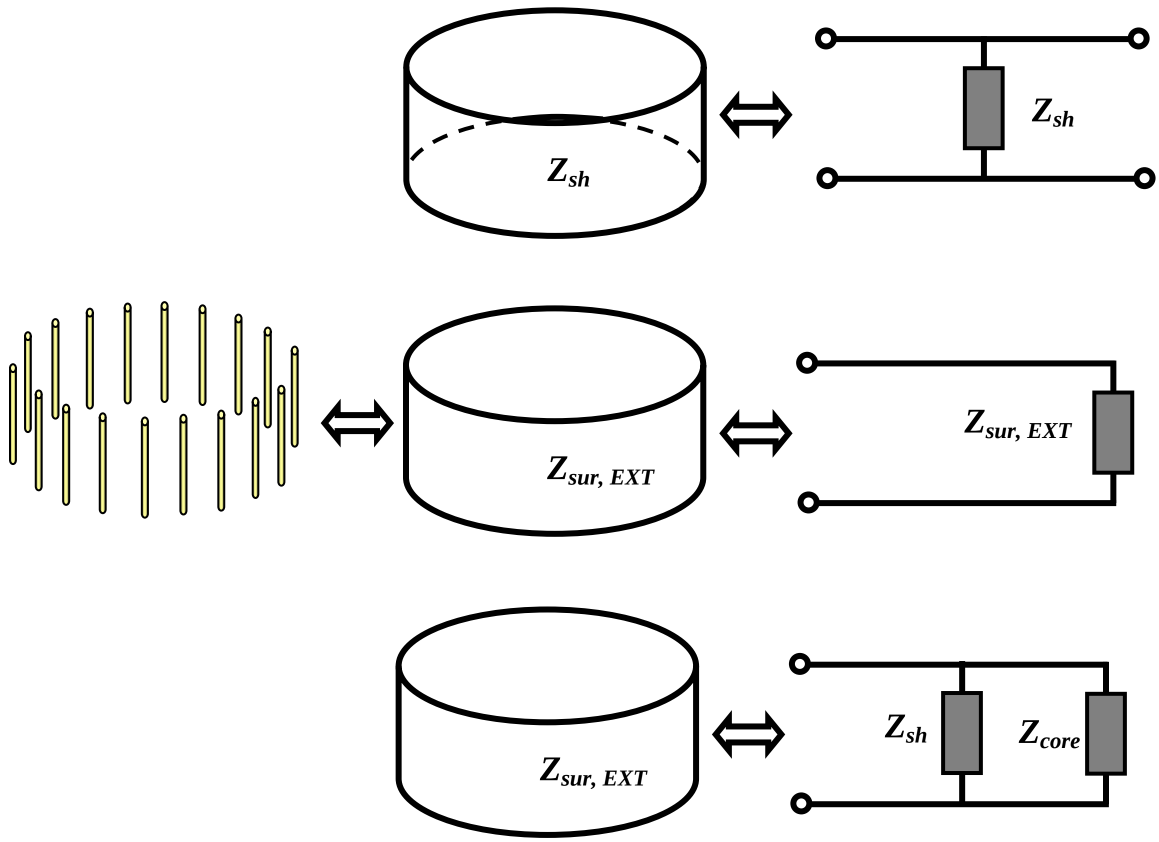

Figure 2.13. The equivalent exterior sheet impedance model of the via array.

2.6 Equivalent Interior Sheet Impedance Model

The equivalent sheet impedance for the interior problem is derived in a similar fashion as the exterior problem in Section 2.4. To find the equivalent interior sheet impedance, the model given Figure 2.14 is used. In this analysis the incident field is chosen to be the same as (2.53), so that the total scattered field inside the cavity is given by (2.64) and the field outside the sheet is

$$E_z^{OUT}\left(\rho,\phi\right) = Ae^{jn_i\phi}H_{n_i}^{(2)}\left(k\rho\right), \tag{2.97}$$

where A is an unknown to be determined using the boundary conditions. Using the following definition for the sheet impedance:

$$Z_{sh,INT} = \left.\frac{E_z}{J_{sz}}\right|_{\rho=R_0} = \left.\frac{E_z}{H_\phi^{OUT} - H_\phi^{IN}}\right|_{\rho=R_0}. \tag{2.98}$$

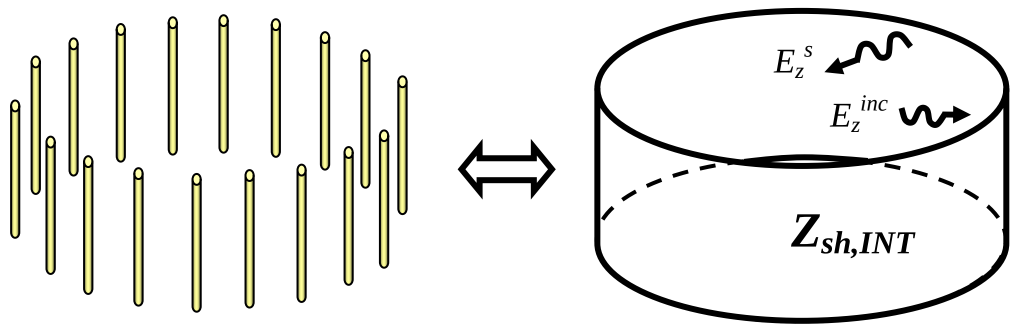

Figure 2.14. The equivalent interior sheet impedance model of the via array.

Solving for these fields as before and simplifying,

$$Z_{sh,INT} = \frac{\eta\pi(kR_0)H_{n_i}^{(2)}\left(kR_0\right)\left[H_{n_i}^{(1)}\left(kR_0\right)-\Gamma_{INT}\left(H_{n_i}^{(2)}\left(kR_0\right)-2J_{n_i}\left(kR_0\right)\right)\right]}{4\Gamma_{INT}}, \quad (2.99)$$

where Γ_{INT} is given by (2.68).

It can be seen from (2.99) that $Z_{sh,INT} \to \infty$ as $\Gamma_{INT} \to 0$, which is the open-circuit boundary (no via array) case and $Z_{sh,INT} \to 0$ for $\Gamma_{INT} \to -1$, which is short-circuit boundary (PEC) case.

Chapter 3
Loss Calculations in Via Array

3.1 Introduction

Since the materials used in microstrip antennas are not perfect conductors there is always a certain amount of loss present due to the power dissipated in the top and bottom conductor of the microstrip antenna. This chapter investigates the losses that occur due to the array of vias used in the antenna. Losses in the vias become important when they are comparable to the losses in the top and bottom conductors of the antenna.

3.2 Approximate Sheet Resistance Formula

The resistance of a single via is written as

$$R_{via} = \frac{R_{sur}^{m} h}{2\pi a}, \tag{3.1}$$

where h is the height of the via, a is the radius of the via and R_{sur}^{m} is the surface resistance of the metal used. Assuming no interactions between vias, the sheet resistance of the array is approximated as

$$R_{sur,\,array} \approx \frac{2\pi R_0}{hL} R_{via} = \frac{R_0}{aL} R_{sur}^{m}\,, \tag{3.2}$$

where R_0 is the radius of the array.

3.3 Loss Analysis

The power dissipated in the array is calculated in two ways: One is summing up all the powers lost in each via, and the other is determining the power lost in the sheet impedance model that represents the via array.

The power dissipated on one via due to conductive loss is written as

$$P_c^{via} = \frac{R_{sur}^{m}}{2} h \int_0^{2\pi} \left| J_{sz}(\phi) \right|^2 a\, d\phi\,, \tag{3.3}$$

where R_{sur}^{m} is the surface resistivity of the metal of the vias, and *a* is the radius of the via. Using the surface current density, $J_{sur,z}(\phi)$ on the via given in (2.3), (3.3) is written as

$$P_c^{via} = \pi a h R_{sur}^{m} \sum_{n=-N}^{N} \left| a_n \right|^2\,, \tag{3.4}$$

where h is the height of the vias and the a_n coefficients are the current basis function coefficients, found using the EFIE discussed in Chapter 2. The total power lost in the array is then simply the multiplication of this power by the number of vias L,

$$P_c^{array} = L\pi a h R_{sur}^m \sum_{n=-N}^{N} |a_n|^2 \, . \tag{3.5}$$

The other method to compute the loss is using the equivalent sheet conductance G_{sh} of the via array discussed in Section 2.4,

$$P_c^{array} = \frac{1}{2} G_{sh} \int_S |E_z|^2 \, dS \, , \tag{3.6}$$

where E_z is the total field on the surface of the sheet model of the array. Using the field inside the cavity given in (2.87) as the total field, since it is continuous across the boundary, (3.6) is re-written as

$$P_c^{array} = G_{sh} \, \pi |A|^2 \left| J_{n_i}\left(kR_0\right)\right|^2 R_0 h \, , \tag{3.7}$$

where the coefficient A is found using the fields given in (2.8), (2.86) and (2.87) and the boundary conditions as

$$A = \frac{H_{n_i}^{(1)}\left(kR_0\right)H_{n_i}^{(2)\prime}\left(kR_0\right) - H_{n_i}^{(1)\prime}\left(kR_0\right)H_{n_i}^{(2)}\left(kR_0\right)}{J_{n_i}\left(kR_0\right)H_{n_i}^{(2)\prime}\left(kR_0\right) - j(\eta / Z_s)J_{n_i}\left(kR_0\right)H_{n_i}^{(2)}\left(kR_0\right) - J_{n_i}{}'\left(kR_0\right)H_{n_i}^{(2)}\left(kR_0\right)}. \quad (3.8)$$

The sheet conductance G_{sh}, is related to sheet resistance R_{sh} by using the general relation

$$G_{sh} + jB_{sh} = \frac{1}{R_{sh} + jX_{sh}}. \quad (3.9)$$

Assuming $R_{sh} \ll \left|X_{sh}\right|$,

$$G_{sh} \approx \frac{R_{sh}}{X_{sh}^2}. \quad (3.10)$$

Instead of the sheet values that are used in (3.9), surface values can also be used in the same manner as

$$G_{sur} + jB_{sur} = \frac{1}{R_{sur} + jX_{sur}}. \quad (3.11)$$

Then the surface conductance is approximated as

$$G_{sur} \approx \frac{R_{sur}}{X_{sur}^2}. \quad (3.12)$$

Since the surface conductance of the via array is the summation of the sheet conductance of the via array and the surface conductance of the lossless interior region, which is zero, the sheet and surface conductances are equal. Then (3.10) and (3.12) are combined as

$$G_{sh} = G_{sur} \approx \frac{R_{sh}}{X_{sh}^2} \approx \frac{R_{sur}}{X_{sur}^2}. \tag{3.13}$$

Then (3.7) is written as

$$P_c^{array} = \frac{R_{sh}}{X_{sh}^2} \pi |A|^2 \left| J_{n_i} \left(kR_0 \right) \right|^2 R_0 h \tag{3.14}$$

or

$$P_c^{array} = \frac{R_{sur}}{X_{sur}^2} \pi |A|^2 \left| J_{n_i} \left(kR_0 \right) \right|^2 R_0 h \, . \tag{3.15}$$

Equating (3.5) and (3.14) or (3.15), and using the current coefficients and reactance values from the via analysis, the equivalent sheet resistance or surface resistance is solved for, respectively.

Another representation for the dissipated power of the array is obtained from (3.3) as

$$P_c^{array} = \frac{1}{2} R_{sur} \int_S \left| J_{sur,z} \right|^2 dS \tag{3.16}$$

where $J_{sur,z}$ is the surface current density on the equivalent surface impedance of the via array. It is found using field analysis as

$$J_{sur,z}(\phi) = \frac{-k}{j\omega\mu} \left[H_{n_i}^{(1)\prime}(kR_0) + \Gamma \frac{H_{n_i}^{(2)\prime}(kR_0) H_{n_i}^{(1)}(kR_0)}{H_{n_i}^{(2)}(kR_0)} \right] e^{jn_i\phi} . \tag{3.17}$$

If there are an infinite number of vias, the reflection coefficient Γ goes to -1 and (3.17) becomes

$$J_{sur,z}(\phi) = \frac{-k}{j\omega\mu} \frac{1}{H_{n_i}^{(2)}(kR_0)} \frac{4j}{\pi k R_0} e^{jn_i\phi} . \tag{3.18}$$

3.4 Analytical Results

The equivalent sheet and surface resistance values corresponding to a via array are calculated. The parameters of the chosen via-array geometry are given in Table 3.1. Equating (3.5) and (3.14) the corresponding sheet resistance is found as

$$R_{sh} = 0.03417 \quad \text{Ohm/sq} . \tag{3.19}$$

The surface resistance is also found by equating (3.5) and (3.15) as

Table 3.1. The via-array parameters used in the loss calculations.

Definition of the Variable	Symbol	Value
Radius of the via elements	a	0.3175 mm
Radius of the via array	R_0	32.029 mm
Height of the via array	h	1.524 mm
Number of current basis functions	$2N+1$	25
Frequency	f	1.575 GHz
Mode number of the incoming wave	n_i	1
Number of via elements	L	32
The permittivity of the medium	ε_r	1
The surface resistance of copper	$R_{sur}^{\ m}$	0.01034 Ohm/sq
The conductivity of copper	σ	5.8 10^7 Mho/m

$$R_{sur} = 0.03408 \quad \text{Ohm/sq}\,. \tag{3.20}$$

The approximate surface resistance formula in (3.2) gives

$$R_{sur,approx} = 0.0326 \quad \text{Ohm/sq} \tag{3.21}$$

for the same geometry given in Table 3.1.

3.5 HFSS Loss Simulations

The via-array geometry in Table 3.1 inside of a circular cavity with a PMC outer wall of radius 5.5778 cm is simulated by using HFSS with copper material having a finite conductivity of 5.8 10^7 Mhos/m. Using the eigenvalue feature of the HFSS program, the complex resonance frequencies and the corresponding Q values of the via array are obtained for different modes.

The resonance frequency of the via array given in Table 3.1 for the $n_i = 1$ mode is found as

$$f_{res} = 1.599 + j0.00017593 \quad \text{GHz}. \tag{3.22}$$

The Q value, which is related to the complex frequency, is found as

$$Q = \frac{\mathrm{Re}(f_{res})}{2\,\mathrm{Im}(f_{res})} = 4547. \tag{3.23}$$

To validate the analytical results found in Section 3.4, the surface impedance wall at the same via-array radius is simulated in HFSS using the calculated surface resistance and surface reactance values as

$$Z_{sur} = R_{sur} + jX_{sur} = 0.03417 + j14.037. \tag{3.24}$$

Using the surface impedance in (3.24) in HFSS, the corresponding Q value is found as

$$Q = 4758.9\,. \tag{3.25}$$

This value is slightly different than the one found from via array, showing the validity of the analytical calculations. The corresponding surface impedance value is also found by trial and error in HFSS to obtain the same Q value in (3.23) as

$$Z_{sur} = 0.03576 + j14.037\,. \tag{3.26}$$

The importance of the real part of the surface impedance or the loss is understood by comparing the loss occurring on the surface of the via array and the loss in the top and bottom conductors.

The same geometry is simulated in HFSS again using lossy top and bottom conductors having the actual conductivity of the copper but with a lossless via array. Then the corresponding Q is found to be

$$Q = 922.76 \tag{3.27}$$

which is approximately five times smaller than the Q value of the via array given in (3.23), meaning the loss occurring in the top and bottom conductors is five times the loss occurring in the via array for the specific geometry given in Table 3.1.

Chapter 4
Results for Reflection Coefficients, Sheet and Surface Impedances of a Circular Via Array

4.1 Introduction

In this chapter, numerical results for the analytical formulas covered in Chapter 2 are presented and results for the reflection coefficient, sheet impedance and surface impedance values from different calculation methods such as the cylindrical via model, the strip model, and HFSS simulations are compared.

First, results from the analytical reflection coefficient formulas for the cylindrical and strip array models are compared. This comparison includes the variation of the external reflection coefficient with different numbers of via elements for an air case and for a dielectric case for different radii of the vias and different radii of the via array. The convergence of the current coefficients with the number of basis functions in the analytical calculations is also demonstrated. Finally, results from the interior reflection coefficient are compared with values from the external one.

To gain confidence in the analytical formulations, additional comparisons are done using the Ansoft HFSS electromagnetic simulation program. Two different types of test cavities were created, one of which is a PMC cavity (a cylindrical cavity with PEC at the top and the bottom and a PMC wall on the side) with an array of vias inside it, and the other is a

PEC cavity (a cylindrical cavity with PEC at the top, bottom and on the side) with the same array of vias inside. Then these cavities are simulated in HFSS to find the resonance frequencies using the eigenvalue feature of HFSS. Afterwards, the analytical models are created for the same cavities using the equivalent sheet impedance wall models of the via array. Then the resonance frequencies of these analytical test cavities are calculated and compared with those of the test cavities simulated in HFSS. The good agreement in the comparison of the results shows how well the modeling of the actual via array with an equivalent sheet impedance wall is working.

Modeling the via array as a sheet or surface impedance is more practical for many applications. Therefore, the reflection coefficient values are converted to sheet and surface impedance values using the analysis in Chapter 2. The reflection coefficient, sheet impedance, and surface impedance values are derived from one another, so that knowing one is equivalent to knowing the others. Assuming no higher-order modes are radiated and the vias and the medium are lossless, it can be concluded that the magnitude of the reflection coefficient of the via array is unity and therefore the corresponding sheet and the surface impedance values are pure imaginary numbers. Therefore the problem reduces to sheet and surface reactances. In this chapter, the sheet reactances are calculated looking from the inside and the outside of the via array with varying number of vias, and they are compared. This is repeated for the dielectric case where the medium has a dielectric constant different than 1. Also, the sheet reactance behavior with frequency is investigated. Finally, the variation of the sheet reactance values with varying radius of the vias and radius of the via array are presented.

At the end of the chapter an approximate CAD formula for finding the equivalent reactance of the via array, which neglects mutual coupling, is introduced and the numerical results are compared with those from the analytical formula.

4.2 Cylinder Code and Strip Code Comparison for Validation

In Chapter 2, the electromagnetic analysis of a circular array of vias was developed for both the cylindrical via and the equivalent flat strip via model. In this chapter various via-array structures are investigated using the aforementioned two different analysis methods, and the results are compared in order to validate the cylindrical via model.

The formulas found from both analysis methods in Chapter 2 were programmed in order to calculate the reflection coefficients of the via-array structures. In the cylinder model analysis part, a basis-function representation of the surface currents is assumed, with unknown current coefficients a_n for each via. Then using the Electric Field Integral Equation (EFIE), which uses boundary conditions and testing functions, the unknown a_n coefficients are determined by solving the matrix equation. Knowing the currents on the vias, the scattered field is calculated, and from this the reflection coefficient.

A similar EFIE procedure is used to find the unknown currents on each strip in the flat strip model of the via array. Then the scattered field from the array is found using a

Fourier series representation of the current on the array. Reflection coefficients are then found by using this method.

Finally, different array geometries are chosen and the corresponding reflection coefficients are calculated using both methods and are compared. The behavior of the reflection coefficients is also investigated by changing the number of vias, the via-array radius, and the radius of the vias.

4.2.1 Reflection Coefficient Results: Varying Number of Vias in an Air Medium

For this study, the via-array geometry is chosen to have the same dimensions as the SAR-RSW antenna discussed in Chapter 1, in order to have results for a case that is close to practical dimensions. The number of vias is varied from 4 to 32, to see the effect of the number of vias on the value of the reflection coefficient. Table 4.1 shows the chosen dimensions of the array with varying number of via elements.

The exterior reflection coefficient results found from the cylinder model and strip model are compared in Table 4.2. As can be seen from Table 4.2, the reflection coefficient values calculated from the two different methods show very good agreement. The magnitudes of the reflection coefficients are unity, showing that only waves with the same azimuth variation as the incoming wave are significantly scattered from the array. That is, higher-order modes are not significantly generated.

Table 4.1. The via-array parameters used to find reflection coefficients for an air medium, with a varying number of vias in the array.

Definition of the Variable	**Symbol**	**Value**
Radius of the via elements	a	0.3175 mm
Radius of the via array	R_0	30.29 mm
Number of current basis functions	$2N+1$	25
Frequency	f	1.575 GHz
Mode number of the incoming wave	n_i	1
Number of via elements	L	varying
Permittivity of the medium	ε_r	1

Table 4.2. A comparison of exterior reflection coefficients calculated using the cylinder model and the strip model. The via-array parameters are given in Table 4.1.

Γ_{EXT}	***REFLECTION COEFFICIENTS USING CYLINDER MODEL***		***REFLECTION COEFFICIENTS USING STRIP MODEL***	
NUMBER of VIAS	**MAGNITUDE**	**PHASE (degrees)**	**MAGNITUDE**	**PHASE (degrees)**
L=4	1.000	146.312	1.000	146.727
L=8	1.000	160.464	1.000	160.906
L=16	1.000	171.239	1.000	171.361
L=32	1.000	177.047	1.000	177.063
L=64	1.000	179.460	1.000	179.382

The phase of the reflection coefficient gets closer to 180° as the number of vias is increased, meaning the via array acts as a short-circuit wall at $\rho = R_0$ when the number of vias is large enough.

4.2.2 Reflection Coefficient Results: Varying Number of Vias in a Dielectric Medium

To investigate the effect of the dielectric medium around the via array on the reflection coefficient, the via array geometry given in Table 4.3 in a medium with a dielectric constant of $\varepsilon_r = 2.94$ is analyzed. The results for the exterior reflection coefficients found from the cylinder and strip models in a dielectric medium are given in Table 4.4. The first thing observed is the consistency of the results found from the two different methods. Also, as can be seen from comparing this table with the results from the air case given in Table 4.2, the phases of the refection coefficients in the dielectric case, for the same number of vias, are less than those of the via array in air, which means the array acts less like a short circuit wall in the dielectric. This is not too surprising, since the surrounding medium is modeled as a transmission line with a lower characteristic impedance with there is a dielectric present. Also, the magnitude of the reflection coefficient is not unity for a small number of vias, (e.g. 4 vias), which is explained by the excitation of higher-order modes that are not included in the reflection coefficient definition.

Table 4.3. The via-array parameters used to find the reflection coefficients for a dielectric medium, with a varying number of vias in the array.

Definition of the Variable	**Symbol**	**Value**
Radius of the via elements	a	0.3175 mm
Radius of the via array	R_0	30.29 mm
Number of current basis functions	$2N+1$	25
Frequency	f	1.575 GHz
Mode number of the incoming wave	n_i	1
Number of via elements	L	varying
The permittivity of the medium	ε_r	2.94

Table 4.4. Comparison of exterior reflection coefficient results for a dielectric medium, calculated using the cylinder model and the strip model. The via-array parameters are given in Table 4.3.

Γ_{EXT}	***REFLECTION COEFFICIENTS USING CYLINDER MODEL***		***REFLECTION COEFFICIENTS USING STRIP MODEL***	
NUMBER of VIAS	**MAGNITUDE**	**PHASE (degrees)**	**MAGNITUDE**	**PHASE (degrees)**
L=4	0.991	101.300	0.991	101.723
L=8	1.000	136.690	1.000	137.163
L=16	1.000	161.783	1.000	162.013
L=32	1.000	174.197	1.000	174.137
L=64	1.000	179.157	1.000	178.784

4.2.3 Reflection Coefficient Results: Varying Via Radius

The via radius is an important parameter from a manufacturing point of view; therefore the effect of changing the via radius is investigated for a 32 element via array. The array parameters are given in Table 4.5 and comparative results from the two different models are given in Table 4.6.

Table 4.5. The via-array parameters used to find the exterior reflection coefficients for varying via radius.

Definition of the Variable	**Symbol**	**Value**
Radius of the via elements	a	varying
Radius of the via array	R_0	30.29 mm
Number of current basis functions	$2N+1$	25
Frequency	f	1.575 GHz
Mode number of the incoming wave	n_i	1
Number of via elements	L	64
The permittivity of the medium	ε_r	1

The results in Table 4.6 show that the reflection coefficients calculated from the two different methods agree well. The reflection coefficient values approach -1 (i.e. a short-circuit wall) as the via radius increases, as expected. However, the sensitivity of the reflection coefficient with changing via radius is not very large.

Table 4.6. Comparison of exterior reflection coefficients calculated using the cylinder model and the strip model for varying via radius. The via-array parameters are given in Table 4.5.

Γ_{EXT}	***REFLECTION COEFFICIENTS USING CYLINDER MODEL***		***REFLECTION COEFFICIENTS USING STRIP MODEL***	
VIA RADIUS [mm]	**MAGNITUDE**	**PHASE (degrees)**	**MAGNITUDE**	**PHASE (degrees)**
0.03969	1	176.672	1	178.861
0.07938	1	177.567	1	178.877
0.15875	1	178.494	1	178.960
0.31750	1	179.460	1	179.382
0.63500	1	180.540	1	179.997

4.2.4 Reflection Coefficient Values: Varying Array Radius

To understand the effect of the radius of the via array on the reflection coefficient, the number of vias and the radius of each via are kept constant while the radius of the array is varied. The via-array radius is very important for certain microstrip antennas, such as the SAR-RSW antenna, in which the resonance frequency depends on the via-array radius. The geometrical parameters are given in Table 4.7 and the results are given in Table 4.8. It is seen that for a fixed number of vias, the via array behaves more as a short-circuit wall as the radius of the via array decreases.

Table 4.7. The via-array parameters used to find the reflection coefficients for varying via-array radius.

Definition of the Variable	**Symbol**	**Value**
Radius of the via elements	a	0.3175 mm
Radius of the via array	R_0	varying
Number of current basis functions	$2N+1$	25
Frequency	f	1.575 GHz
Mode number of the incoming wave	n_i	1
Number of via elements	L	32
The permittivity of the medium	ε_r	1

Table 4.8. Comparison of exterior reflection coefficient values calculated using the cylinder model and the strip model for varying via-array radius. The via-array parameters are given in Table 4.7.

Γ_{EXT}	***REFLECTION COEFFICIENTS USING CYLINDER MODEL***		***REFLECTION COEFFICIENTS USING STRIP MODEL***	
ARRAY RADIUS [mm]	**MAGNITUDE**	**PHASE (degrees)**	**MAGNITUDE**	**PHASE (degrees)**
8.0070	1	180.069	1	179.993
16.0140	1	179.483	1	179.450
32.0279	1	177.047	1	177.063
64.0558	1	167.201	1	169.67
128.1116	1	159.363	1	165.391

4.3 Reflection Coefficient Convergence Results: Varying Number of Basis Functions

The current distribution on the reference (number zero) via is represented by a finite summation of current basis functions as

$$J_{sz}^{(0)}(\rho,\phi)=\sum_{n=-N}^{n=N} a_n\, e^{jn\phi_l'} \quad . \tag{4.1}$$

It is clear that the number of elements in the summation cannot be very large due to the computer memory constraints and the processing time limitations, but at the same time this number should be large enough for results to converge to a solution. Therefore the via-nalysis program is run to find the reflection coefficients for different geometries in order to investigate the effect of the number of basis functions used in describing the unknown current. Since the summation runs from –N to +N, the total number of basis functions will be 2N+1.

First, a via-array geometry with a fairly large number of vias is chosen as indicated in Table 4.9, under the assumption that convergence will be more difficult to achieve for a large number of vias. The results for the exterior reflection coefficient values, with the number of basis functions changing from 1 to 11, are shown in Table 4.10. From these results it can be concluded that three or five current basis functions are enough to calculate the reflection coefficient for this specific array with the dimensions in Table 4.9.

Table 4.9. The via-array parameters to find exterior reflection coefficients with varying number of current basis functions.

Definition of the Variable	Symbol	Value
Radius of the via elements	a	0.3175
Radius of the via array	R_0	30.29 mm
Number of current basis functions	$2N+1$	varying
Frequency	f	1.575 GHz
Mode number of the incoming wave	n_i	1
Number of via elements	L	64
The permittivity of the medium	ε_r	1

Table 4.10. Comparison of exterior reflection coefficients calculated from the cylinder model for varying number of current basis functions. The via-array parameters are given in Table 4.9.

Γ_{EXT}	***REFLECTION COEFFICIENTS USING CYLINDER MODEL***	
NUMBER of BASIS FUNCTIONS (2*N*+1)	**MAGNITUDE**	**PHASE (degrees)**
1	1.000	179.43843
3	0.999	179.45891
5	0.999	179.45975
7	0.999	179.45975
9	0.999	179.45975
11	0.999	179.45975

4.4 Cavity Model and HFSS Cavity Simulations for Validation

To further investigate the validity of the analytical circular via-array model, cavity resonators are analyzed using the via-array model and the electromagnetic simulation tool HFSS. Two types of cavities are created. One is a PMC wall cavity (PEC on top and bottom and PMC side walls) and the other is PEC wall cavity (PEC on top, bottom and side walls). Both of the cavities have an array of vias inside them with a specific geometry. These cavities are first solved analytically using the analytical sheet reactance model for the via array, and then they are simulated in Ansoft HFSS using the actual via array. Values for the resonance frequency of the via-array loaded PMC and PEC cavities from both methods are compared. The resonance frequency comparison is intended to give an idea of accuracy in the analytical modeling of via array as a sheet impedance wall. Even though this section is only for verification of the analytical results, practical dimensions such as those for a SAR-RSW antenna and a UHF antenna are used.

4.4.1 Analytical Model for PMC Wall Cavity

The via array in a PMC wall cavity (PEC top and bottom and PMC side walls) and its equivalent surface impedance model are shown in Figure 4.1. The equivalent surface impedance of the via array is found from the corresponding reflection coefficient result, using the analysis discussed in Chapter 2. The resonance frequencies of the cavity shown in Figure 4.1(b) are found by following standard cavity field analysis.

The field in the region $R_0 < \rho < R_1$ of Figure 4.1(b) is

$$E_z(\rho,\phi) = e^{jn_i\phi}\left(H_{n_i}^{(1)}(k\rho) + CH_{n_i}^{(2)}(k\rho)\right). \tag{4.2}$$

The reflection coefficient looking towards the via array from the exterior is written as

$$\Gamma_{EXT} = \frac{CH_{n_i}^{(2)}(kR_0)}{H_{n_i}^{(1)}(kR_0)}. \tag{4.3}$$

The reflection coefficient given in (4.3) is the same as the reflection coefficient result of the corresponding via array discussed in Chapter 2. Therefore, the numerical result for the reflection coefficient in (4.3) is calculated using the via analysis.

Using the boundary condition at the PMC wall at R_1 with (4.2) and (4.3) results in the following transcendental equation,

$$\Gamma_{EXT} = -\frac{H_{n_i}^{(1)\prime}(kR_1)}{H_{n_i}^{(2)\prime}(kR_1)}\frac{H_{n_i}^{(2)}(kR_0)}{H_{n_i}^{(1)}(kR_0)}, \tag{4.4}$$

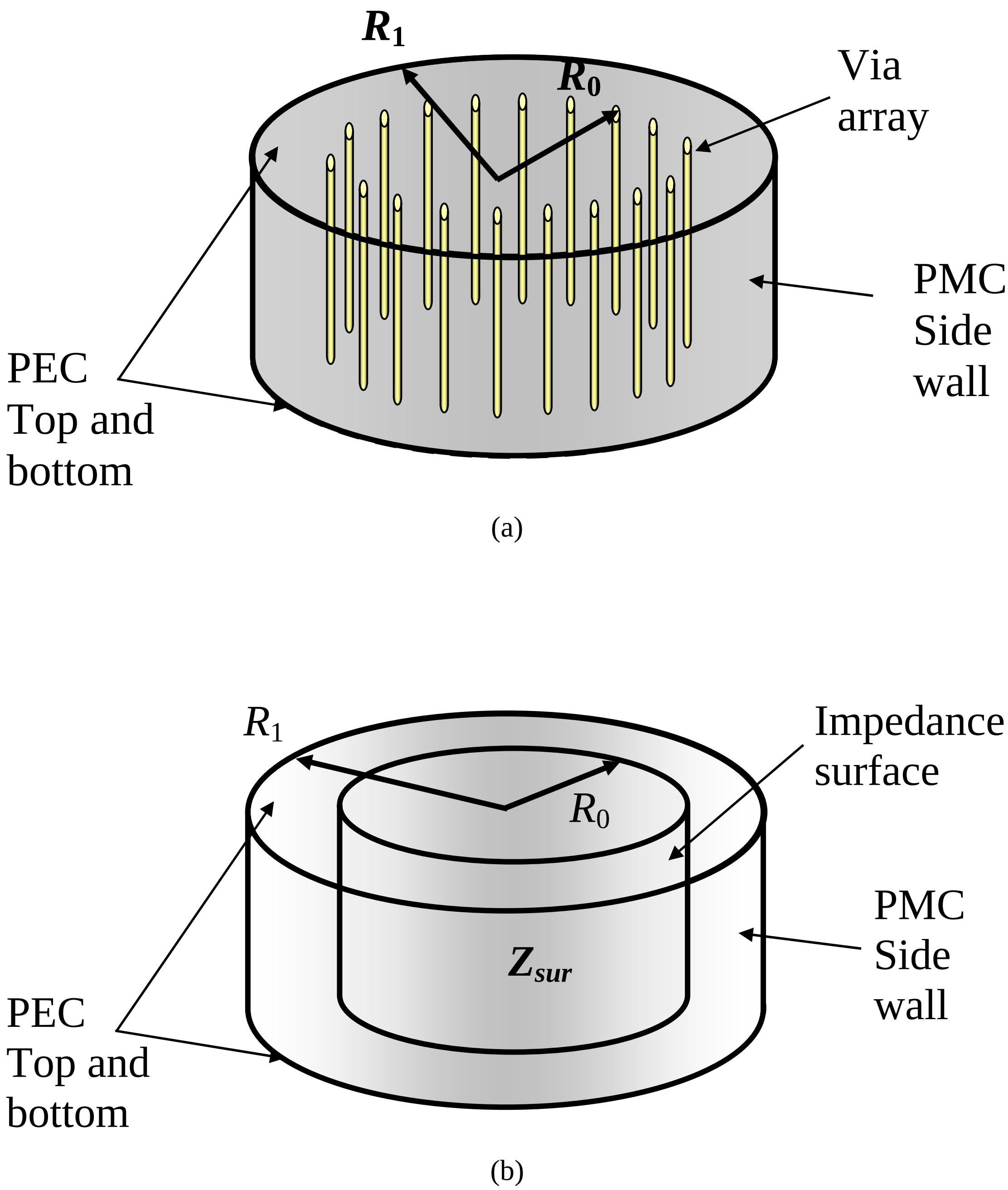

Figure 4.1. (a) PMC cavity with an array of vias. (b) PMC cavity model with an equivalent surface impedance for the via array.

which is solved for k to find the resonance frequency. Equation (4.4) is expressed in terms of surface impedance by using (2.94) in (4.4). It is noted that Γ_{EXT} in (4.4) is frequency dependent, therefore to find the resonance frequency (4.4) and the reflection coefficient should be solved for iteratively as shown in Figure 4.2.

4.4.2 Analytical Model for PEC Wall Cavity

Similarly, the via array in a PEC wall cavity (PEC top, bottom and side wall) and its equivalent surface impedance model are shown in Figure 4.3. The equivalent surface impedance of the via array can be found from its corresponding reflection coefficient obtained using the analysis discussed in Chapter 2. The resonance frequencies of the cavity shown in Figure 4.3(b) can be found by following standard cavity field analysis.

The field in the $R_0 < \rho < R_1$ region of Figure 4.3(b) is

$$E_z\left(\rho,\phi\right) = e^{jn_i\phi}\left(H_{n_i}^{(1)}\left(k\rho\right) + CH_{n_i}^{(2)}\left(k\rho\right)\right). \tag{4.5}$$

The reflection coefficient looking towards the via array from the exterior is written as

$$\Gamma_{EXT} = \frac{CH_{n_i}^{(2)}\left(kR_0\right)}{H_{n_i}^{(1)}\left(kR_0\right)}. \tag{4.6}$$

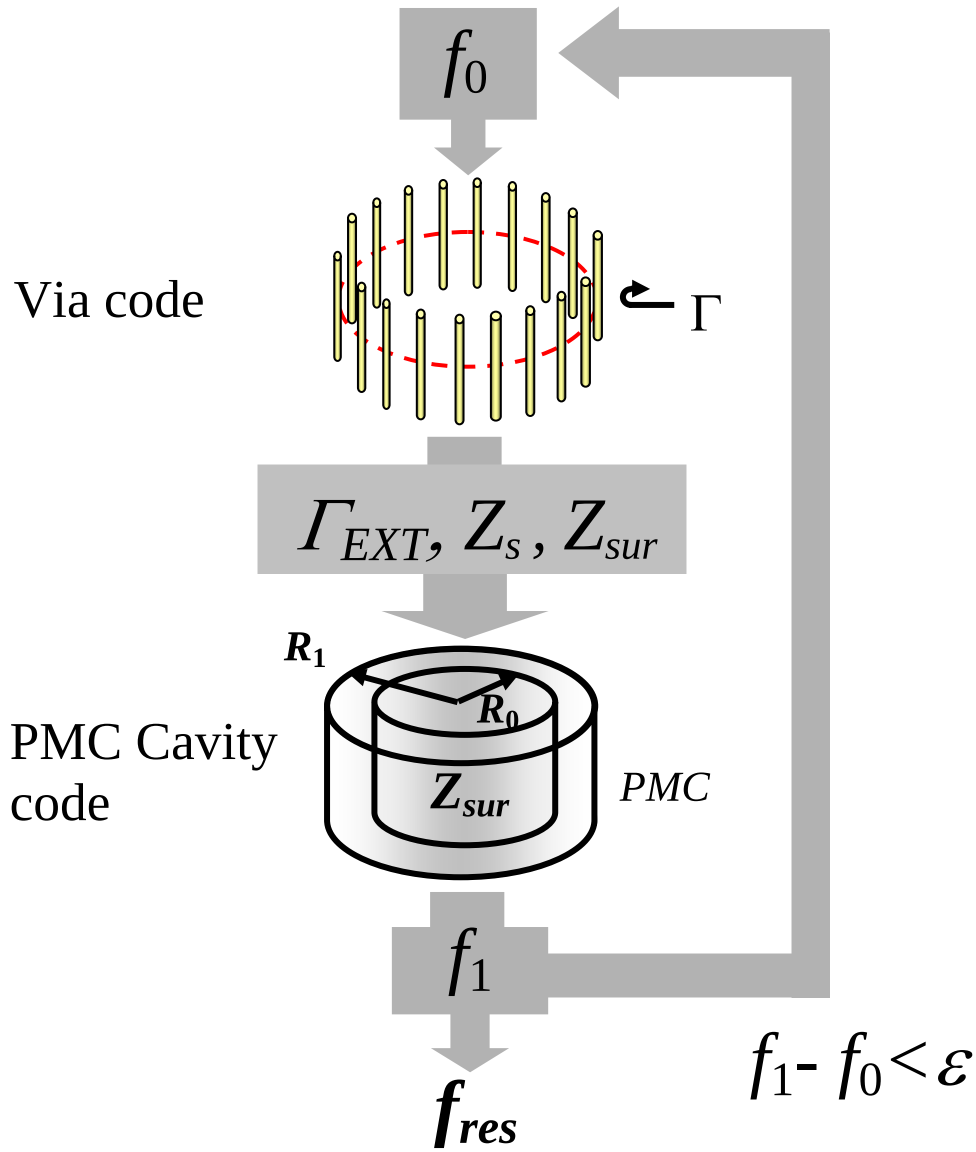

Figure 4.2. Iterative process scheme for a PMC cavity, showing how to find the resonance frequency of the via-array loaded cavity analytically.

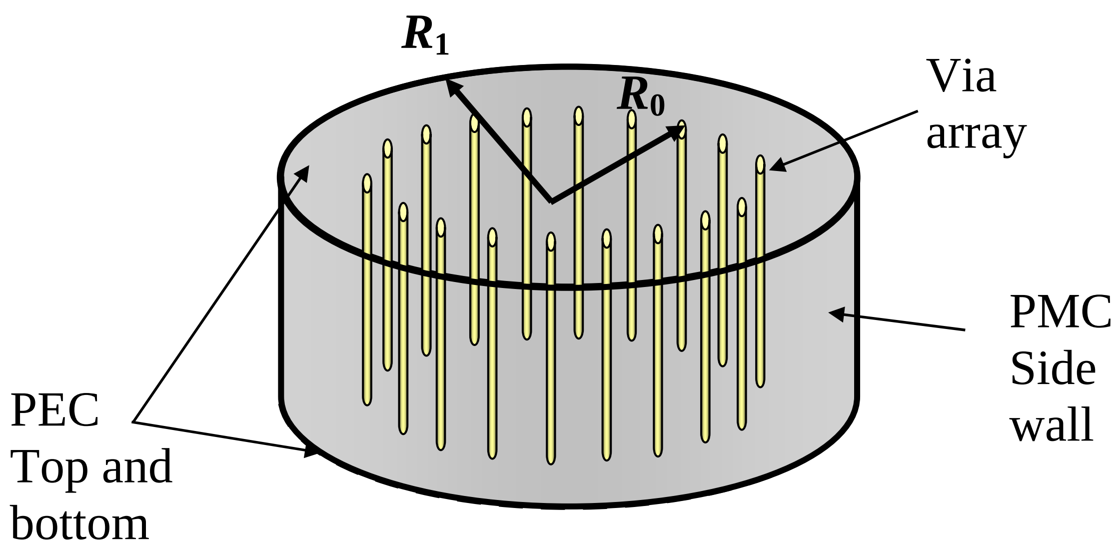

(a)

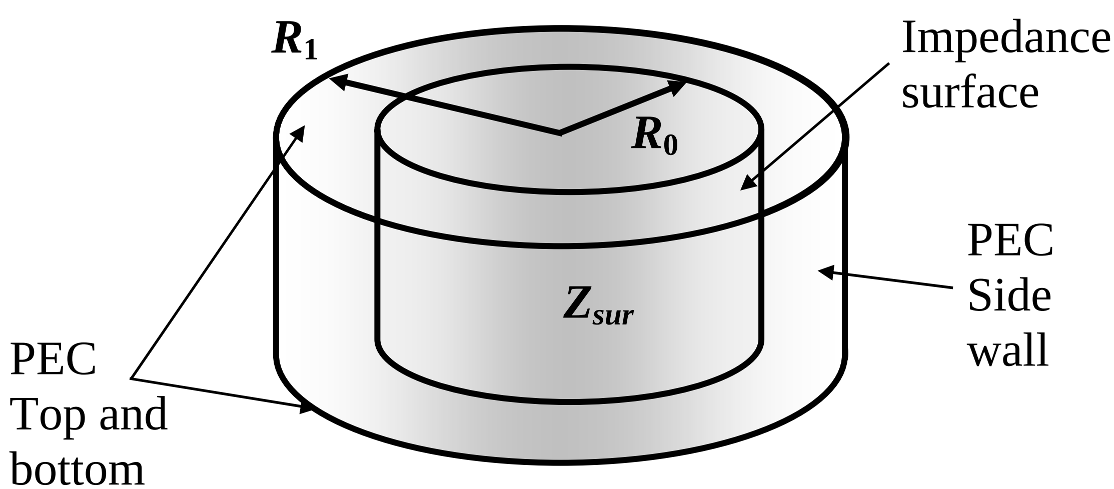

(b)

Figure 4.3. (a) PEC cavity with an array of vias. (b) PEC cavity model with an equivalent surface impedance model for the via array.

The exterior reflection coefficient given in (4.6) is the same as the reflection coefficient found for the corresponding via array discussed in Chapter 2. Therefore the numerical result for the reflection coefficient in (4.6) is calculated using the via analysis.

Using the boundary condition at the PEC wall at R_1 with (4.5) and (4.6) results in the following transcendental equation:

$$\Gamma_{EXT} = -\frac{H_{n_i}^{(1)}\left(kR_1\right)}{H_{n_i}^{(2)}\left(kR_1\right)}\frac{H_{n_i}^{(2)}\left(kR_0\right)}{H_{n_i}^{(1)}\left(kR_0\right)}, \tag{4.7}$$

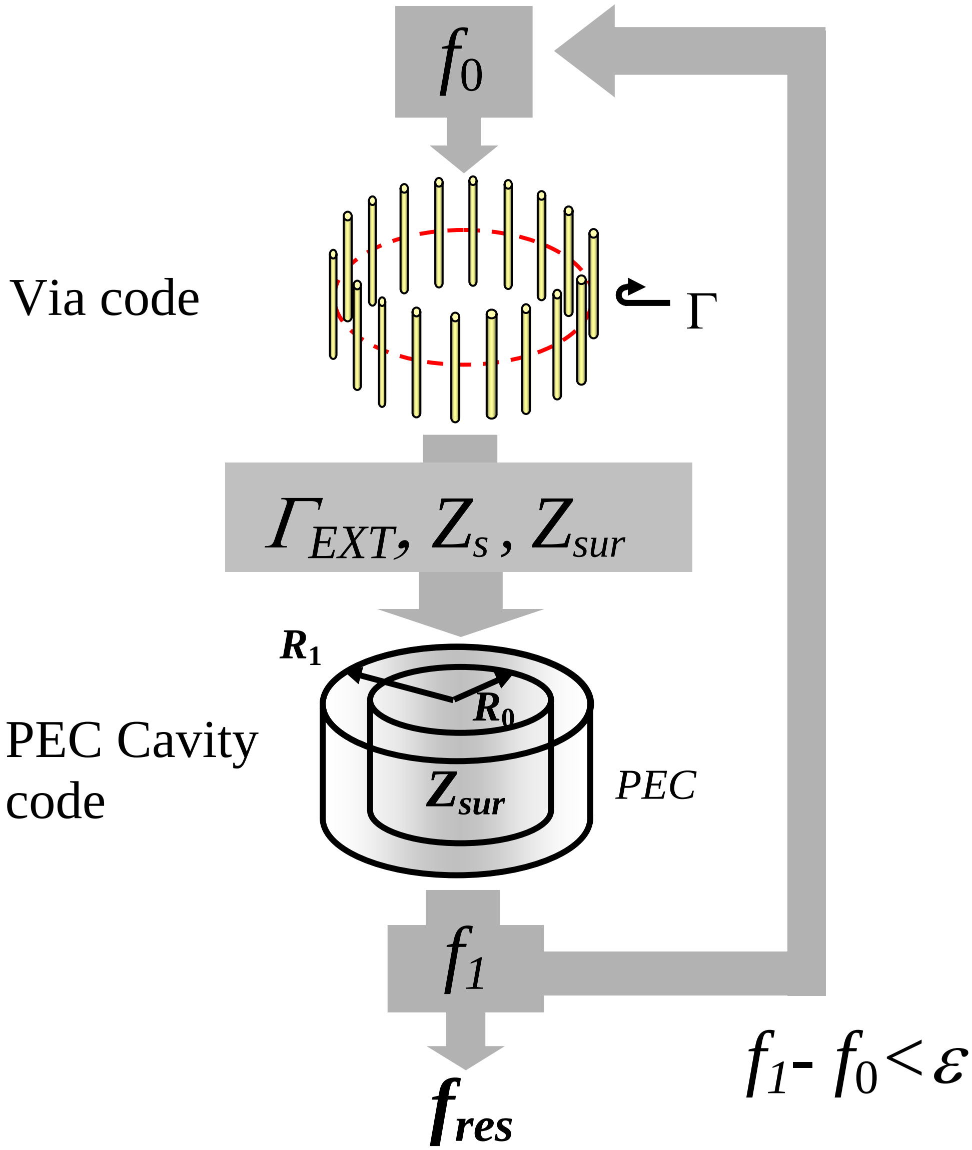

Figure 4.4. Iterative process scheme used to find the resonance frequency of the via-array loaded PEC cavity.

4.4.3 Results for PMC Wall Cavity

The via-loaded PMC cavity, with the parameters listed in Table 4.11, is simulated in Ansoft HFSS to obtain its resonance frequencies. In particular, a cylinder created with the given parameters in HFSS and the corresponding PEC and PMC boundaries is analyzed using the eigenvalue solver feature of HFSS is used to find the resonance frequencies.

Table 4.11. The PMC cavity with the via-array parameters used in the analysis to find the resonance frequencies and surface impedances.

Definition of the Variable	**Symbol**	**Value**
Radius of the via elements	a	0.205 cm
Radius of the via array	R_0	17.7579 cm
Radius of the cavity	R_1	21.3950 cm
Mode number of the incoming wave	n_i	0, 1
Number of via elements	L	9
The permittivity of the medium	ε_r	1

The same cavity given in Table 4.11, with the corresponding equivalent via-array surface impedance, is then analyzed using the iterative procedure shown in Figure 4.4. The results for the resonance frequencies, found from HFSS and the iterative procedure using the analytical formulation, are compared in Table 4.12.

The surface impedance values are also compared in Table 4.13. The corresponding surface impedance value for the HFSS solution is determined by finding the surface impedance value which gives the HFSS resonance frequency in the analytical cavity model. It should be also noted that the surface approximation used in HFSS to approximate the cylinder is 3 degrees and the maximum element length used for meshing in HFSS is 1 cm.

Table 4.12. Comparison of resonance frequencies found from the analytical via-array and PMC cavity code, and from the Ansoft HFSS eigenvalue solution.

f_0	***RESONANCE FREQUENCIES OF THE PMC CAVITY***	
MODE NUMBER	**ITERATIVE ANALYTICAL VIA ARRAY AND CAVITY CODE**	**ANSOFT HFSS EIGENVALUE SOLUTION**
n_i=0	486.55 MHz	485 GHz
n_i=1	743 GHz	738 GHz

Table 4.13 Comparison of surface reactances found from the analytical via array and PMC cavity code, and from the corresponding Ansoft HFSS eigenvalue solution.

Z_{sur}	***EQUIVALENT SURFACE REACTANCES OF THE VIA ARRAY IN THE PEC CAVITY***	
MODE NUMBER	**ITERATIVE ANALYTICAL VIA ARRAY AND CAVITY CODE**	**USING THE FREQUENCY FROM ANSOFT HFSS EIGENVALUE SOLUTION**
n_i=0	96.177 ohms/square	95.02 ohms/square
n_i=1	142.162 ohms/square	141.63 ohms/square

Another via-array loaded PMC cavity as shown in Figure 4.5, with the parameters given in Table 4.14, is simulated in Ansoft HFSS to obtain its resonance frequencies. Once again, a cylinder created with the given parameters in HFSS and the corresponding PEC and PMC boundaries is used along with the eigenvalue solver feature of the HFSS is used to find the resonance frequencies.

Table 4.14. The PMC cavity with the via-array parameters used to find the resonance frequencies and surface impedances.

Definition of the Variable	Symbol	Value
Radius of the via elements	a	0.03175 cm
Radius of the via array	R_0	3.029 cm
Radius of the cavity	R_1	5.577 cm
Mode number of the incoming wave	n_i	0, 1
Number of via elements	L	32
The permittivity of the medium	ε_r	2.94

The same cavity given in Table 4.14, with the corresponding equivalent via-array surface impedance, is analyzed using the iterative procedure shown in Figure 4.4. The results for resonance frequencies, found from HFSS and the iterative procedure using the analytical formulation, are compared in Table 4.15.

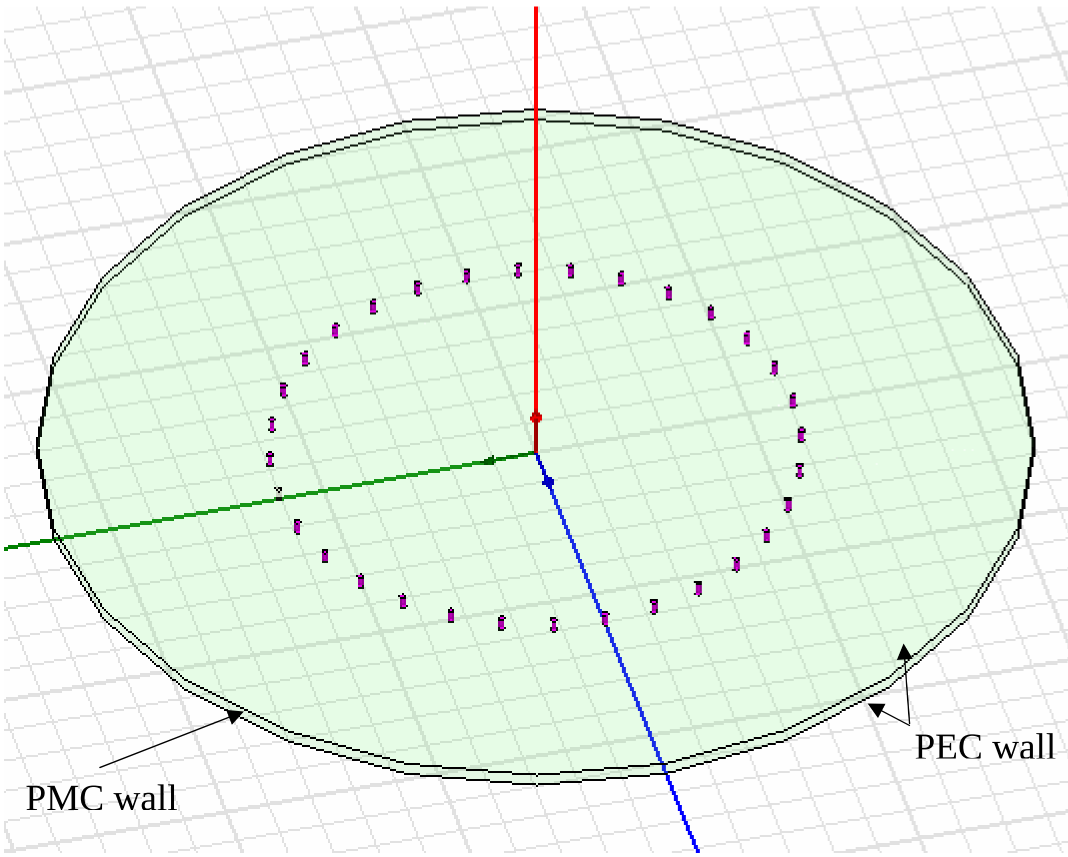

Figure 4.5. PMC cavity with an array of vias used in HFSS simulations with the parameters given in Table 4.14.

Table 4.15. Comparison of resonance frequencies found from the analytical via array and PMC cavity code, and from the Ansoft HFSS eigenvalue solution.

f_0	***RESONANCE FREQUENCIES OF THE PEC CAVITY***	
MODE NUMBER	**ITERATIVE ANALYTICAL VIA ARRAY AND CAVITY CODE**	**ANSOFT HFSS EIGENVALUES SOLUTION**
n_i=0	1.4400 GHz	1.4408 GHz
n_i=1	1.5620 GHz	1.5613 GHz

The surface impedance values are also compared in Table 4.16. The corresponding surface impedance values from the HFSS solution are determined by finding the surface impedance value which gives the HFSS resonance frequency in the analytical cavity model. It should be also noted that the surface approximation used in HFSS to approximate the cylinder is 3 degrees and the maximum element length used for meshing in HFSS is 1 cm.

Table 4.16. Comparison of surface impedances found from the analytical via array and PMC cavity code, and from the corresponding Ansoft HFSS eigenvalue solution.

Z_{sur}	***EQUIVALENT SURFACE REACTANCES OF THE VIA ARRAY IN THE PEC CAVITY***	
MODE NUMBER	**ITERATIVE ANALYTICAL VIA ARRAY AND CAVITY CODE**	**USING THE FREQUENCY FROM ANSOFT HFSS EIGENVALUES SOLUTION**
n_i=0	12.622 ohms/square	12.631 ohms/square
n_i=1	12.452 ohms/square	12.091 ohms/square

4.4.4 Results for PEC Wall Cavity

PEC cavities are next simulated in Ansoft HFSS to obtain the resonance frequencies of the structures as shown in Figure 4.6. The parameters for the first cavity are given in Table 4.17.

Table 4.17. The PEC cavity with via-array parameters used to find the resonance frequencies and surface impedances.

Definition of the Variable	**Symbol**	**Value**
Radius of the via elements	a	0.205 cm
Radius of the via array	R_0	17.7579 mm
Radius of the cavity	R_1	21.3950 mm
Mode number of the incoming wave	n_i	0, 1
Number of via elements	L	9
The permittivity of the medium	ε_r	1

This cavity is analyzed using a similar iterative procedure shown in Figure 4.4 and the results for resonance frequency are shown in Table 4.18.

Table 4.18. Comparison of resonance frequencies found from the analytical via array and PEC cavity code, and from the Ansoft HFSS eigenvalue solution.

f_0	***RESONANCE FREQUENCIES OF THE PEC CAVITY***	
MODE NUMBER	**ITERATIVE ANALYTICAL VIA ARRAY AND CAVITY CODE**	**ANSOFT HFSS EIGENVALUE SOLUTION**
n_i=0	579.7 MHz	580.1 MHz
n_i=1	919.9 MHz	920.9 MHz

The surface impedance values are also compared in Table 4.19. The surface impedance value for the HFSS simulation is determined by finding the surface impedance value which gives the HFSS resonance frequency in the analytical cavity model. It should also be noted that the surface approximation to model the cylinder used in HFSS is 3 degrees and the maximum meshing length is 1 cm.

Another geometry similar to a SAR-RSW antenna is also simulated using the same steps.
Table 4.20 shows the geometry and Table 4.21 and Table 4.22 show comparisons of the resonance frequencies and surface impedances, respectively. This time, the element length based refinement is chosen to be 0.5 cm.

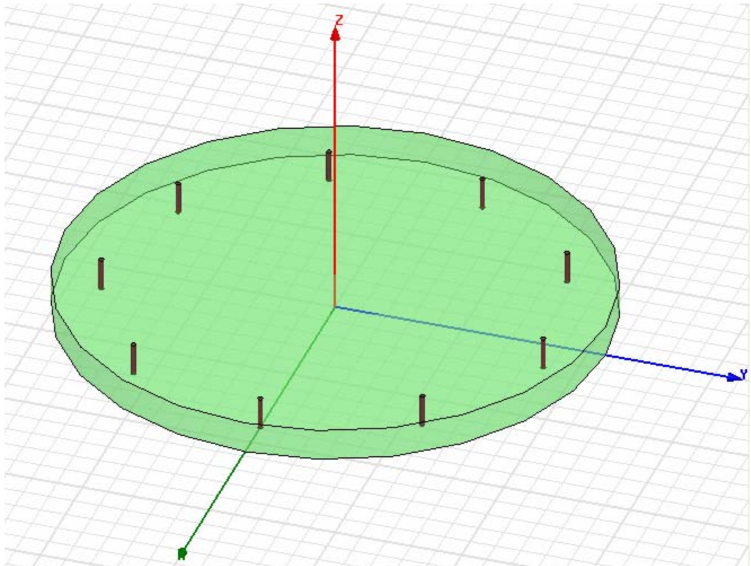

(a)

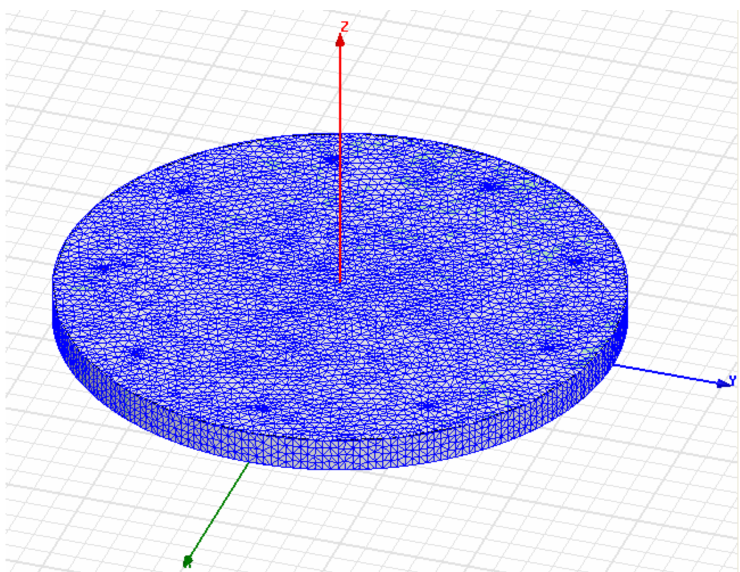

(b)

Figure 4.6. HFSS simulation of an air filled PEC cavity of height of 2.54 cm and radius of 21.395 cm, with an array of 9 via elements at 17.75785 cm radius with a via radius of 0.205 cm. (a) The geometrical model in HFSS, (b) The meshing used to find the fields. The meshing is denser around the vias.

Table 4.19. Comparison of exterior surface reactances found from the analytical via array and PEC cavity code, and from the corresponding Ansoft HFSS eigenvalue solution.

Z_{sur}	***EQUIVALENT SURFACE REACTANCES OF THE VIA ARRAY IN THE PEC CAVITY***	
MODE NUMBER	**ITERATIVE ANALYTICAL VIA ARRAY AND CAVITY CODE**	**USING THE FREQUENCY FROM ANSOFT HFSS EIGENVALUE SOLUTION**
n_i=0	-160.995 ohms/square	-161.240 ohms/square
n_i=1	-279.998 ohms/square	-280.484 ohms/square

Table 4.20. The PEC cavity with the via array parameters used find the resonance frequencies and surface impedances.

Definition of the Variable	**Symbol**	**Value**
Radius of the via elements	a	0.03175 cm
Radius of the via array	R_0	3.029 cm
Radius of the cavity	R_1	5.577 cm
Mode number of the incoming wave	n_i	0, 1
Number of via elements	L	32
The permittivity of the medium	ε_r	2.94

Table 4.21. Comparison of resonance frequencies found from the analytical via array and PEC cavity code, and from the Ansoft HFSS eigenvalue solution.

f_0	***RESONANCE FREQUENCIES OF THE PEC CAVITY***	
MODE NUMBER	**ITERATIVE ANALYTICAL VIA ARRAY AND CAVITY CODE**	**ANSOFT HFSS EIGENVALUE SOLUTION**
n_i=0	2.1373 GHz	2.1362 GHz
n_i=1	3.2623 GHz	3.2620 GHz

Table 4.22. Comparison of exterior surface reactances found from the analytical via array and PEC cavity code, and from the corresponding Ansoft HFSS eigenvalue solution.

X_{sur}	***EQUIVALENT SURFACE REACTANCES OF THE VIA ARRAY IN THE PEC CAVITY***	
MODE NUMBER	**ITERATIVE ANALYTICAL VIA ARRAY AND CAVITY CODE**	**USING THE FREQUENCY FROM ANSOFT HFSS EIGENVALUE SOLUTION**
n_i=0	17.736 ohms/square	17.738 ohms/square
n_i=1	27.186 ohms/square	27.182 ohms/square

4.5 Sheet and Surface Reactance Results

4.5.1 Exterior Sheet Impedance and Exterior Surface Impedance Results: Varying Number of Vias in an Air Medium

Using the formulas in Sections 2.4 and 2.5, the values of the reflection coefficients are converted into sheet impedance and surface impedance values. The array geometry given in Table 4.1 is used again with a varying number of via elements to find the corresponding sheet and surface impedance values, and the results are shown in Table 4.23.

Table 4.23 shows that impedance values are not pure imaginary – in other words not purely reactive, as one might expect. The reason is that is the higher-order modes being radiated are not taken into account when calculating the reflection coefficients used to obtain the sheet and surface impedances discussed in Sections 2.4 and 2.5. Another important observation from Table 4.23 is that the sheet and surface impedance values approach zero (short circuit) as the number of vias is increased.

Table 4.23. Comparison of sheet and surface impedances calculated using the cylinder model and the strip model. The via-array parameters are given in Table 4.1.

NUMBER of VIAS	***SHEET IMPEDANCES*** **(ohms/square)**	***SURFACE IMPEDANCES*** **(ohms/square)**
L=4	0.317 + j 312.288	0.122 + j 193.612
L=8	0.094 + j 118.149	0.062 + j 95.908
L=16	0.117 + j 42.232	0.100 + j 38.999
L=32	0.177 + j 12.866	0.168 + j 12.549
L=64	0.304 + j 2.262	0.301 + j 2.252

4.5.2 Exterior Sheet Impedance and Exterior Surface Impedance Results: Varying Number of Vias in a Dielectric Medium

Similar to Section 4.5.1, the array geometry given in Table 4.3 is used in a dielectric medium of permittivity 2.94 with a varying number of via elements to find the corresponding sheet and surface impedance values, and the results are shown in Table 4.24.

Similarly, Table 4.24 shows that the impedance values are not pure imaginary and also that the sheet and surface impedance values approach zero (short circuit) as the number of vias is increased.

Table 4.24. Comparison of sheet and surface impedances in a dielectric medium of permittivity 2.94, calculated using the cylinder model and the strip model. The via-array parameters are given in Table 4.3.

NUMBER of VIAS	*SHEET IMPEDANCES* (ohms/square)	*SURFACE IMPEDANCES* (ohms/square)
L=4	4.599 + j 327.166	3.574 + j 288.431
L=8	0.091 + j 119.042	0.083 + j 113.495
L=16	0.087 + j 42.196	0.084 + j 41.477
L=32	0.098 + j 12.624	0.097 + j 12.559
L=64	0.133 + j 1.792	0.133 + j 1.791

4.5.3 Exterior Sheet Impedance and Exterior Surface Impedance Results: Varying Radius of Vias in an Air Medium

The array geometry given in Table 4.5 is used in a dielectric medium of permittivity 2.94 with a varying number of via elements to find the corresponding sheet and surface impedance values and the results are shown in Table 4.25.

Table 4.25 shows that impedance values are not pure imaginary and also the sheet and surface impedance values approach zero (short circuit) as the radius of the vias is increased.

Table 4.25. Comparison of sheet and surface impedances in an air medium, calculated using the cylinder model. The via-array parameters are given in Table 4.5.

VIA RADIUS (mm)	***SHEET IMPEDANCES* (ohms/square)**	***SURFACE IMPEDANCES* (ohms/square)**
0.03969	0.003 + j 37.357	0.002 + j 36.793
0.07938	0.012 + j 29.198	0.012 + j 28.852
0.15875	0.047 + j 21.038	0.046 + j 20.858
0.31750	0.177 + j 12.865	0.175 + j 12.797
0.63500	0.642 + j 4.619	0.64 + j 4.61

4.5.4 Exterior Sheet Impedance and Exterior Surface Impedance Results: Varying Radius of the Via Array in an Air Medium

The array geometry given in Table 4.7 is used in a dielectric medium of permittivity 2.94 with a varying number of via elements to find the corresponding sheet and surface impedance values, and the results are shown in Table 4.26.

Table 4.26 shows that impedance values are not pure imaginary and also the sheet and surface impedance values approach zero (short circuit) as the radius of the via array is decreased.

Table 4.26. Comparison of sheet and surface impedances in an air medium, calculated using the cylinder model. The via-array parameters are given in Table 4.7.

VIA ARRAY RADIUS (mm)	***SHEET IMPEDANCES*** **(ohms/square)**	***SURFACE IMPEDANCES*** **(ohms/square)**
8.0070	0.060 + j 0.611	0.004 + j 0.0002
16.0140	0.127 + j 2.946	0.124 + j 2.912
32.0279	0.175 + j 14.284	0.175 + j 14.265
64.0558	0.031 + j 45.786	45.086 - j 1765
128.1116	0.131 + j 126.900	0.012 + j 37.677

4.5.5 Interior Reflection Coefficient and Sheet Impedance Results: Varying Number of Vias

Numerical results are presented for the interior reflection coefficients discussed in Section 2.2.5 and the interior sheet impedances discussed in section 2.6. The geometry for the via array is given in Table 4.27. As can be seen from Table 4.28, the reflection coefficients are different depending on the direction looked to find the reflection coefficient. Looking from the outside, one sees the via fence and the interior air region, but looking from inside one sees the fence and the exterior air region, which is very different from the interior air region. However the interior and exterior sheet impedances are the same because of the fact that the definition of sheet impedance is independent of the region from which it is observed.

Table 4.27. The via-array parameters used to find the interior reflection coefficient and the sheet reactance for a varying number of vias.

Definition of the Variable	**Symbol**	**Value**
Radius of the via elements	a	0.3175 mm
Radius of the via array	R_0	30.29 mm
Number of current basis functions	$2N+1$	25
Frequency	f	1.575 GHz
Mode number of the incoming wave	n_i	1
Number of via elements	L	varying
The permittivity of the medium	ε_r	1

Table 4.28. Comparison of interior and exterior reflection coefficient values and sheet impedance values, calculated from the cylinder model. The via-array parameters are given in Table 4.27.

	REFLECTION COEFFICIENT CYLINDER MODEL (Γ_{EXT})		***REFLECTION COEFFICIENT CYLINDER MODEL*** (Γ_{INT})		***SHEET REACTANCE*** ($X_{sh,EXT}$)	***SHEET REACTANCE*** ($X_{sh,INT}$)
NUMBER of VIAS	**MAGNITUDE**	**PHASE (degrees)**	**MAGNITUDE**	**PHASE (degrees)**	**OHMS/SQ.**	**OHMS/SQ.**
L=4	1.000	146.312	0.606	127.350	312.279	312.248
L=8	1.000	160.464	0.895	153.608	118.147	118.148
L=16	1.000	171.239	0.984	169.930	42.232	42.272
L=32	0.999	177.047	0.999	176.879	12.864	12.975
L=64	0.999	179.460	1.000	179.398	2.263	2.497

4.5.6 Exterior Reflection Coefficient and Exterior Sheet Impedance Results: Varying Frequency

Numerical results are presented in Table 4.30 for the reflection coefficients and sheet impedances when the frequency changes for the specific via-array geometry given in Table 4.29.

Table 4.29. The via-array parameters used to find the reflection coefficients and sheet impedances for varying frequency.

Definition of the Variable	Symbol	Value
Radius of the via elements	a	0.3175 mm
Radius of the via array	R_0	30 mm
Number of current basis functions	$2N+1$	25
Frequency	f	varying
Mode number of the incoming wave	n_i	1
Number of via elements	L	16
The permittivity of the medium	ε_r	1

As can be seen in Table 4.30, the sheet reactance values increase as the frequency increases, which is consistent with the simple impedance and inductance relation, $Z = j(2\pi f)L$. The sheet reactance is not exactly independent of frequency, however, so the relationship between sheet reactance and frequency is not exactly linear.

Table 4.30. Variation of the exterior reflection coefficient and the exterior sheet reactance versus frequency. The via-array parameters are given in Table 4.29.

	REFLECTION COEFFICIENT CYLINDER MODEL **(Γ_{EXT})**		***SHEET REACTANCE*** **($X_{sh,EXT}$)**
FREQUENCY (GHz)	**MAGNITUDE**	**PHASE (degrees)**	**OHMS/SQ.**
1.0	1.000	175.592	26.42
1.2	1.000	174.186	31.71
1.4	1.000	172.718	36.99
1.6	1.000	171.204	42.264
1.8	1.000	169.650	47.536
2.0	0.999	168.060	52.804
2.2	0.999	166.428	58.070
2.4	0.999	164.752	63.338
2.6	0.999	163.020	68.613
2.8	0.999	161.221	73.899
3.0	0.999	159.338	79.203
3.2	0.999	157.348	84.529
3.4	0.999	155.223	89.882
3.6	0.999	152.923	95.265

4.6 Approximate Reactance Formula vs. Exact Results

It is assumed that there is no coupling or negligible coupling between the vias in the array, then an approximate reactance formulation for the single via can be used for the via-array case. The reactance of a single probe is found from the delivered power to a tube model of the single cylindrical via using field analysis as

$$X_{in} = \eta \frac{(kh)}{4} J_0(ka) H_0^{(2)}\left(ka\right) \tag{4.8}$$

or

$$X_{in} \approx \eta \frac{(kh)}{4} \left(\frac{2}{\pi}\right)\left(-\gamma + \ln\left(\frac{2}{ka}\right)\right), \tag{4.9}$$

where η is the wave impedance of the medium, h is the height of the via, and a is the radius. Also, the value of Euler's constant γ is

$$\gamma = 0.5772156. \tag{4.10}$$

The approximate formula for the equivalent via-array sheet reactance is written as

$$X_{sh,array} \approx \frac{2\pi R_0}{hL} X_{in}, \tag{4.11}$$

where L is the number of elements and R_0 is the radius of the via array.

The results in Table 4.32 for the geometry given in Table 4.31 show that the approximate formula is not accurate for obtaining the reactance values due to the coupling between the elements of the array, especially for a larger number of vias. This also proves the necessity for the detailed electromagnetic analysis for this type of via array that has been given here.

Table 4.31. The via-array parameters used in the approximate formula and the exact results for the sheet impedances, for varying number of vias in the array.

Definition of the Variable	**Symbol**	**Value**
Radius of the via elements	a	0.3175 mm
Radius of the via array	R_0	30.29 mm
Number of current basis functions	$2N+1$	25
Frequency	f	1.575 GHz
Mode number of the incoming wave	n_i	1
Number of via elements	L	varying
The permittivity of the medium	ε_r	1

Table 4.32. Comparison of sheet reactance values calculated using the approximate formula and the cylinder model.

X_{sh}	***SHEET REACTANCE VALUES USING APPROXIMATE FORMULA***	***SHEET REACTANCE VALUES USING CYLINDER MODEL***
NUMBER of VIAS	**OHMS/SQ.**	**OHMS/SQ.**
L=4	465.140	312.539
L=8	232.757	118.246
L=16	116.378	42.267
L=32	58.189	12.875
L=64	29.095	2.265

Chapter 5
Practical Antenna Applications of Circular Via Arrays

5.1 SAR-RSW Antenna

5.1.1 Introduction

An important application of the circular via array analyzed in Chapter 2 is its use in the design of Shorted Annular Ring Reduced Surface Wave (SAR-RSW) microstrip antennas. A new design procedure is developed for designing a practical SAR-RSW antenna using the via analysis, starting from a desired resonance frequency for the antenna.

The SAR-RSW shown in Figure 5.1 consists of an annular ring antenna with a short-circuit boundary introduced by a circular array of vias at radius R_0. The outer radius R_1 is found using the RSW condition and the inner radius R_1 is found by making the antenna resonant at the desired frequency.

The main difference between the previous and the new RSW design procedure is the use of a reactive wall instead of short circuit wall at the inner boundary R_0 to obtain a resonance. The reactance of the wall necessary for the resonance is found using a cavity model analysis. Then the reactive wall is realized using an array of vias. The number of vias and their radius are found with the help of the via analysis discussed in Chapter 2.

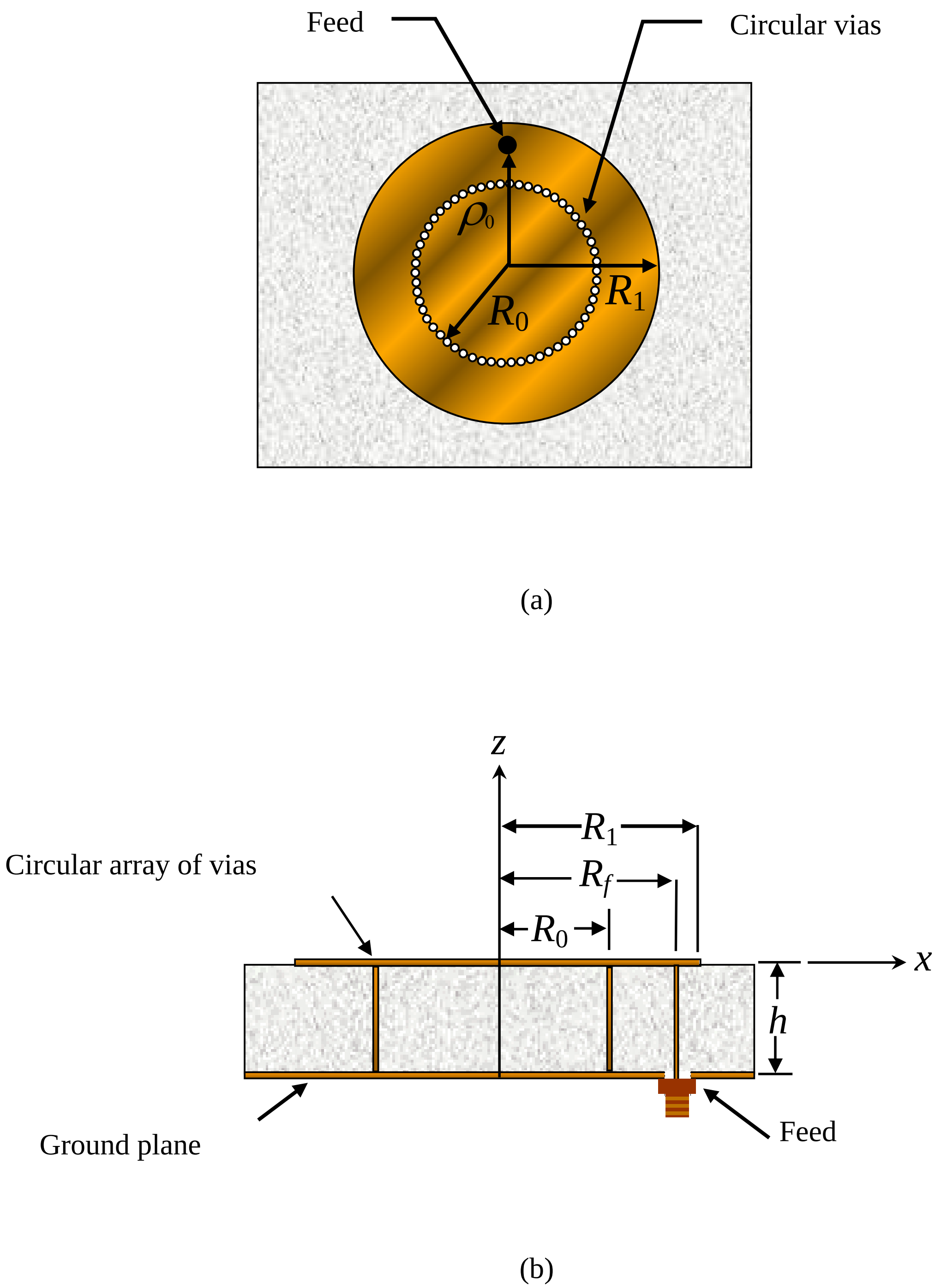

Figure 5.1. Shorted Annular Ring Reduced Surface Wave (SAR-RSW) microstrip antenna. (a) Top view. (b) Side view.

The final RSW antennas, designed using the new procedure where an array of vias is used to create a reactance surface, are simulated in Ansoft HFSS to verify the required frequency and radiation pattern characteristics.

5.1.2 Design Procedure

A new SAR-RSW antenna is designed to operate at the GPS L1 frequency of 1.575 GHz. This antenna is designed using a Rogers Duroid 6002 double-sided copper clad substrate. The substrate thickness is h = 0.1524 cm, the dielectric constant is $\varepsilon_r = 2.94$, and the dielectric loss tangent is $\tan\delta = 0.0012$.

First, the outer radius, R_1 as shown in Figure 5.1 is found using (1.2) as

$$R_1 = 0.055778 \text{ m.} \tag{5.1}$$

The next step is to make the antenna resonant at the desired frequency. In a conventional SAR-RSW design a short-circuit boundary in placed at the radius R_0, in order to make the patch resonant at the desired frequency [4]. In the new design a short-circuit inner boundary is not used. Instead, a surface reactance wall with a nonzero reactance is used. This reactance wall can be easily realized using an array of vias, as has already been explained.

There are several degrees of freedom, such as radius of the via array R_0, the number of vias L, and the radius of each via a. There are also several different ways to manipulate these parameters, but it can be started by choosing the array radius R_0 and then using the PMC cavity analysis explained in section 4.4.1. Then it can be solved for the value of the surface reactance that is placed at this radius, in order to achieve resonance at the desired frequency (1.575 GHz).

Using the PMC cavity analysis and code, we make some conclusions about the behavior of this cavity as illustrated in

Table 5.1. Since a positive-valued wall reactance is used in this design a larger array radius compared to that of a PEC wall is needed. For this design the radius is chosen to be

$$R_0 = 0.03109 \text{ m.} \tag{5.2}$$

Table 5.1. The relationship between the resonance frequency, sheet reactance, and radius of the reactance wall in a PMC cavity shown in Figure 4.1.

ACTION	***RESULT***
Increasing the radius of the array, R_0	Increases resonance frequency, f_0
Increasing the surface (or sheet) reactance value, X_s	Decreases the resonance frequency, f_0

The effective outer radius to be used in the cavity analysis is found using (5.2) and [17] as

$$R_{1,eff} = 0.05673 \text{ m}. \tag{5.3}$$

Using these values for the reactance wall (via array) radius and the effective outer radius in the PMC cavity analysis the required surface reactance value for the chosen resonance frequency must be

$$X_{sur} = 7.592 \text{ Ohm/sq}. \tag{5.4}$$

This surface reactance value can be interpreted in terms of sheet reactance or a reflection coefficient as well. The corresponding sheet reactance is

$$X_s = 7.607 \text{ Ohm/sq}, \tag{5.5}$$

and the corresponding reflection coefficient is

$$\Gamma = 0.999\angle 176.45^\circ. \tag{5.6}$$

These values (5.4, 5.5, 5.6) are used to determine the parameters of the necessary via array. To help understand the via-array behavior with changing parameters, the behavior is tabulated in Table 5.2, based on the results of Section 4.3.

Table 5.2. The relationship between the sheet reactance, frequency, radius of the via array, and the radius of the vias as shown in Figure 2.1.

ACTION	***RESULT***
Increasing the radius of the array, R_0	Increases sheet reactance, X_s
Increasing the radius of the via, a	Decreases sheet reactance, X_s
Increasing the number of vias, L	Decreases sheet reactance, X_s
Increasing the frequency, f	Increases sheet reactance, X_s

The array radius and the frequency are already determined, therefore only the number of vias and the via radius need to be determined. It is convenient to set the number of vias first since it should be an integer number and then find the radius accordingly. For this design the number of vias is chosen as 32, and the corresponding via radius is found to be $a = 0.492$ mm to achieve the required reflection coefficient. The scaled pictures of the original SAR-RSW antenna (214 vias) and the new design with 32 vias are given in Figure 5.2.

For this design to reduce the number of vias to eight at the same array radius as in (5.2), the via radius can be increased

$$a = 3.1369 \text{ mm}. \tag{5.7}$$

This array geometry is shown in Figure 5.3(a). Since the via radius is quite large the radius can be pushed out a little further to obtain reasonable sized vias, and the array radius is thus chosen to be

$$R_0 = 0.035778 \text{ m}. \tag{5.8}$$

Then using the same effective outer radius in (5.3) the necessary surface reactance, sheet reactance, and reflection coefficients are as follows:

$$X_{sur} = 73.079 \text{ Ohm/sq}, \tag{5.9}$$

$$X_s = 70.061 \text{ Ohm/sq}, \tag{5.10}$$

$$\Gamma = 1 \angle 148.522^\circ. \tag{5.11}$$

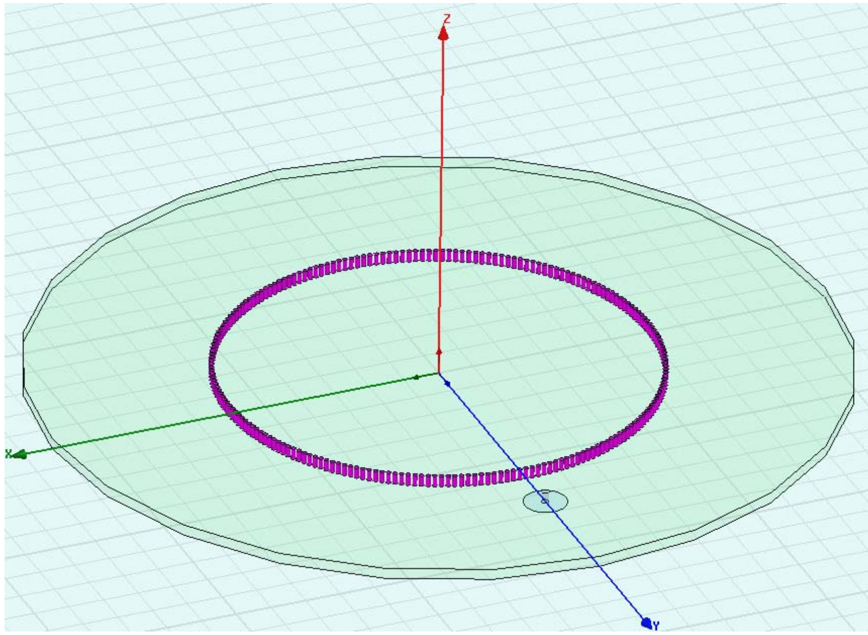

(a)

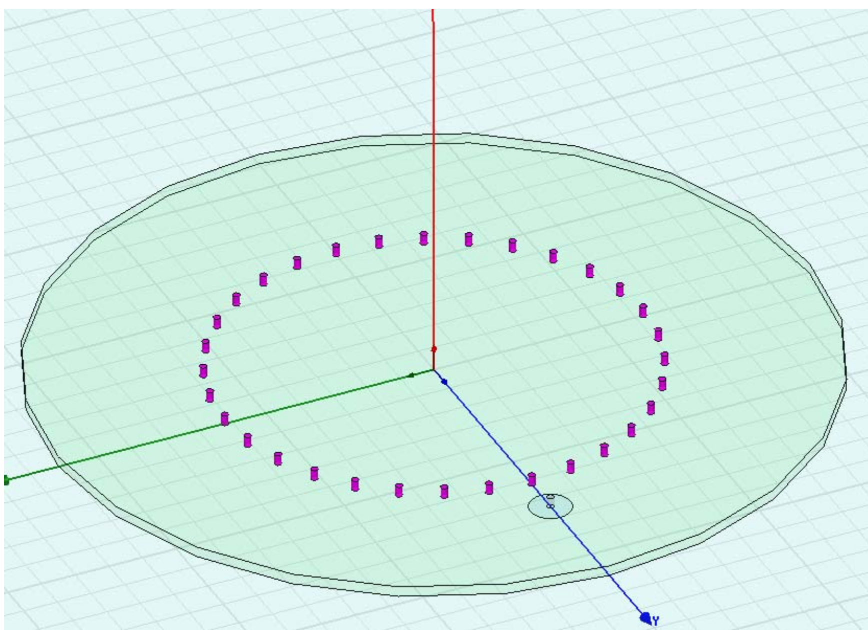

(b)

Figure 5.2. Two different SAR-RSW antennas operating at 1.575 GHz. (a) Original design using 214 vias array at a radius $R_0 = 0.03029$ m. (b) New design using 32 vias array at a radius $R_0 = 0.03109$ m.

An eight-element via array with the specified parameters above can be realized using the via analysis and the radius of each via is found as

$$a = 1.3293 \quad \text{mm}, \tag{5.12}$$

with the corresponding geometry illustrated in Figure 5.3(b). Similarly, a four-element via array can be realized using a radius of each via of

$$a = 6.0584 \quad \text{mm}, \tag{5.13}$$

as shown in Figure 5.4.

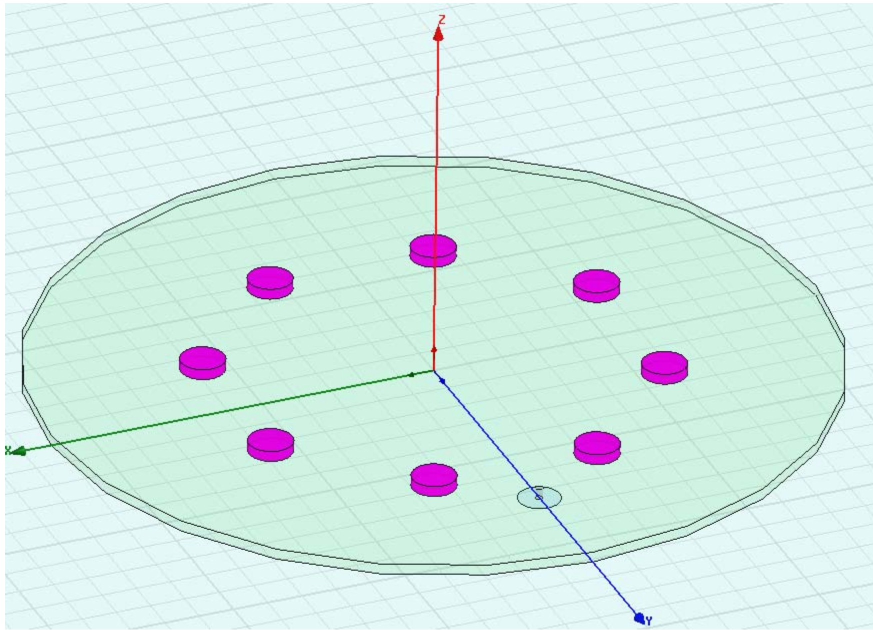

(a)

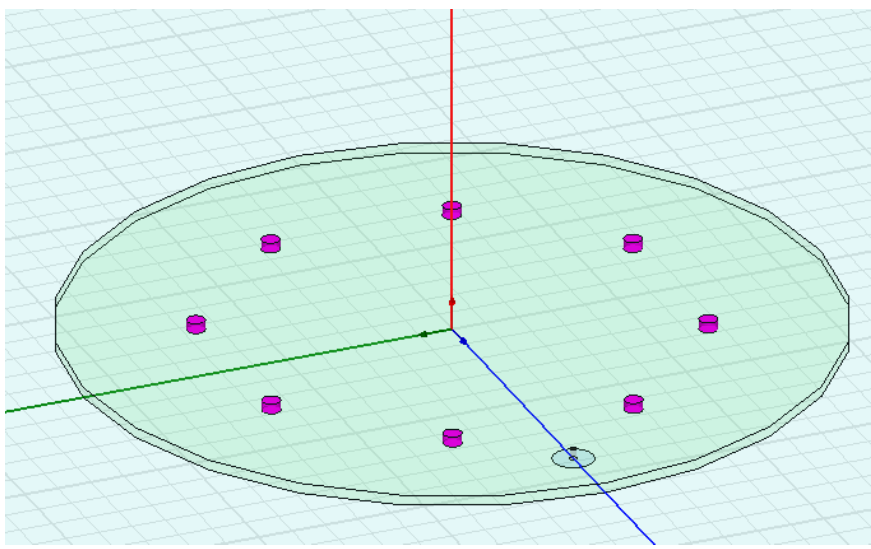

(b)

Figure 5.3. Two different new SAR-RSW antennas operating at 1.575 GHz. (a) Using 8 vias at a radius $R_0 = 0.03109$ m. (b) Using 8 vias at a radius $R_0 = 0.035778$ m.

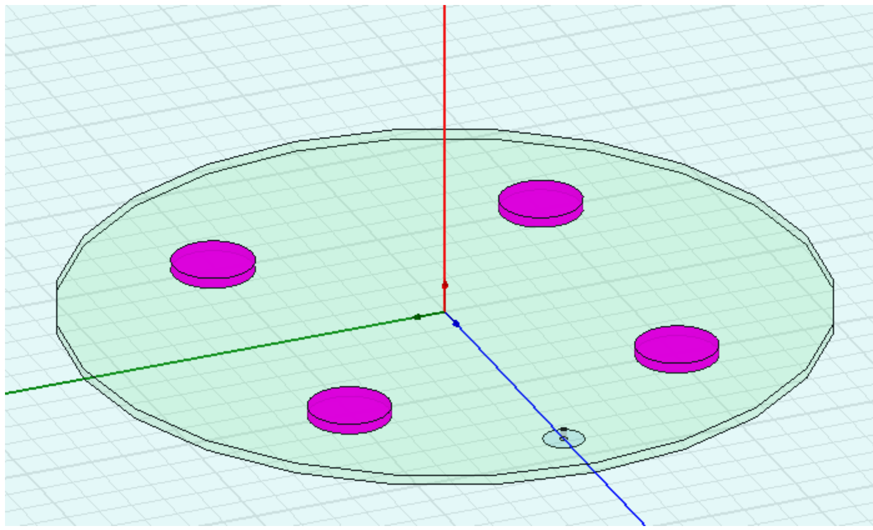

Figure 5.4. A new SAR-RSW antenna operating at 1.575 GHz. using 4 vias at a radius $R_0 = 0.035778$ m.

5.1.3 Resonance Frequencies and Radiation Patterns

The resonance frequencies and the radiation patterns of the designed RSW antennas are presented in order to investigate the new technique of designing antennas with a reactance wall. The resonance frequencies of the RSW antennas found using the HFSS simulation tool are given in Table 5.3. Table 5.6 shows the resonance frequencies of the previously designed RSW antennas [5] found using the HFSS tool. The resonance frequencies are determined by finding the frequency where the maximum of the real part of the input impedance occurs. The radiation patterns of the RSW antennas are also given in Figures 5.5-5.10.

Table 5.3. The resonance frequencies of the RSW antennas designed in Section 5.1 as determined by HFSS simulation tool.

RSW DESIGN FIGURE NUMBER	NUMBER OF VIAS	PATCH RADIUS (cm)	VIA ARRAY RADIUS (cm)	VIA RADIUS (mm)	FEED LOCATION (cm)	RESONANCE FREQUENCY (GHz)
Figure 5.4	4	5.5778	3.5778	6.0584	4.405	1.559
Figure 5.3.a	8	5.5778	3.1090	3.1369	3.705	1.597
Figure 5.3.b	8	5.5778	3.5778	1.3293	4.4	1.590
Figure 5.2.b	32	5.5778	3.1090	0.4920	3.705	1.589

Table 5.4. The resonance frequencies of the RSW antennas in [5] determined by HFSS simulation program.

NUMBER OF VIAS	PATCH RADIUS (cm)	VIA ARRAY or PEC RADIUS (cm)	VIA RADIUS (mm)	FEED LOCATION (cm)	RESONANCE FREQUENCY (GHz)
PEC Wall	5.5778	3.0290	-	3.705	1.576
214	5.5778	3.0290	0.3175	3.705	1.594

The results in Table 5.3 show that the resonance frequencies of the antennas with 8 and 32 vias are a bit higher than the design frequency, which is 1.575 GHz. This is because of the difference between the analytical design method and the simulation method of the HFSS tool. In particular, the analytical design method in Chapter 5.1.2 doesn't take the probe impedance into account whereas HFSS does. A higher frequency than the design frequency is an expected result of ignoring the probe effect. A larger frequency difference in the 4-via case is explained in the following section, where the design limitations are discussed.

The radiation patterns of the antennas with 8 or 32 vias, designed using the new technique are quite similar to those of the original design using a PEC wall or a large number of vias [5]. The size of the ground plane used is 32 cm by 32cm with the same size of dielectric region.

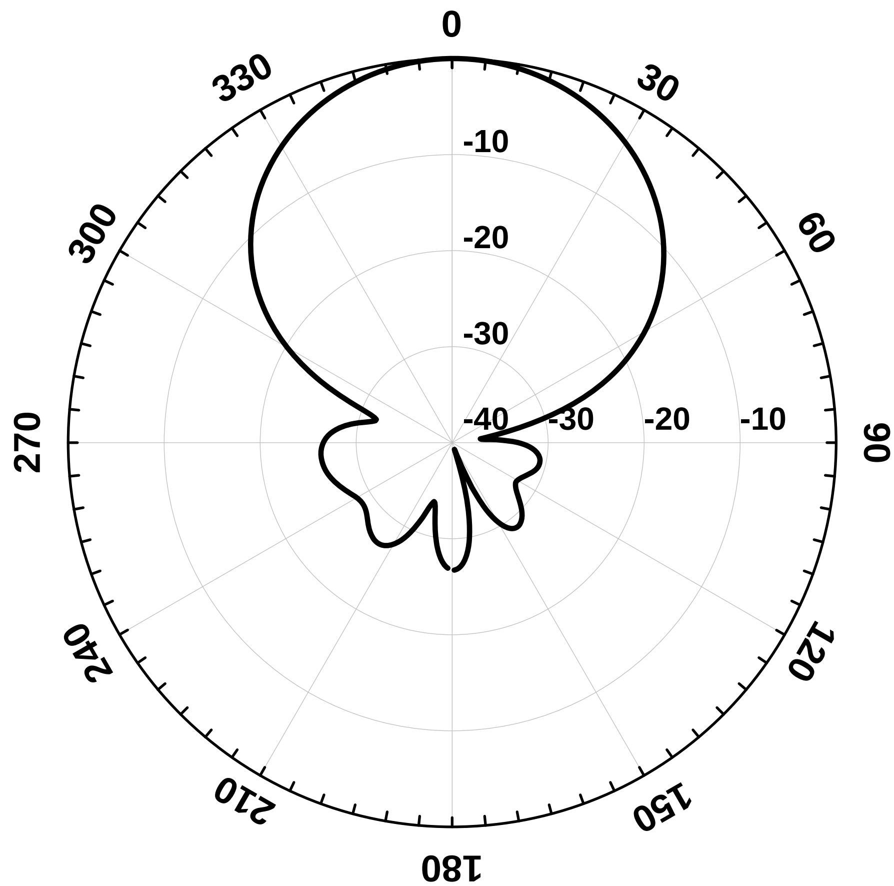

Figure 5.5. E-plane radiation pattern of a SAR-RSW antenna operating at 1.576 GHz, with the PEC short-circuit wall at a radius of 3.029 cm and a patch radius of 5.5778 cm.

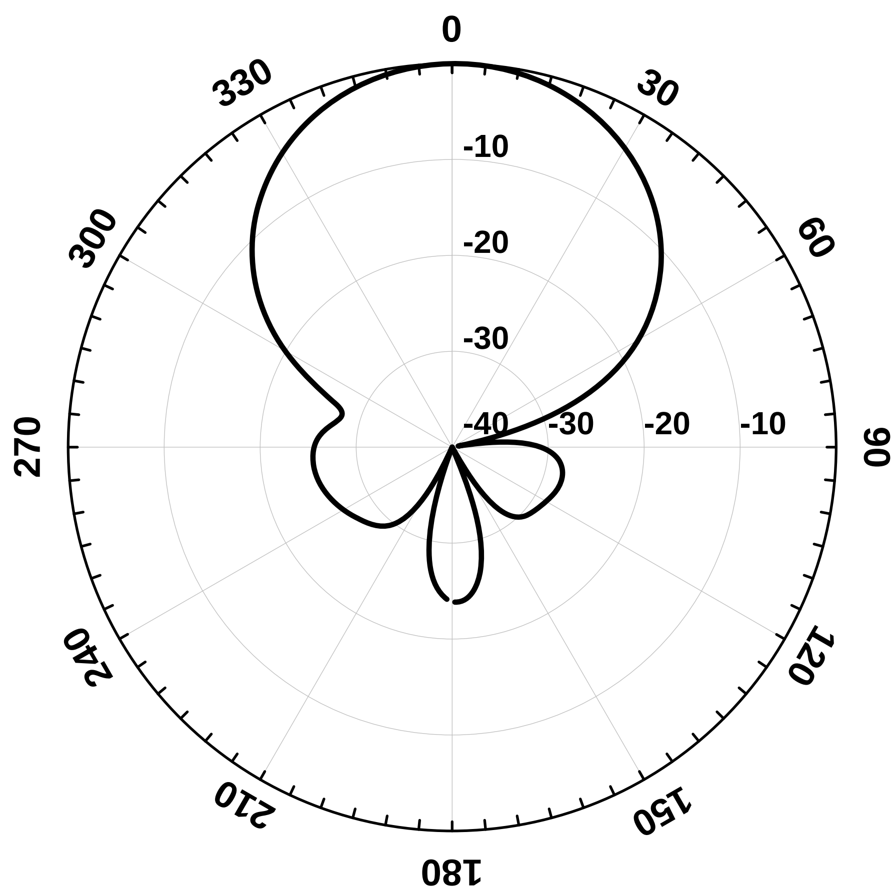

Figure 5.6. E-plane radiation pattern of a new SAR-RSW antenna operating at 1.594 GHz with the number of vias being 214, the patch radius 5.5778 cm, the via-array radius 3.029 cm, and the via radius 0.3175 mm. The antenna is shown in Figure 5.2(a).

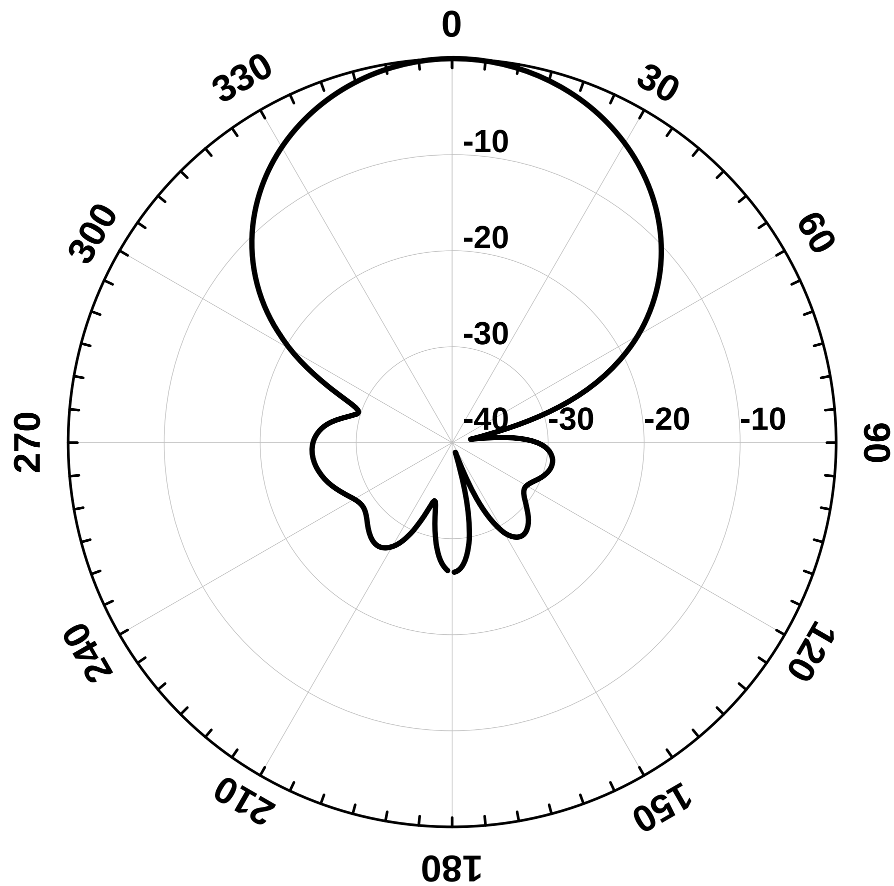

Figure 5.7. E-plane radiation pattern of a new SAR-RSW antenna operating at 1.589 GHz with the number of vias being 32, the patch radius 5.5778 cm, the via-array radius 3.109 cm, and the via radius 0.492 mm. The antenna is shown in Figure 5.2(b).

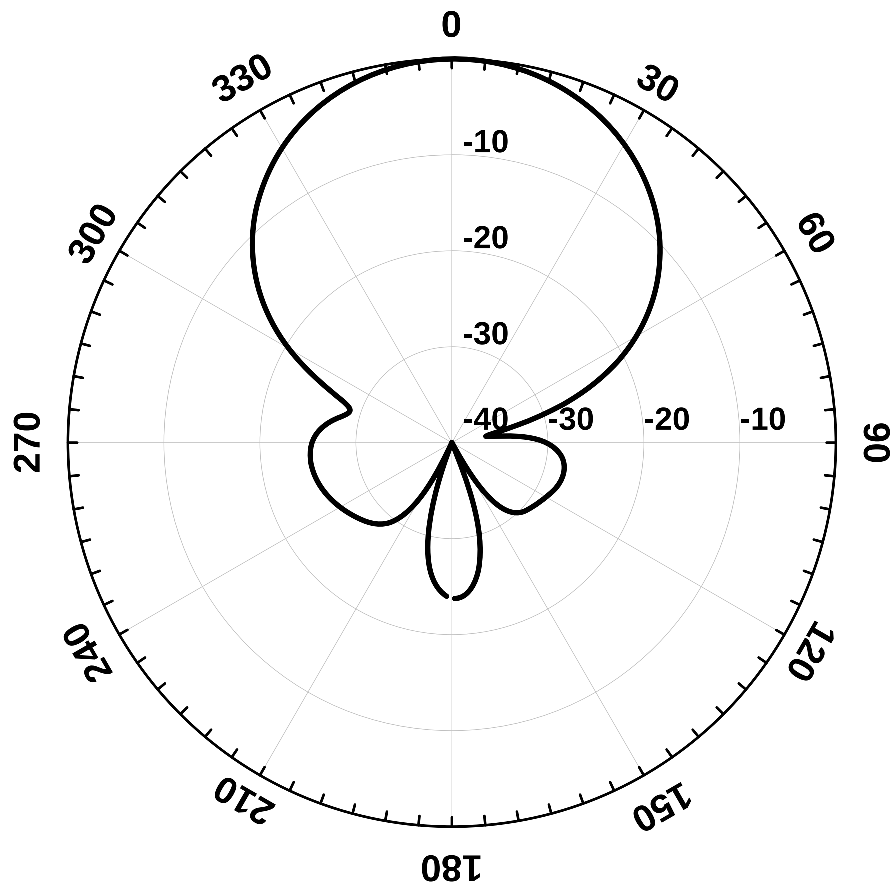

Figure 5.8. E-plane radiation pattern of a new SAR-RSW antenna operating at 1.597 GHz with the number of vias being 8, the patch radius 5.5778 cm, the via-array radius 3.109 cm, and the via radius 3.1369 mm. The antenna is shown in Figure 5.3(a).

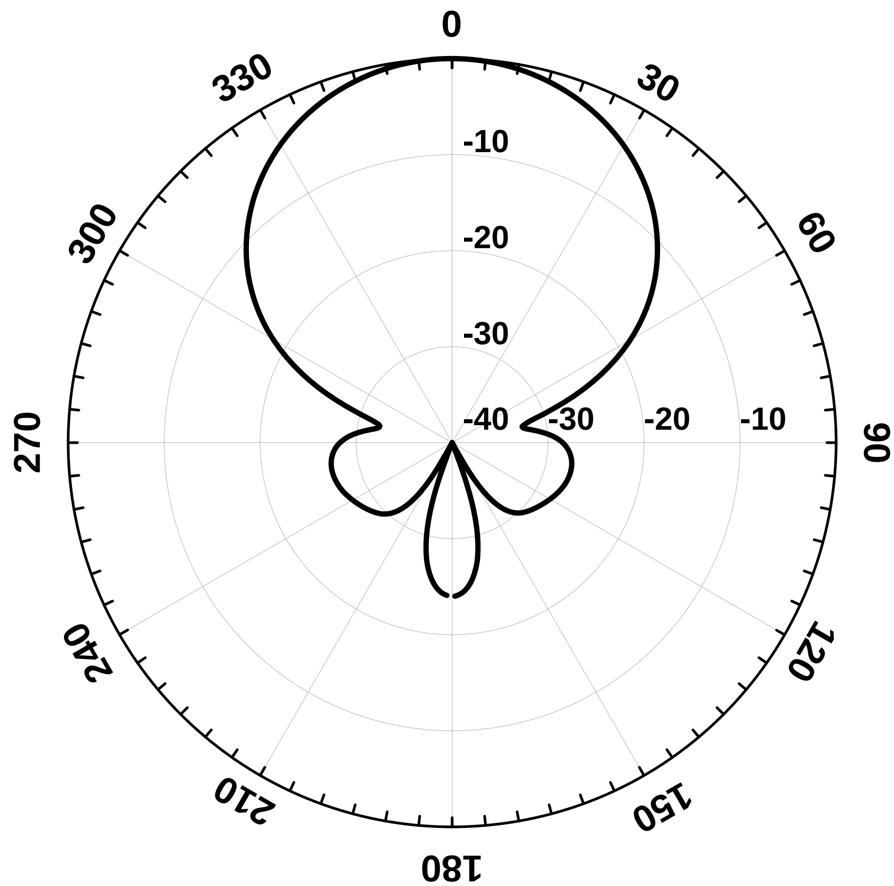

Figure 5.9. E-plane radiation pattern of a new SAR-RSW antenna operating at 1.590 GHz with the number of vias being 8, the patch radius 5.5778 cm, the via-array radius 3.5778 cm, and the via radius 1.3293 mm. The antenna is shown in Figure 5.3(b).

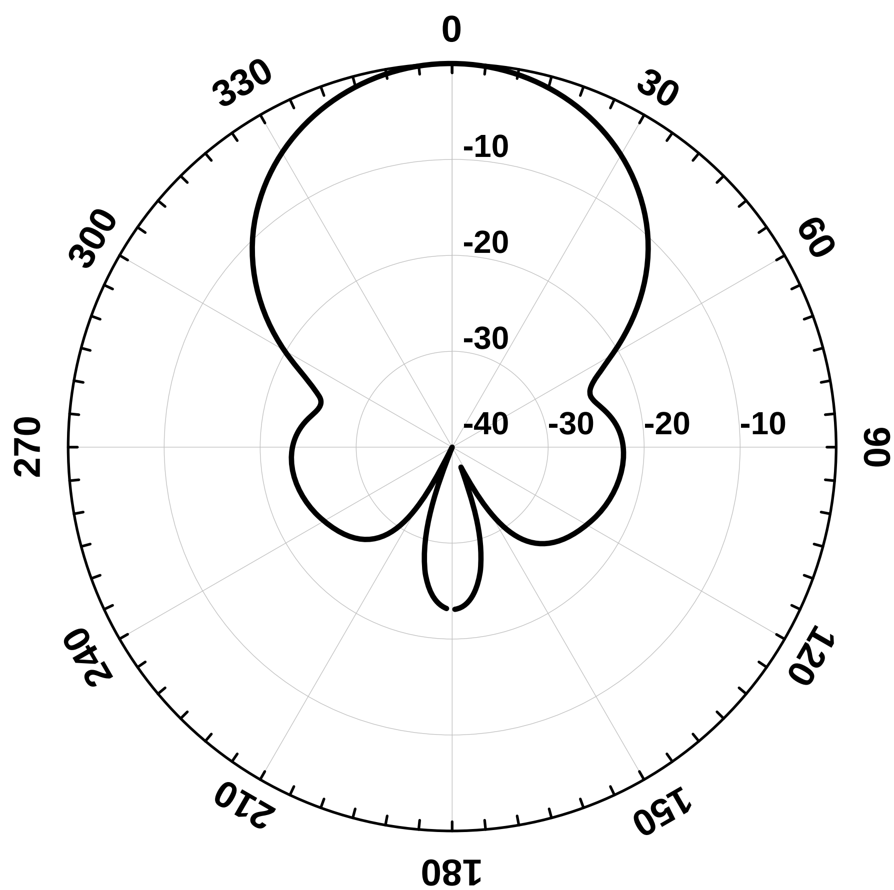

Figure 5.10. E-plane radiation pattern of a new SAR-RSW antenna operating at 1.559 GHz with the number of vias being 4, the patch radius 5.5778 cm, the via-array radius 3.5778 cm, and the via radius 0.3175 mm. The antenna is shown in Figure 5.4.

5.1.4 Limitations of the New RSW Antenna Design Technique

The new design technique presented in Section 5.1.2 models the via array as an equivalent reactance sheet in the cavity model, and implicitly assumes that the higher-order modes generated at the via array do not effect the operation of the antenna. In particular, the higher-order modes reflected from the outer PMC wall of the patch antenna at $\rho = R_1$ should decay enough so as not to induce significant currents on the vias at $\rho = R_0$, as shown in Figure 5.11.

The validity of the new design technique is tested by looking at the ratio of the higher order electric field given in (2.50) that is reflected from the outer radius and evaluated at the inner radius, to the incident electric field at the radius of the via array, as

$$\text{Decay} = \left| \left. \frac{E_z\big|_{\rho=R_0+2\Delta}}{E_z\big|_{\rho=R_0}} \right|_{p=1,-1} \right|. \tag{5.14}$$

This formula assumes the electric field propagates with the same functional form after it is reflected from the outer boundary. Table 5.5 summarizes the decay values for the designed SAR-RSW antennas using the new technique.

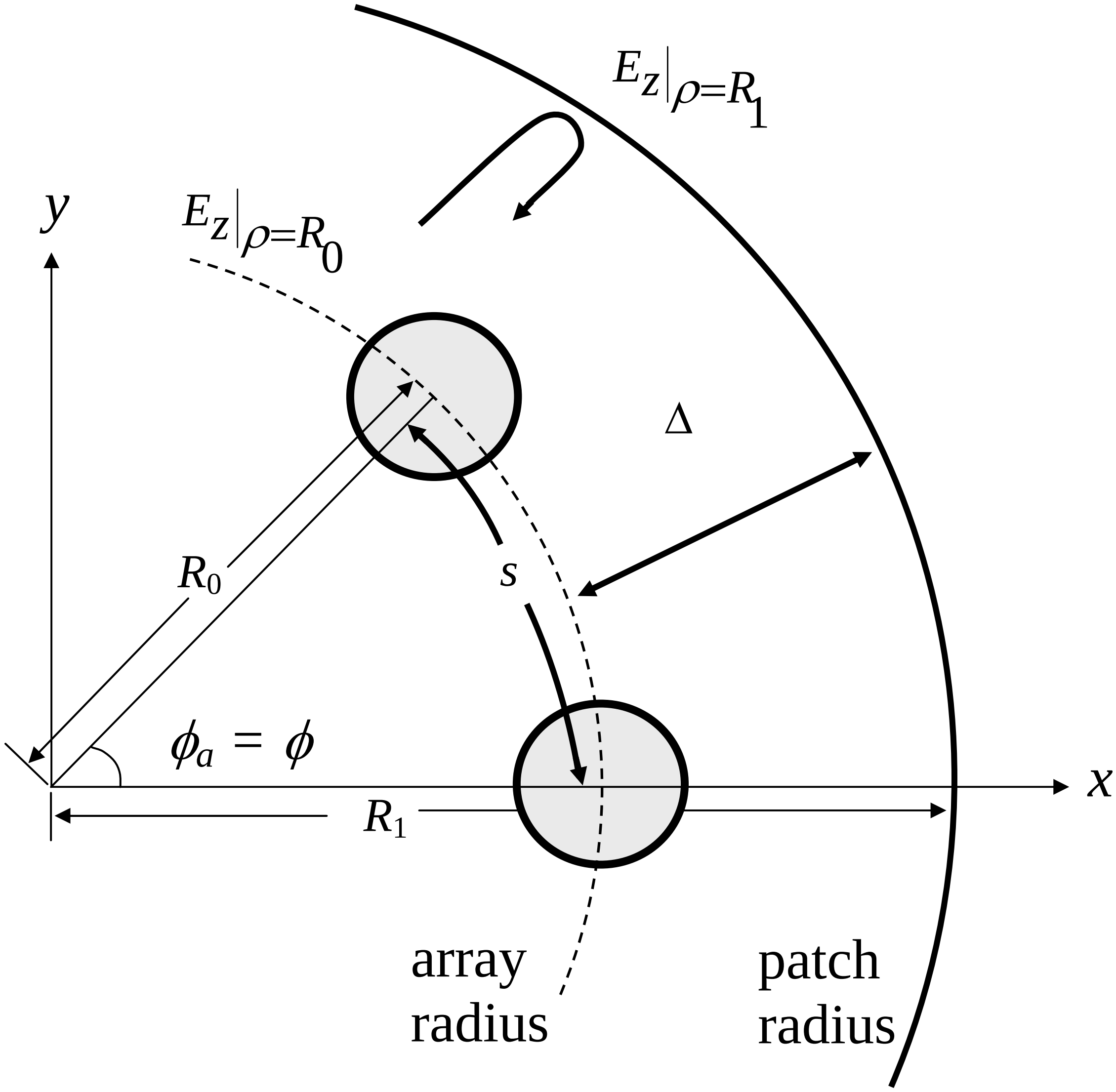

Figure 5.11. The electric fields at the via array and at the outer patch radius of the SAR-RSW antenna.

Table 5.5. The decay values for the electric fields for the designed SAR-RSW antennas.

RSW DESIGN FIGURE NUMBER	NUMBER OF VIAS	DISTANCE RATIO (Δ/s)	DECAY RATIO OF THE ELECTRIC FIELD (*p*=1)	DECAY RATIO OF THE ELECTRIC FIELD (*p*=-1)
Figure 5.4	4	0.36	0.021	0.180
Figure 5.3(a)	8	1.01	0.0018	0.013
Figure 5.3(b)	8	0.7	0.00022	0.0015
Figure 5.2(b)	32	4.04	10^{-16}	10^{-10}

As it can be seen from Table 5.5, the effect of higher-order modes is negligible in the 8- and 32-via cases but not in 4-via case, which explains the difference in the resonance frequency for 4-via design. Looking at the distance ratio values, it is concluded that the ratio of the distance between the inner and outer radii to the separation of the vias should be greater than one in order to design SAR-RSW antennas using the new technique.

5.2 Design of UHF Band Microstrip Antenna for Public Safety Vehicles

5.2.1 Introduction

A new low-profile multi-band antenna system (shown in Figure 5.12) was designed for public safety vehicles to cover the Ultra High Frequency (UHF), Global Positioning

System (L1-GPS), and Wireless Fidelity (Wi-Fi) bands [18]. The UHF frequencies are covered with a dual-band center-fed circular patch antenna, partially filled with a dielectric core and loaded with a fence of metallic posts.

The UHF antenna radiates with a monopole-like pattern. The dielectric core is used to reduce the antenna radius while the fence of posts is used to create and tune the dual resonances of the antenna. The input impedance versus frequency is shown in Figure 5.14, indicating the dual resonance. This system is approximately 30 cm in diameter and 1.5 cm in height. It covers the UHF bands 450 MHz–512 MHz and 746 MHz–869 MHz with a Voltage Standing Wave Ratio (VSWR) less than 2 and a horizon roll-off under 3 dB.

The UHF antenna design procedure followed in [18] is based on the cavity model analysis and HFSS simulations of the antenna. The antenna is modeled as a PMC wall cavity (PEC top and bottom and PMC side wall) as shown in Figure 5.13. Then the cavity problem is analyzed to find the required reactance wall inside the cavity.

The sheet reactance is realized with a particular number of vias and a particular via radius. This design is simulated in HFSS to obtain the input impedance versus frequency characteristics. An input impedance characteristic with respect to frequency was also obtained from the cavity analysis. Then these curves are compared. By changing the number of vias and their radius in HFSS, the curves are matched by trial and error (as

(a)

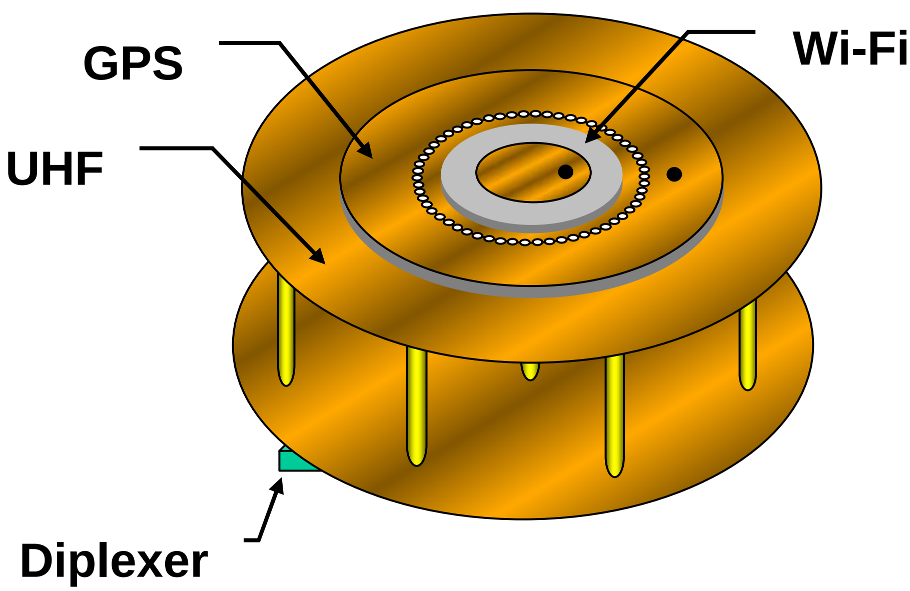

(b)

Figure 5.12. (a) Various antennas currently used in public safety vehicles and the proposed multiband low-profile antenna. (b) Detailed schematic of the multiband antenna.

illustrated by a comparison of the results shown in Figure 5.14, discussed later), giving the required via-array geometry [18].

This previously used iterative method can be replaced by an easier and faster method based on the use of the via analysis in Chapter 2 to realize the via-array geometry. After finding the required sheet reactance, the corresponding via-array geometry can be found directly using the via-array analysis. In this section, the results from the iterative design and via analysis are compared to show the accuracy of the via-array analysis.

5.2.2 Cavity Model Analysis of Dual-Band UHF Antenna

The center-fed antenna is modeled as a cavity as shown in Figure 5.13 [18]. The cavity model consists of the feed in the center, the edge conductance at the outer radius, and the sheet reactance model for the via fence. The monopole-like radiation pattern, shown in Figure 5.15, is found by modeling the antenna as a constant ring of magnetic current K_T of radius R_1. The radiated electric field is

$$E(r,\theta,\phi) = 2\pi\,(k_0 R_1)\,K_T\;J_1(k_0 R_1 \sin\theta)\,\frac{e^{-jk_0 r}}{4\pi r}\,\hat{\theta}\,. \tag{5.15}$$

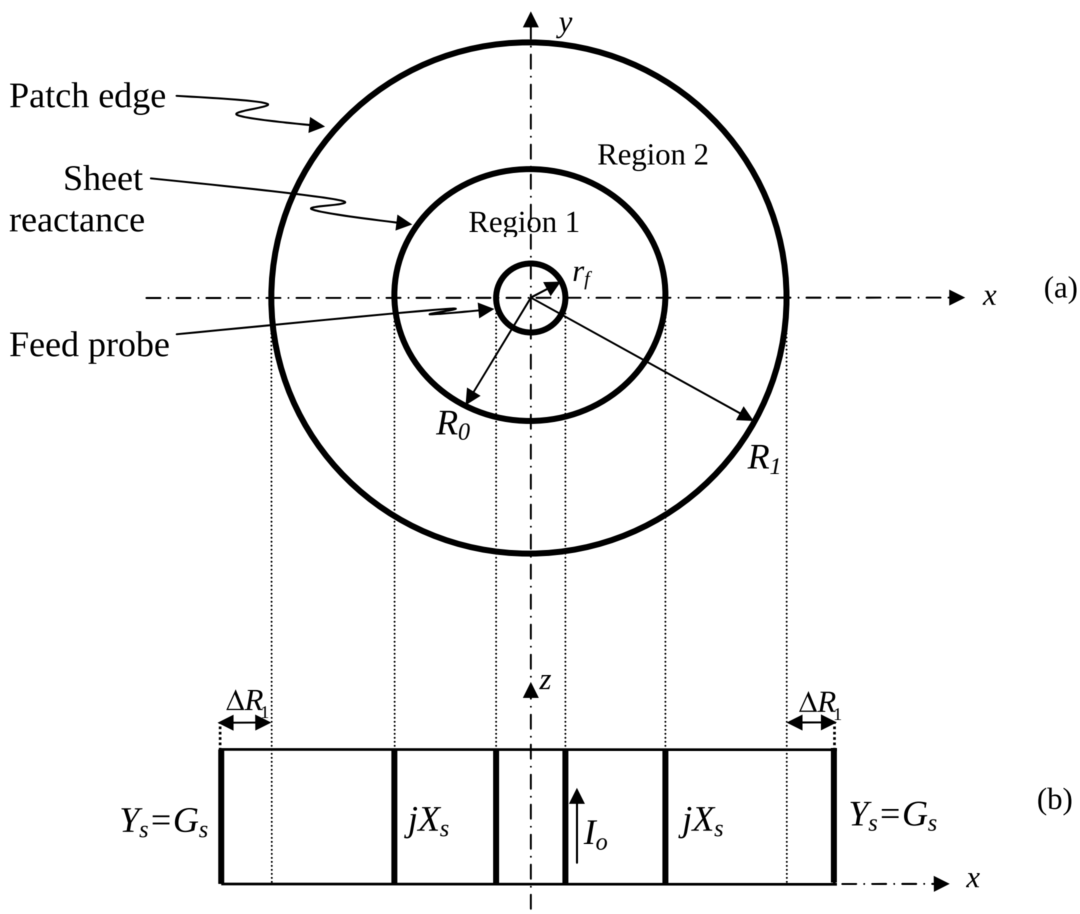

Figure 5.13. The center-fed circular UHF antenna with via-array loading. (a) Top view. (b) Side view.

The equivalent sheet conductance G_s at the radiating edge is found by equating the total power at the cavity side wall and in the far field, and is given as [18], [19]

$$G_s = hR_1\omega\varepsilon_0 k_0 \int_0^{\frac{\pi}{2}} J_1^2\left(k_0 R_1 \sin\theta\right)\sin\theta \, d\theta \,. \tag{5.16}$$

The effect of fringing is accounted for in the analysis by increasing the patch size R_1 by the edge extension [18], using the CAD formula given in [17]

$$\Delta R_1 = \frac{h}{\pi\varepsilon_r}\left(\ln\left(\frac{\pi R_1}{2h}\right) + 1.7726\right). \tag{5.17}$$

Solving the cavity geometry in Figure 5.13 using the boundary conditions at the feed, the impedance surface, and outer radiation surface, an expression for the input impedance is obtained as [18]

$$Z_{in} = -\frac{h}{I_0}\left[AJ_0(kr_f) + BY_0(kr_f)\right], \tag{5.18}$$

where A and B are constants found from the cavity analysis. The input impedance versus frequency is shown in Figure 5.14(b).

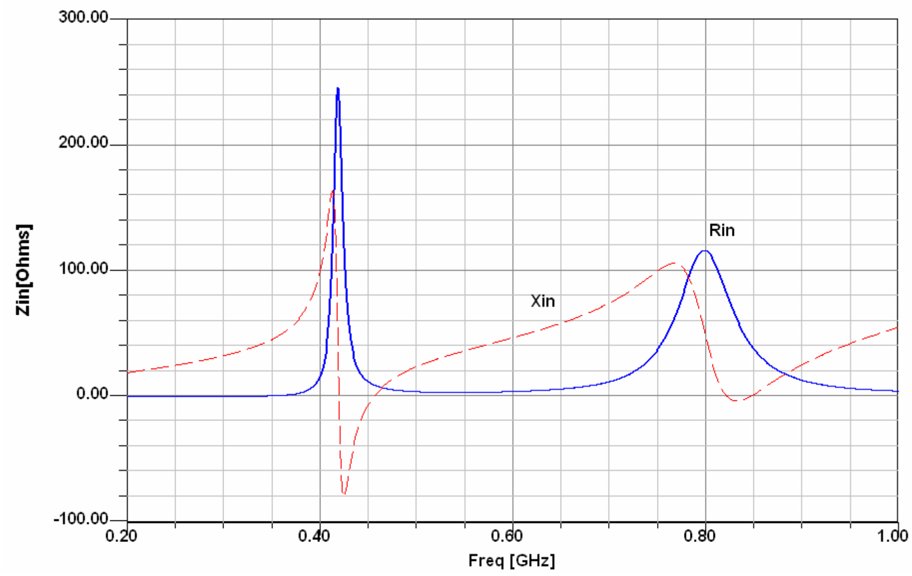

(a)

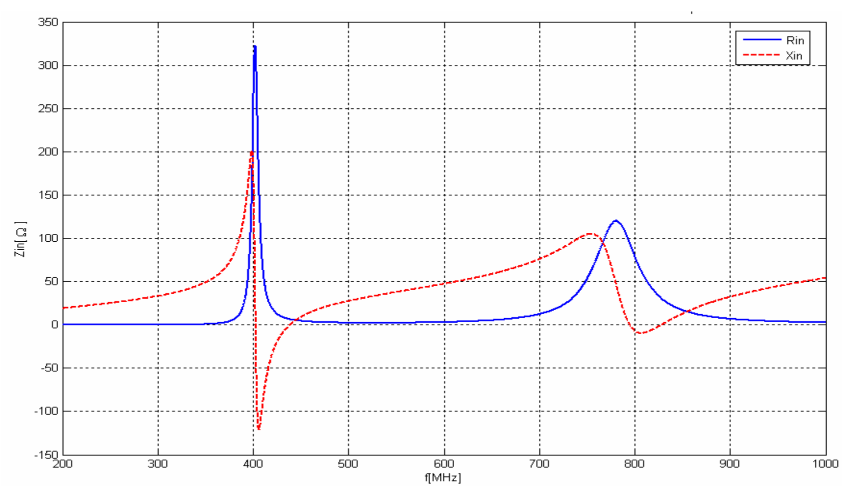

(b)

Figure 5.14. Input impedance vs. frequency characteristics for a center-fed circular UHF antenna, showing the dual-resonance nature of the antenna for the geometry in Table 5.6. (a) HFSS simulation result. (b) Cavity analysis result.

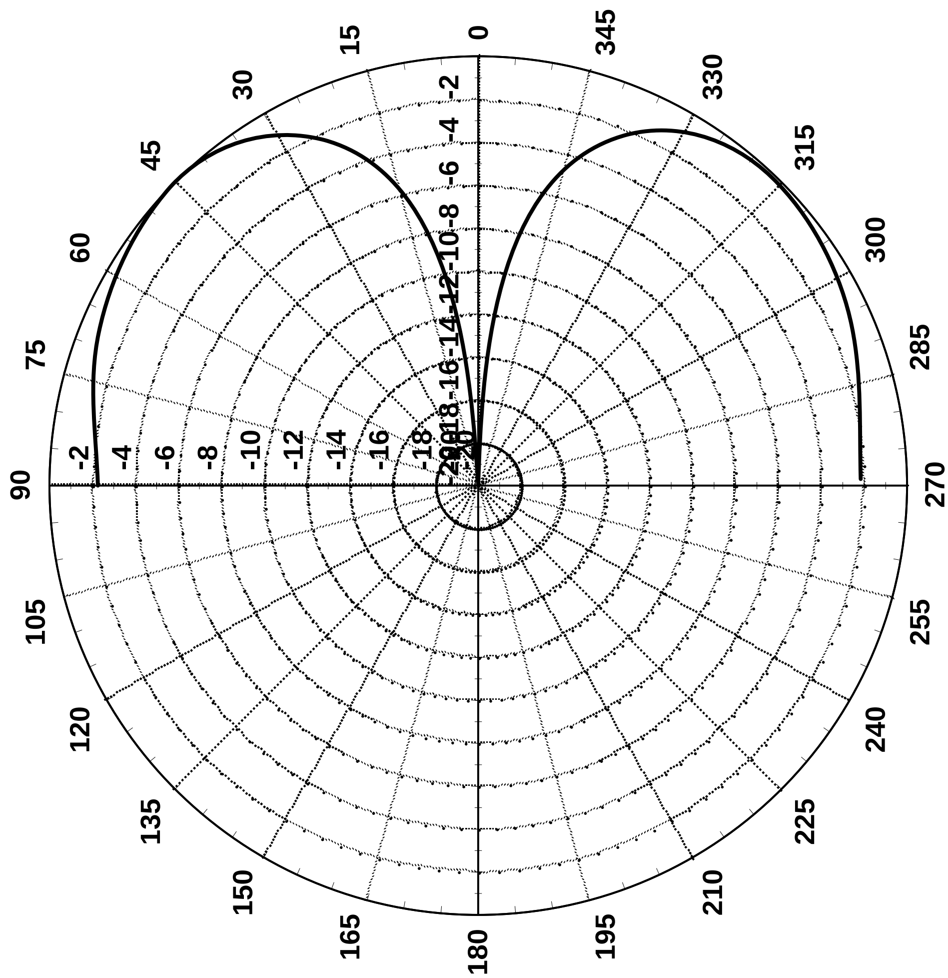

Figure 5.15. The *E*-plane radiation pattern of the center-fed UHF antenna at 869 MHz.

5.2.2.1 Design Procedure for Dual-Band UHF Antenna

As an example, the dual-band UHF antenna given in Table 5.6 is investigated. First, the antenna is designed by solving the cavity problem in Figure 5.13 using boundary conditions for the required surface inductance,

$$L_{sur} = \frac{X_{sur}}{\omega}. \tag{5.19}$$

The surface inductance is found to be 55 nH/sq. The input impedance vs. frequency characteristics of the antenna is shown in Figure 5.14(b). Then the antenna is modeled in HFSS using the geometry given in Table 5.6, as shown in Figure 5.16.

Table 5.6. The dual-band UHF antenna parameters used to obtain the input impedance vs. frequency characteristics of the antenna.

Definition of the Variable	Symbol	Value
Surface Inductance	L_s	55 nH/sq
Radius of the sheet reactance	R_0	11.27 cm
Radius of the cavity	R_1	15.29 cm
Radius of the probe feed	r_p	0.635 mm
Height of the antenna	h	1.27 mm
Frequency	f	varying
Mode number of the incoming wave	n_i	0
The permittivity of the medium	ε_r	2.2

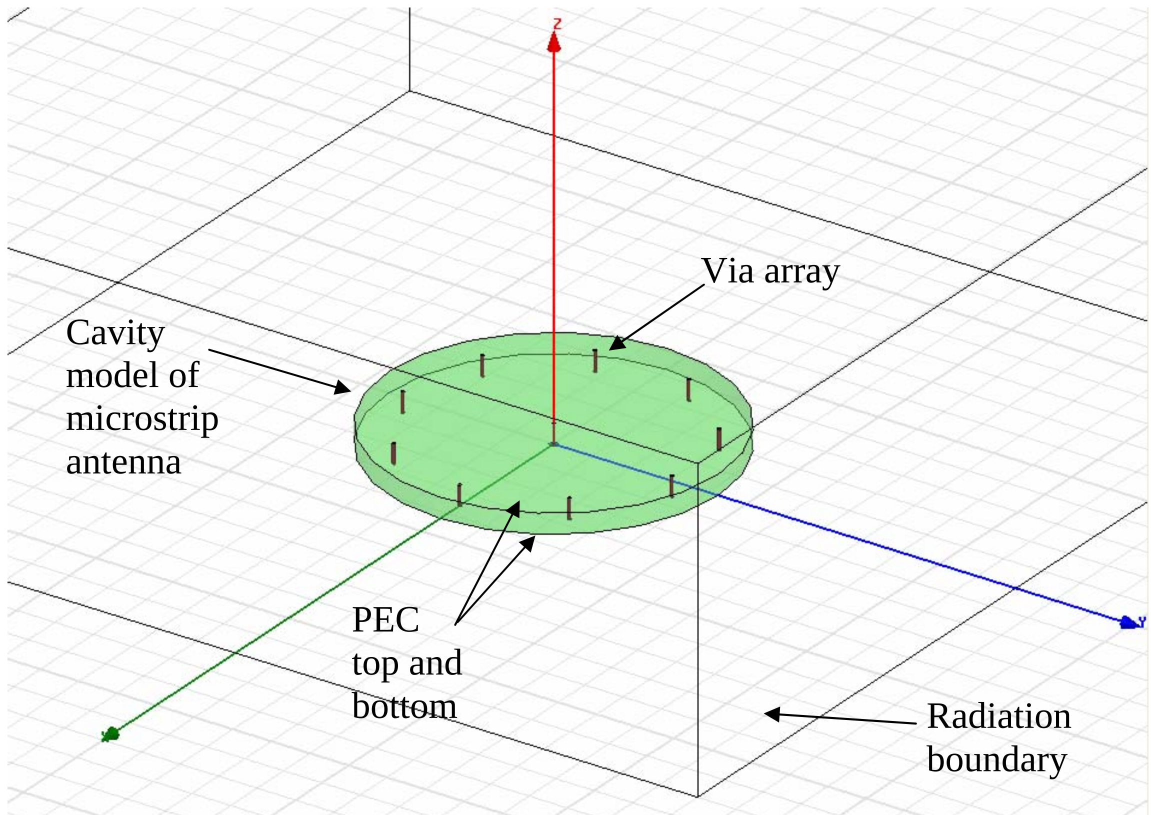

Figure 5.16. HFSS model of the center-fed UHF antenna with the via array.

In the original design procedure the surface inductance (or the surface reactance) of the antenna is realized by a circular array of via elements in HFSS. The location of the via elements is the location of the surface reactance wall in the cavity model but the size and the number of vias is arbitrary at the beginning. The input impedance vs. frequency characteristics is plotted. The number of vias and their radius are manipulated by trail and error until the input impedance characteristics of the cavity model matches that of the HFSS model as shown in Figure 5.14(a). Then the design of via array is complete. In this example, the two plots are matched when the number of vias are 8 and their radius is 0.0635 cm.

The new design procedure using the via-array analysis in Chapter 2 is able to find the number of vias in the fence directly without iterating using HFSS. Once the surface reactance or inductance value of the array and its location is determined by the cavity analysis [18], a practical via radius is chosen, and the number of vias is then found using the via analysis as described in Section 2.2.

5.2.2.2 Results

A comparison of the surface inductance values is given in Table 5.7. This table tabulates in the next-to-last column the surface inductance values required to match the input impedance curves from the cavity analysis and the HFSS simulation for a certain geometry of vias.

The last column has the surface inductance values from the via analysis for the same geometry of via array. It should be noted that the mode number is zero because of the required operation mode of the antenna.

Table 5.7. Comparison of the surface inductances used in the analytical via code and HFSS simulation with the corresponding via code results.

Radius of each via **(a) [cm]**	Radius of the via array **(R_1) [cm]**	Number of the elements in the via array **(L)**	Surface Inductance value used in Cavity Model **(L_{sur}) [nH/sq]**	Surface Inductance values from the Via Code **(L_{sur}) [nH/sq]**
0.0635	11.4	6	73	82.51
0.0635	11.4	8	55	55.86
0.0635	11.4	10	40.5	40.91
0.0635	8.6	6	55	57.19
0.0635	13.5	10	55	52.75

As can be seen from the good agreement in the surface inductance values, the required surface inductance can be realized using the via-array analysis in Chapter 2. The new way of realizing the surface inductance with an array of vias is an easier and faster method than the previous trial-and-error procedure.

5.3 Miniaturized Circular Microstrip Antenna Application of Via Analysis

A circular array of vias can also be utilized to miniaturize microstrip antennas [10]-[12]. A new center-fed conical-beam (monopole-like) microstrip antenna having a circular array of vias that was studied in [9] is shown in Figure 5.17. The radiation pattern of this type of antenna is shown in Figure 5.18.

For a fixed patch size, the change in the resonance frequency of the antenna with a varying number of vias (two, four and eight) located symmetrically with respect to the central feed was investigated [9]. In that study, the optimized miniaturization was achieved by changing the geometry by trial and error using Ansoft Designer simulations.

Also, a cavity model (called the Radial Transmission Line Model (RTL) in the reference) was used in [9] to design and investigate these types of antennas. This analysis uses the same cavity model as shown in Figure 5.13. The cavity problem is analyzed to determine the required sheet reactance. This sheet reactance is realized by an array of vias. The number and the radius of the vias is determined using the via analysis explained in Chapter 2. Results from the analytical design and the HFSS model are compared here, and very good agreement is obtained.

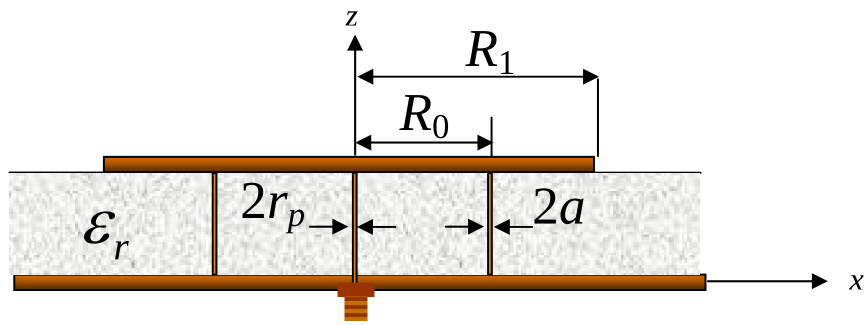

(a)

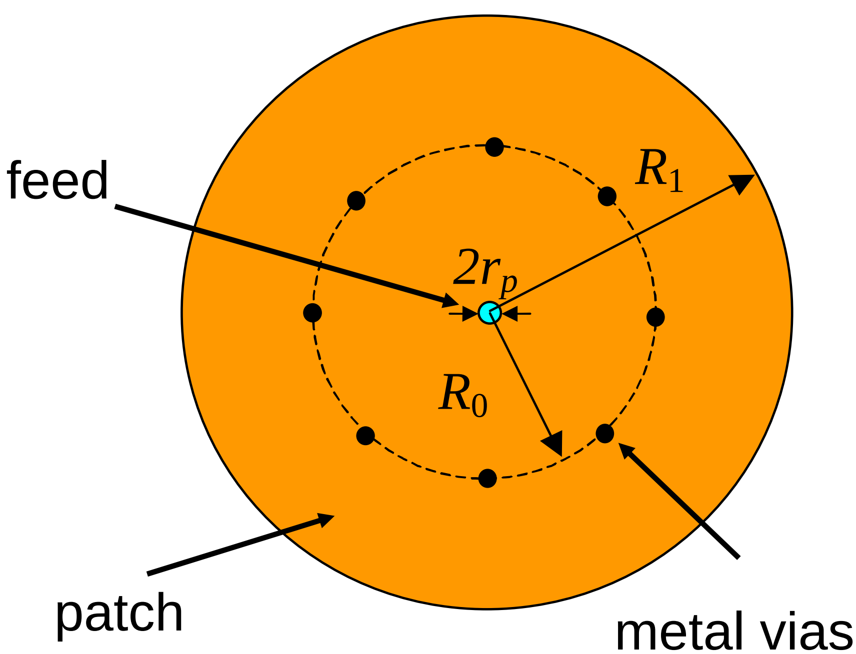

(b)

Figure 5.17. Via-loaded miniaturized microstrip antenna. (a) Side view. (b) Top view.

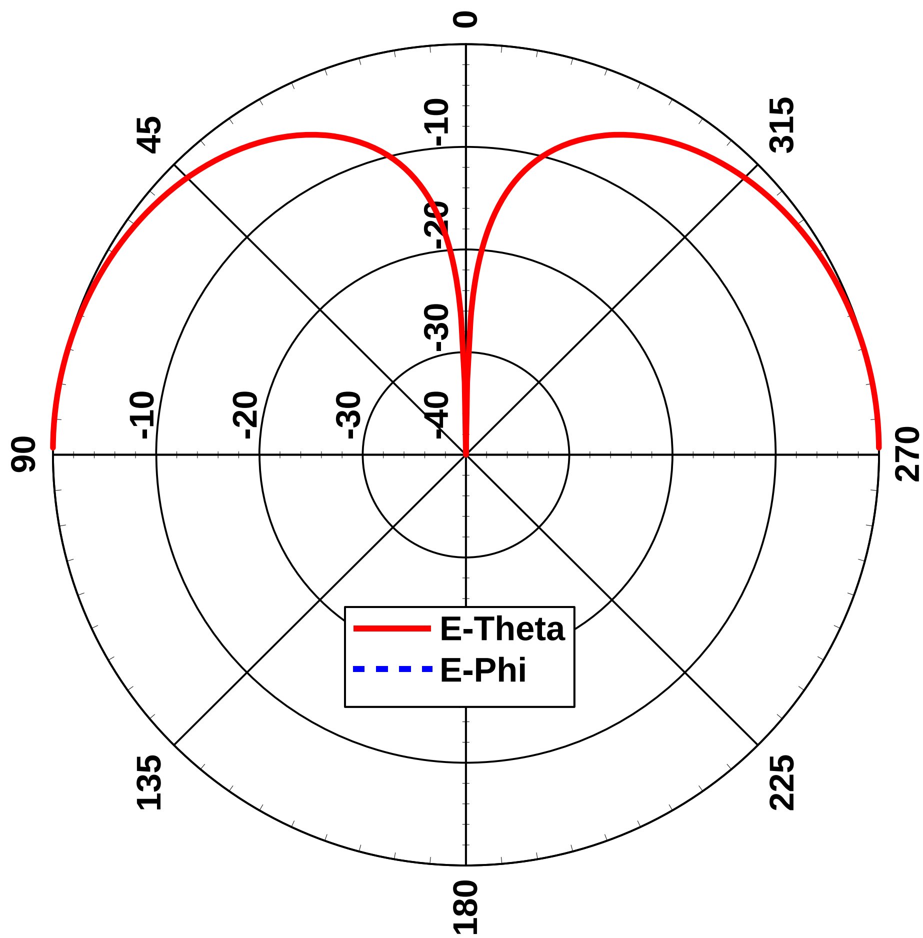

Figure 5.18. E_θ and E_φ patterns at $\phi = 0^\circ$ for a 4-via loaded circular patch. a = 0.635 mm, r_p = 0.3 mm, R_0 = 18.0 mm, R_1 = 34.4 mm, h = 1.6 mm, and ε_r = 1.03. (E_φ is below the level of the scale and is not seen.)

5.3.1 Cavity Model vs. HFSS Simulation Results for Miniaturized Circular Microstrip Antennas

In the cavity model shown in Figure 5.13, the via array is replaced by an ideal sheet reactance X_{sh}, and the outer edge of the patch is replaced with an admittance boundary condition with a surface admittance Y_e at the edge [9].

To validate the cavity model and analysis, a sample antenna geometry is modeled with the parameters given in Table 5.8 [9]. This antenna with the via array is simulated in HFSS to obtain the input impedance vs. frequency characteristics. Then the via-array geometry inside the antenna is expressed in terms of an equivalent sheet reactance using the analysis explained in Chapter 2. The equivalent sheet reactance of the via array is converted to a sheet inductance by using the following simple relation,

$$L_{sh} = \frac{X_{sh}}{\omega} . \tag{5.20}$$

For a 4-via loaded circular patch with the geometry given in Table 5.8, the equivalent sheet inductance is found as $L_{sh} = 15.4$ nH/sq .

Table 5.8. The miniaturized microstrip antenna variables used to find the input impedance vs. frequency characteristics of the antenna.

Definition of the Variable	**Symbol**	**Value**
Radius of the via elements	a	0.3 mm
Radius of the via array	R_0	18 mm
Radius of the cavity	R_1	34.4 mm
Radius of the probe feed	r_p	0.635 mm
Height of the antenna	h	1.6 mm
Number of current basis functions	$2N+1$	25
Frequency	f	varying
Mode number of the incoming wave	n_i	0
Number of via elements	L	4
The permittivity of the medium	ε_r	1

Using this equivalent sheet inductance (corresponding to the via array) the input impedance vs. frequency characteristics is obtained from the cavity-model (RTL) analysis. Figure 5.19 compares the S_{11} characteristics of the antenna, simulated in HFSS and calculated from the RTL analysis using the equivalent sheet reactance model of the via array.

As can be seen from the plot, the cavity model agrees with the HFSS simulation very well. This indicates that the via analysis discussed in Chapter 2 is modeling the via array accurately and it is quite suitable for this application. Modeling a via array with an equivalent sheet reactance and then analyzing the antenna using the cavity model is much easier and faster than the trial-and-error method involving HFSS to obtain the required design.

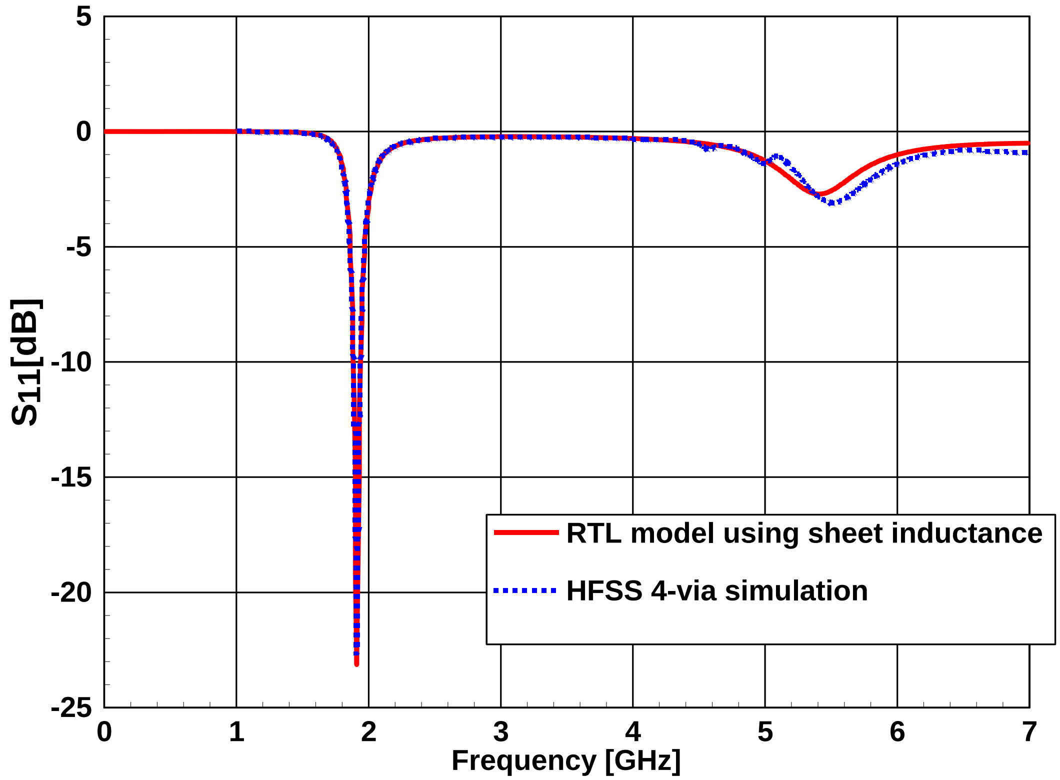

Figure 5.19. S_{11} versus frequency for a 4-via loaded circular microstrip patch antenna, from HFSS simulation and from the cavity model using the sheet inductance calculated from the via analysis in Chapter 2. The antenna geometry is given in Table 5.8.

Chapter 6
Summary and Conclusions

A circular array of vias (conducting metal posts) has an important role in many types of antennas, including microstrip antennas. Therefore, an accurate analysis of the via array was established in this dissertation to understand their behavior and to design antennas that incorporate these structures. The circular array of vias was analyzed analytically, and the analysis was validated. Applications of the via array to practical antenna geometries was then presented.

This dissertation includes three main topics: (1) an electromagnetic analysis of the circular array of vias, (2) validation of the analytical calculations, and (3) a discussion of the properties of the via array and applications of the via array to three different types of antennas. These topics are summarized in more detail below

6.1 Electromagnetic Analysis of Circular Array of Vias

In Chapter 2, an accurate full-wave electromagnetic analysis of a circular array of vias that are sandwiched between two infinite perfectly conducing planes is given. First the vias are modeled as infinitely long cylinders using image theory (since there is no assumed vertical variation of the fields). Using the field radiated from a single cylinder centered at the origin as the starting point, the total field scattered from a circular array of cylinders is expressed in terms of currents on each via.

The unknown current on each via is represented as a summation of current basis functions. It is observed that the current distribution on each via is the same, except for a rotation of the local coordinates and a phase shift due to the phase of the incoming field, which is assumed to have an azimuth variation of the form $\exp(-jn_i\phi)$. Hence, the current basis functions only need to be defined on a single unit-cell via (called via number zero).

Defining an impressed field as the sum of the incident field and the field that is reflected field from the *z*-axis in the absence of the vias and a scattered field due to the currents on the vias, the method of moments (MoM) using electric field integral equation (EFIE) is applied to find the unknown current on the zero via (and hence the currents on all of the vias). The EFIE enforces that the total tangential electric field vanishes on the surface of perfect electric conductor (PEC) vias. The matrix elements and the right-hand side terms in the MoM procedure consist of integrations in variables that are defined in different coordinate systems with respect to the various via locations and the origin. To obtain analytical results, the addition theorem for cylindrical harmonics is used to enable the Bessel functions to be expressed in the same coordinate system (either the center of the via array of the center of the zero via, depending on the calculation). The current on the zero via is then found by solving the MoM matrix equation. Once the currents on the vias are known, the scattered field (the field radiated by the currents on the vias) in the medium may be calculated.

In order to investigate the via-array characteristics, a reflection coefficient for the via array is defined. It is defined as the ratio of the total field propagating away from the via array to the total field propagating towards the via array. Two different reflection coefficients are defined, one looking from the exterior toward the via array (Γ_{EXT}) and the other looking from the interior of the array (Γ_{INT}).

To help validate the via analysis, an independent analysis of a circular array of flat strips is presented. In this case each circular via is modeled by a flat metallic strip. The current on each strip is assumed to be uniform and the effective width of the strips is chosen to best model the radius of the circular vias under the assumption of a uniform strip current. The assumption of a uniform current in the strip model (along with corresponding effective width of the strips) is accurate when the vias are not too closely spaced. Modeling the circular array of strips as a large tube of surface current, and using an analysis based on a cylindrical wave expansion, the scattered field from the strip array is found. The reflection coefficient is then also found as before.

The reflection coefficients are then expressed in terms of equivalent sheet and surface impedances using appropriate boundary value modeling. These characterizations of the via array are very practical and useful in designing and analyzing antennas consisting of via arrays. The sheet impedance models the properties of the via array only and is uniquely defined regardless of whether the incident wave impinges on the array from the interior or the exterior region. The sheet impedance is the ratio of the vertical electric field to the vertical surface current. The surface impedance models the via array together with the interior or exterior region, depending on the region of incidence. The surface impedance is the ratio of the vertical electric field to the vertical surface current on the surface impedance wall that models the via array and the region that is on the opposite side of the array from the region that the incident wave impinges from.

Chapter 3 introduces a calculation of the losses occurred on the via array, since they are not perfect electric conductors in practice, by allowing for a non-zero value of surface resistance for the metal. The total loss in the array is found by summing the individual losses in each via. An equivalent sheet resistance is then found by equating the power lost in the via array to that of an equivalent (lossy) sheet impedance model.

6.2 Numerical Validation of the Via-Array Analysis and Properties of a Via Array

In Chapter 4, the accuracy of the via-array analysis, which models the current on a single (unit cell) via in terms of basis functions, is validated by comparing with the strip model. The reflection coefficient values obtained by varying the parameters of the via array are first compared for an air medium and a good agreement is observed between the two methods. The reflection coefficients approaches -1 as the number of vias increases, indicating that the via array acts as a short-circuit wall.

The relative permittivity of the medium is then changed from unity (air medium) to 2.94 and the validation is repeated by changing the number of vias. Again the two methods agree very well and the reflection coefficient approaches -1 as the number of vias increases. Comparing the reflection coefficients between the air medium and the dielectric medium, it is observed that the reflection coefficient values in a medium with a smaller permittivity act more like a short-circuit wall than in a medium with a higher permittivity for the same via geometry.

The radius of the vias is then varied and the reflection coefficients are calculated using both the via and the strip methods, resulting in a very good agreement between these two methods. The reflection coefficient approaches -1 as the via radius is increased.

The effects of changing the radius of the via array on the reflection coefficient is also investigated. The reflection coefficient approaches -1 as the radius of the via array is decreased, for the same number of vias. A good agreement between the via analysis and the strip model is again observed.

A convergence study for the circular via array is also included. The number of basis functions describing the current on the zero via is increased, and the reflection coefficients are examined for convergence. For the specific example analyzed, 5 basis functions are found to be enough for a very accurate result. Even using a single basis function usually gives results that are quite accurate, for the geometries studied here.

Another validation method for the via analysis was also presented, by analyzing cavities with a via array inside. The circular cavities have PEC top and bottom surfaces and either a PEC or PMC outer wall. In the analytical modeling the via array is represented as a surface impedance inside the cavity, found from the via analysis. A simple iterative procedure is then used to determine the resonance frequency of the cavity. The cavity is then analyzed using the electromagnetic finite element solver Ansoft HFSS to get the resonance frequency. Very good agreement is obtained between the analytical and the HFSS cavity results, validating the via-array analysis.

After the validation phase, the equivalent sheet reactance of the via array is studied in more detail. By increasing the number of vias in the array the corresponding sheet reactance of the array decreases, approaching an ideal short-circuit. The values of the sheet reactance are compared with those obtain by a simple CAD formula that is based on a single via, and which neglects mutual coupling between vias in the array. It is observed that mutual coupling between vias is significant, even when the number of vias in the array is fairly small, since results from the CAD formula are seen to disagree substantially from those obtained from the accurate via analysis.

6.3 Applications of Via Arrays

The via-array analysis is applied to practical antenna designs. These include: (1) a shorted-annular-ring reduced-surface-wave (SAR-RSW) antenna, which is designed for GPS, (2) a dual-band UHF antenna, and (3) a miniaturized circular microstrip antenna.

A new design technique is presented for the SAR-RSW antenna where a reactive wall is used instead of a short-circuit wall. A cavity model of the antenna is used to find the required value of the reactive wall once its location is specified and from this the required value of the sheet reactance is obtained. The sheet reactance is then realized using a circular array of vias, with the number of vias and the radius of the vias chosen to give the required sheet reactance. Several practical designs are presented together with their HFSS simulations.

Next, the application of the via-array analysis to the design of a dual-band UHF antenna is discussed. It is shown that the via analysis can easily replace the tedious trial-and-error method that was used previously to determine the required via radius and number of vias in order to realize the desired antenna response. After solving the PMC cavity model for the antenna, where the array of vias is represented as a surface impedance wall, the number and the radius of the vias are easily determined using the via-array analysis. A comparison shows that results from a previous method, which uses a cavity analysis together with HFSS, agrees very well with results obtained from the new via analysis.

The last example that is presented using a via array is a miniaturized circular microstrip antenna that has a circular via array inside of it. The microstrip antenna is designed by using a PMC cavity model of the via-loaded circular microstrip antenna. The surface impedance obtained from the via analysis is used to realize the array of vias by determining the required number of vias and the via radius. A comparison of results from an HFSS simulation of the antenna and results from the cavity model show a very good agreement, clearly demonstrating the applicability and accuracy of the via-array analysis.

References

[1] C. A. Balanis, *Antenna Theory*, John Wiley and Sons, Inc., Hoboken, New Jersey, 2005.

[2] R. B. Waterhouse, *Microstrip Patch Antennas*, Kluwer Academic Publishers, Inc., Norwell, Massachusetts, 2003.

[3] D. M. Pozar, “Microstrip antennas,” *Proc. IEEE,* vol. 80, no. 1, pp. 79-91, January 1992.

[4] D. R. Jackson, J.T. Williams, A. K. Bhattacharyya, R.L. Smith, S. J. Buchheit and S.A. Long, “Microstrip Patch Designs That Do Not Excite Surface Waves,” *IEEE Trans. Antennas and Propagation*, vol. AP-39, pp. 1026-1037, August 1993.

[5] L. I. Basilio, *New GPS Microstrip Patch Antennas Designed for Reduced Multipath Susceptibility*, Ph.D. Dissertation, Department of Electrical and Computer Engineering, University of Houston, Texas, 2003.

[6] L. I. Basilio, J. T. Williams and D. R. Jackson, “A Reduced Surface Wave GPS Antenna with Low Susceptibility to Multipath Interference,” *2002 IEEE International Symposium on Antennas & Propagation and USNC/URSI Meeting*, San Antonio, Texas. June 2002, URSI Digest, pp. 326.

[7] L. Chen, “*Design and Analysis of Reduced Surface Wave Antennas and Arrays*,” Ph.D. Dissertation, Department of Electrical and Computer Engineering, University of Houston, Texas, 2003.

[8] M. A. Khayat, J. T. Williams, D. R. Jackson and S. A. Long "Mutual Coupling Between Reduced-Surface Wave Microstrip Antennas," *IEEE Trans. Antennas and Propagation*, vol. AP-48, pp. 1581-1593, October 2000.

[9] H. Xu, "*Analysis and Design of Broadband Reduced Surface Wave Antennas and Miniaturized Microstrip Antennas with Via Loading*," Ph.D. Dissertation, Department of Electrical and Computer Engineering, University of Houston, Texas, 2006.

[10] W. F. Richards and Y. T. Lo, "Theoretical and Experimental Investigation of a Microstrip Radiator with Multiple Lumped Linear Loads," *Electromagnetics*, vol. 3, no. 3-4, pp. 371-385, July-Dec., 1983.

[11] R. Waterhouse, "Small Microstrip Patch Antenna," *Electronics Letters*, vol. 31, pp. 604-605, 1995.

[12] R. Porath, "Theory of Miniaturized Shorting-Post Microstrip Antennas," *IEEE Trans. Antennas and Propagation*, vol. 48, pp. 41-47, Jan. 2000.

[13] C. A. Balanis, *Advanced Engineering Electromagnetics*, John Wiley and Sons, Inc., New York, 1989.

[14] M. Abramowitz, I. A. Stegun, *Handbook of Mathematical Functions with Formulas, Graphs and Mathematical Tables*, U.S. Government Printing Office, Washington, D.C., 1964

[15] D. M. Pozar, "Improved Computational Efficiency for the Moment Method Solution of Printed Dipoles and Patches," *Electromagnetics*, vol.3, pp. 299-309, 1983.

[16] A. K. Bhattacharyya, *Phased Array Antennas: Floquet Analysis, Synthesis, BFNs and Active Array Systems*, John Wiley and Sons Inc., Hoboken, New Jersey, 2006.

[17] L. C. Shen, S. A. Long, M. R. Allerding, M. D. Walton, "*Resonant Frequency of a Circular Disc, Printed Printed-Circuit Antenna*," *IEEE Transactions on Antennas and Propagation*, July 1977, vol.AP-25, No.4, p. 596.

[18] A. L. Ng, "*Design of a Multi-band Low Profile Antenna System for Public Safety Vehicles*," M.Sc. Thesis, Department of Electrical and Computer Engineering, University of Houston, Texas, 2003.

[19] V. B. Davis, "*Design and Characterization of Shorted-Annular-Ring Reduced-Surface-Wave Microstrip Antennas*," Ph.D. Dissertation, Department of Electrical and Computer Engineering, University of Houston, Texas, 2000.